



TECHNISCHE
UNIVERSITÄT
WIEN

Vienna University of Technology

DIPLOMARBEIT

Characterization of the Zirconium and Chromium dispersoid in 7xxx aluminium alloys during the homogenization process

ausgeführt unter der Leitung von

Univ. Prof. Dipl.-Ing. Dr.techn. Ernst Kozeschnik
Institut für Werkstoffwissenschaft und Werkstofftechnologie

und

Uni. Ass. Dipl.-Ing. Dr.techn. Ahmad Falahati
Institut für Werkstoffwissenschaft und Werkstofftechnologie

Eingereicht an der Technischen Universität Wien
Fakultät für Maschinenwesen und Betriebswirtschaften

von

Maximilian Pöttinger

Matrikel Nr.: 0925727
Adamsgasse 9 / Top 2
A - 1030 Wien

Wien, August 2015

Abstract

This work attempts to characterize the evolution of the secondary phases, especially dispersoids, during the homogenization process of aluminium 7xxx alloys. The results will improve the parameter optimization of the simulation and at the same time validate and verify the homogenization simulation process. Four different aluminium alloys were investigated during homogenization. 7020, 7475, 7050 and TITANAL are all alloys of the 7xxx aluminium alloy series, the last one of which is a private brand of AMAG (*AUSTRIA METALL AG*). Samples were taken after casting, during the homogenization process and at the end of homogenization. For two alloys, 7475 and 7050, additional samples were taken after homogenization at elevated temperatures.

All specimens were prepared via the dimpling method, making sure no additional chemical or thermal exposure is given. With the use of a FEI Tecnai F20, images of particles within the grains and on grain borders were taken in TEM and STEM mode. Chemical compositions were identified via EDAX analysis. Furthermore number densities and dispersoid radii were calculated to analyse their evolution during homogenization.

The only encountered dispersoid in the 7020 alloy was the Al_3Zr phase. None of the Mn or Cr containing dispersoids mentioned in literature were found. The Al_3Zr phase was distributed very inhomogeneously within the grains, meaning that in many areas no dispersoids at all were found, while other regions contained plenty of them. This made it impossible to calculate a trustworthy number density. With a maximum mean radius of 16 nm the 7020 alloy has the largest mean dispersoids radius out of all four alloys. Due to a fast heating rate, high temperature level and a short holding time, the dispersoids nucleated very heterogeneously. The high homogenization temperature seems to stimulate the nucleation of large dispersoids on Fe-containing particles. During the cooling to RT the alloy starts to form new and smaller dispersoids.

7475 is the only alloy with a Cr-containing dispersoid ($\text{Al}_{18}\text{Mg}_3\text{Cr}_2$). The morphology of the $\text{Al}_{18}\text{Mg}_3\text{Cr}_2$ dispersoids can be characterized in rod-like, triangular and irregular. They appear very homogeneously within the matrix. During the cooling process an increase in number density can be observed, most probably caused by the passing through lower temperature levels (below 400°C), which led to the nucleation of new dispersoids. After homogenization the samples were heated again and the number density continued to grow. This increase is caused by the same effect, which was already observed during cooling. Due to the shape irregularities it was not possible to analyse the size evolution.

The dispersoids of the 7050 alloy (Al_3Zr) show a steady decrease in number density. The reduction can clearly be linked to the holding time and the temperature level. While the number density decreases the mean radius increases up to around 12 nm at the end of homogenization and reaches a maximum of 14 nm at the last specimen. At the end of the homogenization process the sample was reheated again. This causes an increase in number density, while the mean radius decreased, indicating the precipitation of new dispersoids.

The TITANAL alloy is the alloy with the highest Zr concentration, number density and volume fraction percentage. A sharp rise in the number density was observed in the early stages of the homogenization process, followed by a constant decrease until the end. Plenty of small dispersoids were encountered with a mean radius of around 4 nm at

the first measured specimen and a maximum mean radius of 8 nm at the end of homogenization. This is attributed to the very low heating rate (the lowest out of all alloys under investigation) and low maximum homogenization temperature. It appears that the homogenization temperature for the TITANAL alloy strongly favours the nucleation for Al_3Zr dispersoids. This finding is confirmed by the nucleation of new dispersoids in the 7050 alloy at similar temperatures in the specimen after homogenization.

The comparison between the simulation and experimental results showed a good correlation. Although simulation and databases still need further improvements the general trends could be verified. Only the simulation results of the 7475 alloy had larger discrepancies with the experimental findings.

Kurzfassung

Diese Arbeit beschäftigt sich mit der Charakterisierung von Ausscheidungsprodukten, im Besonderen mit den Dispersoiden, während der Homogenisierung einer 7xxx Legierung. Vier unterschiedliche Aluminiumlegierungen mit speziellen Homogenisierungsbehandlungen wurden untersucht. 7020, 7474, 7050 und TITANAL sind alle Legierungen aus der 7xxx Serie, wobei TITANAL eine hauseigene Marke der Firma AMAG (AUSTRIA METALL AG) ist. Es wurden Proben nach dem Gießen, während der Homogenisierung und am Ende der Homogenisierungsbehandlung genommen. Für die 7475 und 7050 Legierungen wurden weiteres auch Proben nach der Homogenisierung bei erhöhter Temperatur entnommen.

Alle Probenstücke wurden mittels der Dimpling-Methode vorbereitet um eine zusätzliche chemische und thermische Beeinflussung zu vermeiden. Mittels eines FEI Tecnai F20 im TEM- oder STEM-Mode wurden Bilder von Partikeln im Korn als auch auf Korngrenzen aufgenommen. Die chemische Zusammensetzung wurde über eine EDX Analyse festgestellt. Des Weiteren wurde die Dispersoidendichte, der mittlere Dispersoidenradius und deren Entwicklung in der Homogenisierungsphase berechnet.

Der Al_3Zr Dispersoid war der einzige Dispersoid in der 7020 Legierung. Es wurden keine Mn- oder Cr-haltigen Dispersoide entdeckt, obwohl in der Literatur darauf verwiesen wird. Die Al_3Zr Phase war ausgesprochen inhomogen verteilt. Oft wurden Gegenden gefunden in denen kein einziger Dispersoid angetroffen wurde, während in anderen Regionen die Matrix voll davon war. Daher war es nicht möglich eine aussagekräftige Dispersoidendichte zu berechnen. Die 7020 Legierung hat einen maximalen mittleren Radius von 16 nm, der größte gemessene Wert aller Legierungen. Bedingt durch die schneller Aufheizrate, die hohe Temperatur und die kurze Haltezeit bilden sich die Dispersoide sehr heterogen. Die hohe Homogenisierungstemperatur scheint eine Bildung auf eisenhaltigen Teilchen zu fördern. Während des Abkühlungsprozesses, gegen Ende der Homogenisierung, bilden sich neue, kleine Dispersoide.

7475 ist die einzige untersuchte Legierung mit einem Cr-haltigen Dispersoid ($\text{Al}_{18}\text{Mg}_3\text{Cr}_2$). Die $\text{Al}_{18}\text{Mg}_3\text{Cr}_2$ Partikeln wurden in stab-, dreieck-, und unregelmäßige Formen vorgefunden. Sie treten sehr homogen in der Matrix auf. Während der Abkühlungsphase nimmt die Dispersoidendichte zu, wahrscheinlich begründet durch die Bildung von neuen Dispersoiden bei niedrigeren Temperaturen ($<400^\circ\text{C}$). Nach dem Homogenisierungsprozess wurde die Legierung erneut erwärmt und die Dispersoidendichte steigt weiter an. Auf Grund der unregelmäßigen Form der Dispersoide konnte keine Größenanalyse durchgeführt werden.

In der 7050 Legierung reduziert sich die Al_3Zr Dichte konstant. Die Reduktion kann eindeutig auf die Haltezeit und die Temperatur zurückgeführt werden. Während die Dichte abnimmt, wachsen die Dispersoide auf eine Größe von 12 nm an. In der letzten Probe nach der Homogenisierungsbehandlung erreichen sie einen Radius von 14 nm. Die Zunahme der Dispersoidendichte bei der Wiedererwärmung nach der Homogenisierung, bei einer gleichzeitigen Abnahme des mittleren Dispersoidenradius, lässt auf die Bildung von neuen Dispersoiden schließen.

Die TITANAL Legierung ist jene mit der höchsten Zr Konzentration, Dispersoidendichte und Volumenanteilsprozent. Die Dichte wächst zu Beginn der Homogenisierung an und fällt dann bis zum Ende des Homogenisierungsprozesses kontinuierlich ab. Eine große Anzahl an sehr kleinen Dispersoiden mit einem mittleren Radius von 4 nm in der ersten gemessenen Probe und 8 nm in der letzten Probe wurden beobachtet. Die kleine

Dispersoidengröße wurde der sehr geringen Aufheizrate (die geringste in allen untersuchten Legierungen) und der geringen maximalen Homogenisierungstemperatur zugeschrieben. Die Homogenisierungstemperatur von TITANAL scheint die Bildung einer Vielzahl von Dispersoiden zu begünstigen. Diese Vermutung wird durch die Bildung von neuen Dispersoiden in den Proben nach der Homogenisierung der 7050 Legierung untermauert, welche ein ähnliches Temperaturniveau besitzen. Simulation und experimentelle Ergebnisse scheinen zu korrelieren. Obwohl die Simulation und die Datenbanken noch Verbesserungen benötigen decken sich die Trends und beide Untersuchungen zeigen ähnliche Resultate. Einzig die Simulation der 7475 Legierung stimmt nicht mit den experimentellen Ergebnissen überein.

Acknowledgements

First of all I want to thank Ernst Kozeschnik for fascinating me for the field of material science. Thanks to his introduction to Ahmad Falahati, who offered me this great opportunity, I was able to write my thesis about this interesting topic. I learned a great deal within the last few months and his valuable insight helped me to finish this thesis. My most sincere thanks to Siamak Rafiezadeh who supported me along the whole process and with whom I spend a great deal of time discussing different topics regarding our research. Tomasz Wojcik owes a special mention as he spent hours with me at the TEM analysing the samples. The financial support of the MCL (Materials Center Leoben) is gratefully acknowledged.

Many thanks goes to my family, especially my parents, who provided me with the financial and emotional support throughout my studies.

Table of Content

Abstract	II
Kurzfassung.....	IV
Acknowledgements	VI
List of Figures	X
List of Tables	XII
List of Equations	XIII
Nomenclature	XIV
1. Introduction	16
2. Objective	18
3. State of the Art	19
3.1. Physical properties	19
3.2. Production process.....	20
3.2.1. Bayer-process.....	22
3.2.2. Electrolysis.....	22
3.2.3. Production process and thermal treatments	24
3.2.4. Direct Chill casting	24
3.2.5. Classification of Aluminium Alloys	27
3.2.6. Homogenization	29
3.2.7. Precipitation strengthening	30
3.2.8. Dispersoids	30
3.2.9. Phases.....	33
4. Experimental	34
4.1. Materials and Homogenization	34
4.1.1. Materials / Samples	34
4.1.2. Homogenization	36
4.2. Sample Preparation.....	38
4.3. Transmission Electron Microscopy, Energy Dispersive X-Ray Spectroscopy and Electron Energy-Loss Spectrum	39
4.3.1. TEM	39
4.3.2. STEM	40
4.3.3. EDX	40
4.3.1. EELS.....	40
5. Simulation	42
6. Results	43

6.1.	7020	43
6.1.1.	As-cast structure	43
6.1.2.	Dispersoids	43
6.1.3.	Other Phases	46
6.2.	7475	47
6.2.1.	As-cast structure	47
6.2.2.	Dispersoids	48
6.2.3.	Non-dispersoid phases	50
6.3.	7050	52
6.3.1.	As-cast structure	52
6.3.2.	Dispersoids	52
6.3.3.	Non-dispersoid phases	55
6.4.	TITANAL.....	58
6.4.1.	As-cast structure	58
6.4.2.	Dispersoids	59
6.4.3.	Non-dispersoid phases	61
6.5.	Annotations:	64
6.6.	Spectra	65
7.	Discussion.....	69
7.1.	7020	69
7.1.1.	Non-dispersoid phases	69
7.1.2.	Dispersoids, number density and size evolution.....	69
7.2.	7475	70
7.2.1.	Non-dispersoid phases	70
7.2.2.	Dispersoids, number density and size evolution.....	71
7.3.	7050	71
7.3.1.	Non-dispersoid phases	71
7.3.2.	Dispersoids, number density and size evolution.....	72
7.4.	Titanal.....	74
7.4.1.	Non-dispersoid phases	74
7.4.2.	Dispersoids, number density and size evolution.....	74
8.	Simulation vs laboratory investigation.....	76
8.1.	7020	76
8.2.	7475	77
8.3.	7050	77
8.4.	TITANAL.....	78
9.	Summary and Conclusion.....	80
	References	81

A. Appendix..... 86

List of Figures

Figure 1-3.1-1 Worldwide aluminium production (reprinted from http://www.world-aluminium.org/statistics/#data)	16
Figure 3.2-3.2-1 Production steps for primary aluminium.....	21
Figure 3.2-2 Modern electrolysis cell with preburnt anodes (reprinted from [5]).....	23
Figure 3.2-3 Production process and thermal treatment (reprinted from [10]).....	24
Figure 3.2-4 DC cast process; main parameters are underlined (reprinted from [13])....	25
Figure 3.2-5 as-cast structure 7020 [24]	29
Figure 3.2-6 Homogenization for 2h at 550°C [24]	29
Figure 3.2-7 Cutting through small particles [37]	31
Figure 3.2-8 Orowan mechanism [33]	31
Figure 4.1-1 7020: Homogenization process including withdrawal of samples	36
Figure 4.1-2 7475 Homogenization process including withdrawal of samples	37
Figure 4.1-3 7050 Homogenization process including withdrawal of samples	37
Figure 4.1-4 Titanal Homogenization process including withdrawal of samples.....	38
Figure 4.1-5 Homogenization processes in comparison.....	38
Figure 6.1-1 As-cast structure [7020]	43
Figure 6.1-2 Dispersoid images [7020]	44
Figure 6.1-3 Dispersoid radius [7020].....	45
Figure 6.1-4 Mean dispersoid radius [7020].....	45
Figure 6.1-5 Mean radius depicting the smallest and largest dispersoid radius [7020] ..	45
Figure 6.1-6 TEM/STEM images of other phases [7020].....	46
Figure 6.1-7 Chemical composition of obtained phases [7020]	47
Figure 6.2-1 As-cast structure [7475]	48
Figure 6.2-2 Dispersoid images [7475]	49
Figure 6.2-3 Number Density [dispersoid per m ³]	49
Figure 6.2-4 TEM/STEM images of other phases [7475].....	50
Figure 6.2-5 Chemical composition of the encountered phases [7475].....	51
Figure 6.3-1 As-cast structure [7050]	52
Figure 6.3-2 Dispersoid images	53
Figure 6.3-3 Number Density (dispersoids per m ³) [7050]	54
Figure 6.3-4 Dispersoid radius [7050].....	54
Figure 6.3-5 mean dispersoid radius [7050]	54
Figure 6.3-6 Mean radius depicting the smallest and largest dispersoid radius [7050] ..	55
Figure 6.3-7 TEM/STEM images of other phases [7050].....	56
Figure 6.3-8 Chemical composition of the encountered phases [7050].....	58
Figure 6.4-1 As-cast structure [TITANAL]	58
Figure 6.4-2 Dispersoid images [TITANAL].....	59
Figure 6.4-3 Number density (dispersoids per m ³) [TITANAL]	60
Figure 6.4-4 Dispersoid radius [TITANAL].....	60
Figure 6.4-5 Mean dispersoid radius [TITANAL]	61
Figure 6.4-6 Mean radius depicting the smallest and largest dispersoid radius [TITANAL]	61
Figure 6.4-7 TEM/STEM images of other phases.....	62
Figure 6.4-8 Chemical composition of obtained phases [TITANAL].....	63
Figure 6.5-6.6-1 Zr-containing dispersoid [7020], [7050], [TITANAL].....	65
Figure 6.5-6.6-2 Cr-containing dispersoid [7475].....	65

Figure 6.5-6.6-3 Mg-Si [7020], [7474], [7050], [TITANAL]	66
Figure 6.5-6.6-4 Mg-Cu [7475], [7050], [TITANAL]	66
Figure 6.5-6.6-5 Fe-Cu [7475], [7050]	66
Figure 6.5-6.6-6 Fe-Mn-Si [7020], [7475], [7050], [TITANAL]	67
Figure 6.5-6.6-7 Fe-Mn-Si-Cr [7020], [7475]	67
Figure 6.5-6.6-8 Ti [7020], [7475]	67
Figure 6.5-6.6-9 Mg-Cu-Zn [7020], [7050], [TITANAL]	68
Figure 6.5-6.6-10 Mg-Cu-Zn 2 [7475], [7050]	68
Figure 6.5-6.6-11 Ti-Cr [7020], [7050], [TITANAL]	68
Figure 8.1-1 Mean radius Simulation/Experimental [7020]	76
Figure 8.2-1 Mean ND Simulation/Experiment [7050]	77
Figure 8.3-1 Mean ND Simulation/Experiment [7050]	78
Figure 8.3-2 Mean radius Simulation/Experimental [7050]	78
Figure 8.4-1 Mean ND Simulation/Experiment [TITANAL]	79
Figure 8.4-2 Mean radius Simulation/Experimental [TITANAL]	79

List of Tables

Table 3.1-1 Physical properties of pure aluminium at 20°	19
Table 3.1-2 Mechanical properties of pure aluminium (Al 99,98) [7]	20
Table 3.2-1 World Bauxite mine production (in 1000 t) [8]	21
Table 3.2.5-1 Classification of wrought alloys [4]	28
Table 3.2.5-2 Classification of cast alloys [4]	28
Table 3.2.9-1 Expected phases according to literature in the 7020, 7475, 7050 and TITANAL alloy	33
Table 4.1.1-1 Chemical composition of alloys: 7020, 7475, 7050 and TITANAL	35
Table 6.1.3-1 Encountered Phases [7020]	47
Table 6.2.3-1 Encountered phases [7475]	51
Table 6.3.3-1 Encountered phases [7050]	56
Table 6.4.3-1 Encountered phases [TITANAL]	62
Table 7.3.2-1 Number density reduction per hour [7050]	73
Table 7.3.2-2 Volume fraction [7050]	74
Table 7.4.2-1 Coarsening rate	75
Table 7.4.2-2 Volume fraction [TITANAL]	75

List of Equations

- (1) Critical Orowan shear stress.....25
- (2) Zener pinning equation.....25
- (3) Hall-Petch relationship.....25
- (4) De Broglie equation33
- (5) Raylight criterion.....33

Nomenclature

AA	Aluminium Association
AMAG	AUSTRIA METALL AG
ANSI	American National Standards Institute
C	Celsius
CEN	Comité Européen de Normalisation 'European Committee for Standardization'
DAS	Dendrite Arm Spacing
DC	Direct Chill
DIN	Deutsche Industrie-Norm 'German Industrial Standard'
EDX	Energy Dispersive X-ray Spectroscopy (also referred to as EDAX)
EELS	Electron Energy Loss Spectroscopy
EMC	Electromagnetic Casting
EN	Euroäische Norm 'European Standard'
E-phase	$Al_{18}Mg_3Cr_2$
GB	Grain Boundary
J	Joule
K	Kelvin
Kg	Kilogramm
LMP	Low Melting Point Phase
ND	Number Density
Pa	Pascal
PIPS	Precision Ion Polishing System
Px	Probe Number x
RT	Room Temperature
STEM	Scanning Transmission Electron Microscope
S-phase	Al_2CuMg
t	Tons
TEM	Transmission Electron Microscop
T-phase	$Mg_3(Al,Cu,Zn)_2$
USA	United States of America
V	Volt

V_{cast}	Casting Speed
W	Watt
Wh	Watt-hour
WQ	Water Quenched
WW	World War
Ω	Ohm

1. Introduction

In 1825 the chemist Hans Christian Oersted was the first to isolate (impure) aluminium. Friedrich Woehler continued to improve this method and managed to produce pure aluminium. Around 1854 Brunsen and Saint-Claire Deville (independently) discovered a way to produce aluminium via electrolysis from Na-AlCl₃. But the technology at the time was not advanced enough to exploit this method. The development of the dynamo by Siemens in 1866 enabled the industry to produce electrical energy with high currents and opened up the door for industrial aluminium production. The French and American chemists Héroult and Hall independently registered patents in 1886 for an aluminium electrolysis of aluminium-oxide (Al₂O₃) in dissolved cryolite between two coal electrodes. Production started 1888/89 in Pittsburgh(USA) and Neuhausen (Switzerland). This marked a breakthrough in the industrial aluminium production. The production costs dropped rapidly and made aluminium an affordable metal [1]. Before the significant drop in production prices, aluminium was still thought to be a curiosity as only 2t of it were produced worldwide [2]. During WW I and WW II the aluminium demand experienced an enormous boost. Aluminium became an alternative to steel in many fields. If we look at the current situation we see that the aluminium production is still increasing significantly, it doubled within the last 15 years. Figure 1-1 clearly depicts Chinas leading role in the aluminium production. Chinas estimated unreported aluminium production is 3,600 thousand metric tons. This is more than the whole production of Western Europe (3,514).

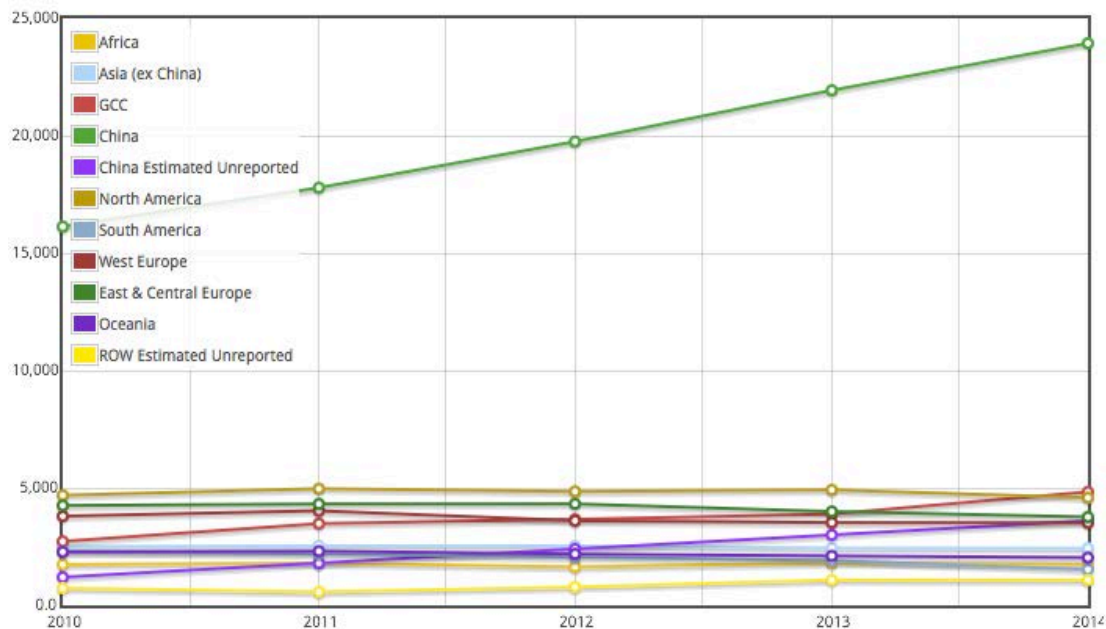


Figure 1-3.1-1 Worldwide aluminium production (reprinted from <http://www.world-aluminium.org/statistics/#data>)

With rising demand, the market also demanded better mechanical properties. This led to the invention of DURALUMIN by Alfred Wilm. He discovered the strengthening effect of “natural aging” for wrought aluminium alloys, marking

the starting point for a continuous improvement of the mechanical properties over the years.

Today we find many different alloys with added constituents like Mg, Mn, Si, Cu or Zn. Together with specific heat treatments the current aluminium alloys are designed and treated to fit the individual purposes.

The increasing use of computational methods led to new ways of developing new alloys or heat treatments. By using simulation software time consuming and costly experiments can be reduced to a minimum. This development leads the way for future research, making reliable simulation software of the utmost importance for producers and researchers.

2. Objective

High strength aluminium alloys are used in many industries and every year new fields of applications are added. This makes the 7xxx aluminium alloys a particularly interesting topic of research. Although plenty of research has been conducted on various aspects of these alloys, literature about the dispersoids and their development is scarce. Furthermore very few works about the development of small particles with small volume fractions and their chemical composition along the homogenization procedure can be found.

In this thesis the analysis of 4 different 7xxx aluminium alloys, 7020, 7475, 7050 and TITANAL was conducted. In all of these alloys the focus was placed on particles within the grain. Although all secondary phases were analysed, the development of the dispersoids was the main topic. The aim is to gain knowledge about the homogenization process and the different effects that influence the formation and development of dispersoids.

All information about the as-cast samples was implemented into the thermodynamic database of *MatCalc – THE MATERIALS CALCULATOR*¹. The comparison of the results was then used to improve the calculations and verify the credibility of the simulation.

¹ <http://matcalc.tuwien.ac.at/>

3. State of the Art

In this chapter we look at aluminium as a whole. A general overview, from the raw material to the finished good, enables the reader to understand the surrounding aspects.

We start with the physical properties, examine the production process and end up at the different possibilities to enhance the properties of aluminium

3.1. Physical properties

Al is the symbol for aluminium in the periodic table and its atomic number is 13. It only exists in chemical compounds and is the 3rd most common element in the earth's crust.

Table 3.1-1 Physical properties of pure aluminium at 20°

Property	Index	Unit
Atomic number	13	-
Atomic weight (rel. atomic mass)	26,9815385	g/mol
Lattice structure	Face centered cubic	
Lattice constant	0,40496	nm
Atomic radius	0,1431	nm
Density	2,6989*10 ³	Kg/m ³
Young's modulus	66,6	kN/mm ²
Shear modulus	25,0	kN/mm ²
Poisson's ratio, ν	0,35	-
Mean linear thermal expansion coefficient (20°C - 100°C)	23,6*10 ⁻⁶	1/°C
Thermal conductivity	235	W/m*K
Melting temperature	660,2	°C
Volume decrease liquid/solid	7,1	%
Linear contraction between 660°C and 20°C	1,85	%
Melting heat	390	kJ/kg
Boiling temperature	2470	°C
Vaporization heat	11,4	MJ/kg
Combustion heat	31	MJ/kg
Specific heat at constant pressure, c_p	0,89	kJ/kg*K
Activation energy at self-diffusion	120	kJ/mol
Electric conductivity	37,67	m/Ω*mm ²
Specific electric resistivity	26,55	nΩ m

The density of aluminium (2,69 kg/dm³) is very low. Only a few materials like Magnesium have lower densities (1,74 kg/dm³). Materials like iron (7,78 kg/dm³) and steel C15 (7,85 kg/dm³) are 3 times as heavy as aluminium, making it a lighter alternative [3].

Aluminium is almost not paramagnetic so it can be used to screen sensitive electronic equipment. It is also impenetrable, meaning it cannot be penetrated by light or aroma, even when processed to a thickness of only 0,006 mm. Ideal properties for the food and pharmaceutical industry (e.g. as foil, blister-packaging for medications) [4]. The thermal conductivity is very high, making it a great material for heat exchanging devices. It has also a very high electric conductivity. Related to its weight aluminium has roughly twice the electric conductivity of copper. Hence high voltage power lines are usually made out of aluminium. The electric conductivity varies with the components of the alloy and the heat treatment. For this reason an electric conductivity test can be done to check the heat treatment procedure.

It also has a high chemical affinity to oxygen, which leads to an oxide layer on the metal surface. This layer protects the aluminium from further oxidation but also changes the properties of the metal [5].

In Table 3.1-2 we see that pure aluminium is very soft in comparison with a standard metal. Construction steel S235JR for instance has a tensile strength of 360-510 MPa [6]. Only in combination with alloying elements can aluminium increase its tensile properties.

Table 3.1-2 Mechanical properties of pure aluminium (Al 99,98) [7]

Yield strength (R _{p0,2})	9,81...24,5 MPa (soft)
	68,7...98,1 MPa (hard)
Tensile strength (R _m)	39...49MPa (soft)
	88...117,7 MPa (hard)
Elongation at fracture (A ₁₀)	30...45% (soft)
	1...3% (hard)
Contraction at fracture	97...99% (soft)
	85...90% (hard)
Brinell hardness	15 (soft)
	25 (hard)

3.2. Production process

For industrial production purposes only the raw material “Bauxit” has enough aluminium (>50 % of aluminium-oxide) to be suitable for production of aluminium oxide. Although efforts were made to extract aluminium oxide from other raw materials, none of them are technically put into practice.

Bauxite is an aluminium rich weathered material. The name Bauxite comes from the French city “Les Baux” where the material was first found in the 19th century [7]. High Bauxite fields can be found in regions with high temperature and a

great amount of rainfall. Hence the greatest Bauxite reserves are found along tropical regions.

In Table 3.2-1 we find the world's Bauxite mine production and the reserves.

Table 3.2-1 World Bauxite mine production (in 1000 t) [8]

Country	Mine production 2013	Reserves
Australia	81,100	6,500,000
Indonesia	55,700	1,000,000
China	46,000	830,000
Brazil	32,500	2,600,000
Guinea	18,800	7,400,000
India	15,400	540,000
Jamaica	9,440	2,000,000
Kazakhstan	5,400	160,000
Russia	5,320	200,000
Suriname	2,700	580,000
Venezuela	2,160	320,000
Greece	2,100	600,000
Guyana	1,710	850,000
Vietnam	250	2,100,000
Other countries	4,570	2,400,000

Nearly all important Bauxite repositories are found along the equator. The chemical and mineralogical composition differs very much. Each region has its own special composition. The typical composition contains Al_2O_3 in amounts greater than 50% [7].

To produce primary aluminium two process steps are necessary.



Figure 3.2-3.2-1 Production steps for primary aluminium

3.2.1. Bayer-process

From 1885-1892 Austrian scientist Karl Joseph Bayer worked in Russia and it was there where he made two important discoveries on which he based his patents [9].

The Bayer-process itself is a two-step-process:

Production of aluminium-hydroxide

Bauxite is being finely ground in autoclaves at 100-360°C. Sodium hydroxide solution is added. Aluminium-hydroxide solutes at higher temperatures in sodium-hydroxide and forms sodium aluminates. All other constituents do not solute, they form the red mud. The color red is due to the high iron concentration. Aforementioned red mud is being isolated.

The oversaturated aluminate liquor segregates pure aluminium-oxide at lower temperatures. This procedure is enhanced by adding solid aluminium-hydroxide (seed-crystal).

Vacuum filters separate the aluminium-hydroxide.

Production of aluminium-oxide

The second step dehydrates the aluminium-hydroxide to aluminium-oxide.

This process happens at temperatures around 1000-1300°C in fluidized beds. The result is a white powder – aluminium-oxide [7].

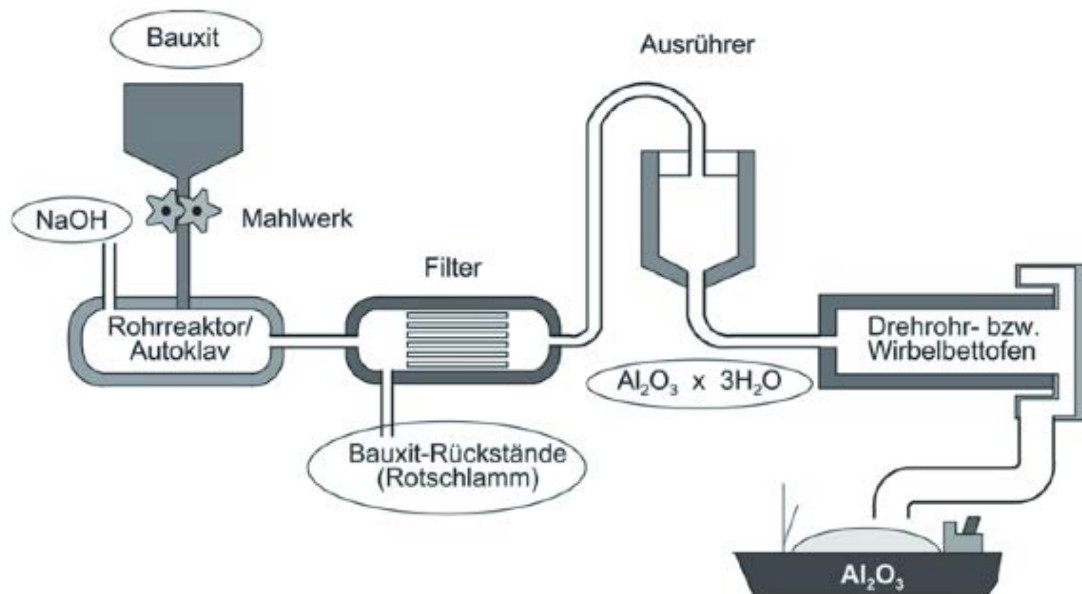


Figure 3.2-2 Production of aluminium-oxide via the Bayer-process (reprinted from[5])

3.2.2. Electrolysis

Aluminium is less noble than hydrogen, hence a electrolysis in a diluted solution is not possible. The best alternative offers the fused-salt electrolysis. One important condition for an efficient process is a low melting point. Aluminium-

oxide has a melting point of 2050°C, ergo not quite optimal for this procedure. But by adding suitable salts the melting point can be lowered significantly. If you dissolve aluminium-oxide in cryolite (Na₃AlF₆) the eutectic melting point lowers to 962,5°C (with 10,5% Al₂O₃).

In Figure 3.2.2-1 you can see a simplified version of the process with preburnt anodes and a central feeding.

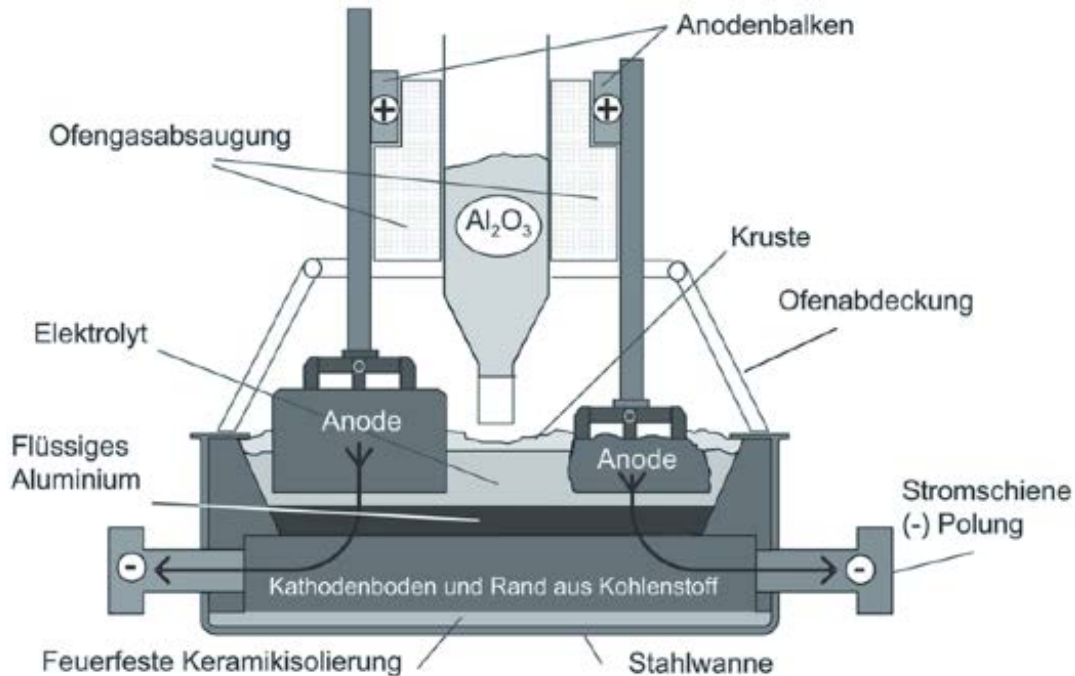
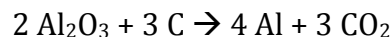


Figure 3.2-2 Modern electrolysis cell with preburnt anodes (reprinted from[5])

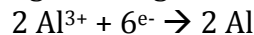
The electrolysis takes place in a steel tub. The walls and the base are made out of carbon and the base also acts as a carbon-cathode. Above the cathode you will find liquid aluminium, molten electrolyte and the carbon-anode in this order. During the electrolysis liquid aluminium will sink to the bottom of the tub (the carbon-anode).

The decomposition follows:



There are two main reactions:

At the cathode aluminium is being discharged:



At the anode all oxygen ions react with the carbon to CO₂, hence the anode dissipates.

This process requires currents from I= 100...320kA at a voltage around 4,2 V [7].

Per kg aluminium 12,5-15 kWh are necessary, this amounts to about 30-40% of the production costs for primary aluminium [5].

Secondary aluminium plays a very important economical and ecological role.

Aluminium is 100% recyclable and a great amount of the aluminium demand is satisfied through secondary aluminium. The aluminium scrap business is quite profitable, especially for countries with limited raw materials and energy resources like Germany. This led to a scrap aluminium guideline (EN 13920-1-16:2003), which differs between 22 different aluminium scrap classes.

Secondary aluminium consumes 95% less energy than primary aluminium. Most of the secondary aluminium is used as cast alloy and the quality difference between primary and secondary cast alloys is virtually none, making it a very profitable alternative [5].

3.2.3. Production process and thermal treatments

After aluminium is available in its raw condition it still has to undergo plenty of more or less difficult steps to reach its final stage at which it can be sold in to the manufacturing industry.

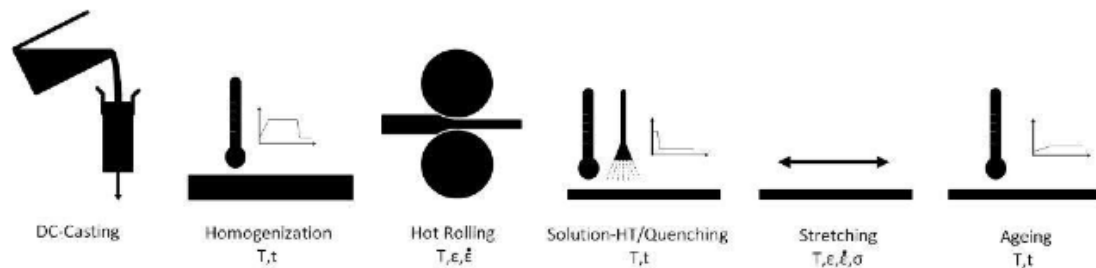


Figure 3.2-3 Production process and thermal treatment (reprinted from [10])

The process starts with DC-casting, followed by homogenization. To reach the final thickness hot rolling is commonly applied and in some cases even cold rolling. Hot and cold rolling require certain formability, this formability is strongly influenced by the homogenization. After the thermo-mechanical treatment solution heat treatment with immediate quenching afterwards is applied. By exposing the alloy to higher temperatures over a certain period of time, elements can dissolve back into the matrix. Quenching freezes the structures creating a supersaturated solid solution. This is the essential requirement for the formation of precipitates during aging. Quenching induces high thermal stresses, which cause plastic deformation. Via stretching the alloy is brought into its final shape, inducing a large amount of dislocations into the material. During the natural (RT) or artificial (elevated temperatures) ageing process finely dispersed particles precipitate within the matrix increasing the material strength [10], [11].

In the following sections of the thesis special attention is paid to the DC- and Homogenization-process. Furthermore we will take a look at the formation of dispersoids and their purpose.

3.2.4. Direct Chill casting

Direct chill casting was invented in 1936-1938 almost simultaneously in Germany and the USA. Due to an increasing demand for passenger airline transportation and later for military needs during World War II, DC casting quickly became the only production method for aluminium production on a large

scale. The main advantage of DC casting is that the solidification (and the formation of structure and defects) takes place in a relatively narrow layer of the billet and can therefore be kept under control [12].

During DC casting, liquid metal is poured into a water-cooled mould. The mould is initially closed by a starting block beneath. As soon as the liquid metal starts to solidify and a solid shell close to the mould wall is formed, the starting block is lowered into a pit with a constant casting speed of V_{cast} while keeping the metal level in the mould at a certain height. The water-cooled mould has to extract enough heat to ensure the metal can build up a solid shell (primary cooling). While this process plays an important role, most of the heat extraction happens at the secondary cooling (provides up to 95% heat extraction), where the solid shell is quenched with water jets (Figure 3.2.4-1)[13].

Although the technological principles remained nearly the same, a continuous improvement has led to [14]:

- Better surface quality
- Reduction in macrosegregation
- Finer and more uniform structure
- A shallow sump with a smaller thermal gradient

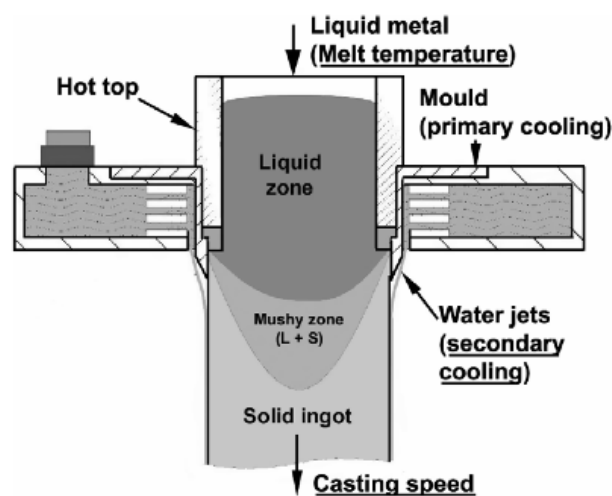


Figure 3.2-4 DC cast process; main parameters are underlined (reprinted from [13])

Out of all the different casting methods, one should be mentioned in particular: electromagnetic casting. The electromagnetic force prevents the metal from touching the mould. This leads to a very high surface quality and avoids surface imperfections, such as surface oscillation and subsurface segregation, usually caused by a mould of DCC. The presence of a stirring motion in the melt leads to a significant reduction in grain size. Furthermore porosity and segregation are reduced and internal cracks are minimized [15].

Casting Defects

Macrosegregation

According to Nadella *et al* macrosegregation can be defined as “... *spatial non-uniformity in the chemical composition on the scale of a solidified casting.*”.

Unlike microsegregation, macrosegregation, which happens at scales of 10-100 μm , macrosegregation cannot be minimised/eliminated by heat treatment.

In some extreme cases the composition of the alloying elements in certain regions may even be outside the registered limits for this alloy [13]. During casting highly segregated phases are present in the semi-solid zone and the physical displacement of these phases leads to macrosegregation.

This may occur by [16]:

- Floating or settling of precipitated phases
- Inclusions early in the solidification
- Movement of liquid within the solid-liquid zone as a result of thermal contractions
- Solidification shrinkage
- Density differences in the interdendritic liquid, in the liquid ahead of the advancing solid
- Convection currents driven by temperature-induced density differences in the fluid

Macrosegregation can be reduced but never completely eliminated, as the cooling rate is limited.

Microsegregation

The dendritic solidification of an alloy occurs over a broad range of temperatures and results in an inhomogeneous distribution of solute atoms between dendrite arms. At high cooling rates the atomic diffusion processes cannot redistribute the solutes sufficiently within the liquid in the vicinity of the solid-liquid interface and within the solid. This leads to different chemical compositions within the area of a DAS (dendrite arm spacing) or grain cells [16].

Microsegregation depends on the temperature range of the solidification as it influences the diffusivity of the solute atoms in both the liquid and solid phases.

As mentioned earlier, microsegregation can be eliminated in the homogenization or solution treatment stage. Higher temperatures well below the solidus temperature alleviate the concentration gradients [14], [16].

Hot Tearing

Due to a hindered contraction and a lack of feeding during the solidification, fractures are formed in the mushy zone. Those irreversible fractures are called hot tearing. Studies show that hot tearing occurs in the late stages of solidification when the volume fraction of solid is above 85-95%. Controlled casting, meaning that temperature and stress gradients are kept to a minimum, and a fine grain structure help to prevent hot tearing. The correlation between the alloy composition and the hot tearing susceptibility is well known and can be taken into account [17].

To predict hot tearing different criteria were developed, those criteria can be subdivided into mechanical and non-mechanical criteria. The mechanical criteria are derived based on the mechanical behaviour of a semi-solid mush. Non-mechanical criteria are based on other features in the solidification process such as the lack of feeding [18].

Pores

Pores reduce the mechanical properties of the alloy. Studies on the fatigue behaviour prove the negative influence of porosity on the aluminium alloy [19]. Dissolved hydrogen and volumetric shrinkage during the casting process are the main porosity factors [20].

As hydrogen is 10 times more soluble in liquid than in solid [21], gas pores form when sufficient supersaturation of hydrogen in the liquid occurs. The higher the initial hydrogen content the higher the number density and the size of the pores. During solidification, the pore formation is also influenced by the composition of the alloy and the solidification conditions. For instance increases the percentage porosity with the magnesium content in the alloy (0-5 wt.%) but it decreases above 9 wt.%. As liquid feeding becomes more and more difficult with an increasing solidification range a certain porosity is inevitable in the DC casting of aluminium ingots [22].

3.2.5. Classification of Aluminium Alloys

Aluminium alloys are divided into two main groups: wrought and cast aluminium alloys.

Cast aluminium alloys:

The fastest way from the molten material to a final part is casting.

Good castability depends on:

- flowability
- easy mold filling
- good heat cracking resistance

Aluminium satisfies all of these parameters making it a suitable material for casting.

In the casting process many different aspects have to be considered and controlled to ensure neat casting, leading to a difficult and complex process. In order to improve the process many alloying elements have been put to test and a few elements proved to be very suitable. Those alloys tend to have very different characteristics than wrought aluminium alloys [5].

Wrought aluminium alloys

The single most important aspect for wrought aluminium alloys is plastic deformability. Wrought alloys usually have a lower amount of alloying elements. Cast alloys tend to have an alloy content around 10-12 %, while wrought alloys tend to be below 10% [7].

Furthermore you can differentiate between alloys, which are suitable for precipitation and normalized alloys.

In an attempt to standardize the engineering standards, the Comité Européen de Normalisation (CEN) was put into place in Europe. For wrought alloys the already existing system of the North American Aluminum Association (AA) was adopted. The system for the cast alloys was developed independently but it is quite similar to the wrought alloy system.

Wrought alloys:

Table 3.2.5-1 Classification of wrought alloys [4]

Group	Alloy Type	Example	Precipitation Hardening
1XXX	Pure Al	EN AW-1050A	Not possible
2XXX	Al Cu	EN AW-2024	Yes
3XXX	Al Mn	EN AW-3003	Not possible
4XXX	Al Si	EN AW-4046	Not possible
5XXX	Al Mg	EN AW-5182	Not possible
6XXX	Al MgSi	EN AW-6082	Yes
7XXX	Al-Zn	EN AW-7020	Yes
8XXX	Other Elements	EN AW-8011A	Not possible
9XXX	Not used		

Cast alloys:

Table 3.2.5-2 Classification of cast alloys [4]

Group	Alloy Type	Example	Precipitation Hardening
21XXX	Al Cu	EN AC-21100 (Al Cu ₄ Ti)	Yes
41XXX	Al SiMgTi	EN AC-41000 (Al Si ₂ MgTi)	Yes
42XXX	Al Si ₇ Mg	EN AC 42100 (Al Si ₇ Mg _{0,3})	Yes
43XXX	Al Si ₁₀ Mg	EN AC-43000 (Al Si ₁₀ Mg(a))	Yes
44XXX	Al Si	EN AC-44200 (Al Si ₁₂ (a))	Not possible
45XXX	Al Si ₅ Cu	EN AC-45000 (Al Si ₆ Cu ₄)	Partially
46XXX	Al Si ₉ Cu	EN AC-46000 (Al Si ₉ Cu ₃ (Fe))	Not possible
47XXX	Al Si(Cu)	EN AC-47000 (Al Si ₁₂ (Cu))	Not possible
48XXX	Al SiCuNiMg	EN AC-48000 (Al Si ₁₂ CuNiMg)	Not possible
51XXX	Al Mg	EN AC-51100 (Al Mg ₃ (a))	Not possible
71XXX	Al ZnMg	EN AC-71000 (Al Zn ₅ Mg)	Yes

3.2.6. Homogenization

After DC-casting the alloy has a certain as-cast structure. This is characterized by a large amount of eutectic phase along the GB's and large cell sizes. Those phases reduce the fracture toughness, but unlike macrosegregation can be minimised or eliminated by an appropriate heat treatment. Homogenization is the most widespread type of heat treatment for casting alloys [23]. Most of the time for wrought alloys the subsequent treatment is some sort of thermo-mechanical treatment like hot rolling. As homogenization increases the technological formability of the alloy, it is usually employed before those treatments.

The main goals during homogenization are:

- Dissolve soluble eutectic intermetallic particles
- Minimize microsegregation
- Precipitation of dispersoids
- Spheroidization of hard particles with sharp edges

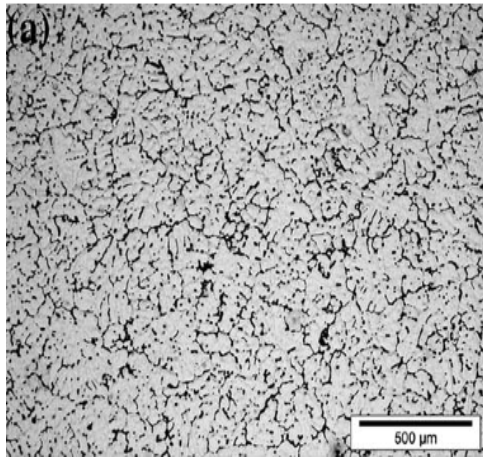


Figure 3.2-5 as-cast structure 7020 [24]

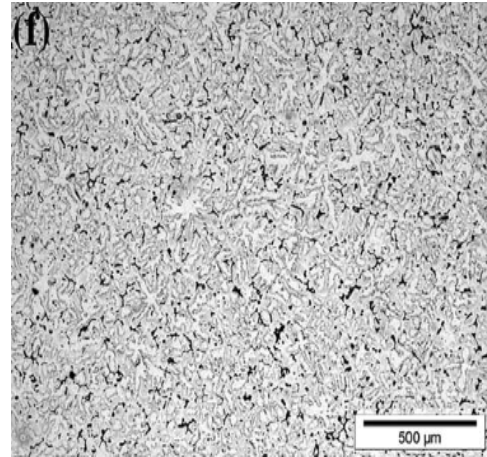


Figure 3.2-6 Homogenization for 2h at 550°C [24]

On the one hand the particles dissolve faster into the matrix at elevated temperatures on the other it is crucial that the highest temperature never exceeds the solidus temperature. Usually the maximum homogenization temperature is around 5°C beneath the incipient melting point [23], [25]. In Figures 3.2.6-1 and 3.2.6-2 we see that the large particles dissolve into the matrix, but new ones, like dispersoids, are formed during the homogenization process [24].

As mentioned earlier, during casting eutectic phases form at the GB's. These particles have low melting points and are referred to as low melting point phases (LMP's), they may cause incipient melting during hot deformation leading to a deterioration of the hot workability [26]. It should be mentioned that the main homogenization goal is the dissolution of the eutectic particles. But as high temperatures result in coarsening of the dispersoids a compromise has to be reached between the different goals. Recent studies have showed great progress in the 2 or 3-step homogenization treatment, which tries to combine the advantages of different temperature levels. Time is crucial in an industrial

process, hence an optimum treatment would also reduce the required homogenization time to an absolute minimum [27], [28], [29], [30].

3.2.7. Precipitation strengthening

In 1906 Wilm was the first to discover the precipitation strengthening effect in the Al-Cu system. The effect is caused by the fact, that one or more suitable elements are able to form particles (precipitates) with each other or together with the matrix material. They pose as lattice imperfection and depending on their size and distribution can increase the material strength substantially. Often the process is also called precipitation hardening. At solution heat treatment the alloys are in solid solution, to avoid the diffusion of the particles back out of the solid solution quenching is applied. This leads to a supersaturation of the matrix, freezing the elements and vacancies. At RT the elements start to unify to intermetallic compounds and grow (natural ageing), but better results are achieved at elevated temperatures (artificial ageing).

For an alloy to be heat treatable it has to contain a certain amount of soluble alloying elements, which exceed the solid solubility limit at RT [31], [32]. Hence not all aluminium alloys are heat treatable, only the 2xxx, 6xxx and 7xxx series [4]. Careful control of the precipitation process is essential, otherwise the hardening constituents and the inter-particle distances will become too large to significantly increase the material hardness.

3.2.8. Dispersoids

A dispersoid is a fine and stable second phase particle. An effective dispersoid needs to have a:

- High volume fraction
- Homogeneous distribution
- Certain thermal stability

To create a dispersoid, which satisfies all of those criteria poses a great challenge to current research. First the aforementioned solubility of the added elements has to be higher at elevated temperatures and lower at RT to be able to form precipitates. Microsegregation and macrosegregation have to be minimized as good as possible to ensure a homogeneous distribution. To ensure a high thermal stability a low solid solubility and diffusivity of the constituent solute atoms in the Al matrix has to be given [33], [34], [35].

The formation of dispersoids aims to improve the tensile properties of Al-Zn-Mg-Cu alloys. The enhanced mechanical properties can be explained by following strengthening mechanisms [36]:

- Dispersoid strengthening
- Fine-grain strengthening

Dispersoid strengthening:

When a dislocation line encounters dispersoids, which are incoherent to the matrix, they can either cut through them, if the particles are small enough (Figure 3.2.8-1), or they have to pass them (Figure 3.2.8-2).

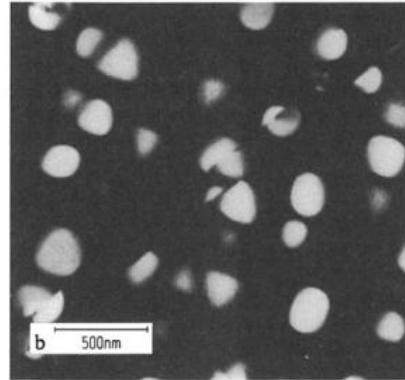


Figure 3.2-7 Cutting through small particles [37]

The shear mechanism creates new surface, which requires additional energy. This poses a higher energy barrier for the next dislocations and hence increases the strength of the alloy.

If it is no longer favourable to shear the particles a second effect comes into play. The Orowan mechanism.

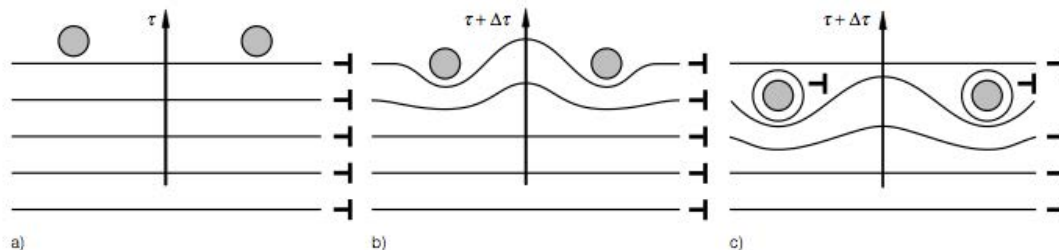


Figure 3.2-8 Orowan mechanism [33]

When the dislocation encounters the dispersoids it starts to bend, leaving behind a so-called Orowan-ring. This process can be explained by his well-known equation:

$$\tau_{Or} = \frac{2T}{bL} \quad (1)$$

Where τ_{Or} is the resulting critical shear stress, T is the line tension, b the Burgers vector of the dislocation and L the spacing between the obstacles.

Although further research has improved and altered the variables T and L, the core of the equation is still at the heart of mechanical metallurgy [38].

Fine-grain strengthening:

Dispersoids may retard the motion of grain boundaries by a process called the Zener drag. If a boundary wants to pass through an incoherent particle it is pinned by the particle. To move past it has to overcome a certain pinning pressure, described by the Zener pinning equation:

$$P_Z = \frac{3f\gamma_{GB}}{2r} \quad (2)$$

where r is the radius and f is the volume fraction of dispersoids, γ_{GB} is the energy of the boundary that the dispersoids are pinning. As we see in the equation a low radius and a high volume fraction will significantly increase the pinning pressure and achieve a high recrystallization resistance [39].

The Hall-Petch relationship describes the effect of average grain size on mechanical properties of a metal:

$$\sigma = \sigma_0 + kd^{-\frac{1}{2}} \quad (3)$$

where σ_0 is the lattice friction stress required to move individual dislocations, k is a material-dependent constant known as Hall-Petch slope and d is the average grain size [40].

As we can see, the smaller the average grain sizes the better the mechanical properties. Furthermore it significantly improves the creep resistance of alloys used in high temperature and pressure environments [34] [41].

Types of dispersoids

There are a number of different types of dispersoids depending on the alloy. In the 7xxx aluminium alloys a wide range of elements has been investigated. Yb, Pr, Sc, Mn, Ti, Zr and Cr are just a few elements often under investigation [36], [39], [41], [26].

We will focus on Zr and Cr as they are widely used in industrial application and are the main dispersoids in our alloys.

Zr-containing dispersoids

Zr and Al form the Al_3Zr dispersoid. There are two different forms of the Al_3Zr phase. Metastable $L1_2$ Al_3Zr and equilibrium DO_{23} Al_3Zr . The latter only forms after prolonged heat treatment (>450 °C and more than 500h) [41],[42], [43].

According to literature the metastable $L1_2$ Al_3Zr phase forms around 460°C after 24h or less [44], [45].

It also exhibits a low quench sensitivity compared to other minor element additions, making it a very interesting element as quenching is an essential part in the production of 7xxx alloys. The key problem with quenching sensitivity is the precipitation of, for instance Al_2CuMg or $MgZn_2$, which grow during slow cooling on locations such as grain boundaries. The formation of large amounts of quench-induced precipitates depletes the matrix of solute available for subsequent aging, leading to a significant decrease in mechanical properties after ageing [42]. It should be noted that due to the low diffusion rate of Zr in Al and their peritectic nature, they are usually found very inhomogeneously distributed. Furthermore Zr segregates into the grain leading to GB regions with few to no dispersoids. This causes local recrystallization [43], [46].

Cr-containing dispersoids

Only a scarce amount of literature about Cr dispersoids in the 7xxx alloy can be found. The Al_3Cr , the $Al_{12}Mg_2Cr$ and the $Al_{18}Mg_3Cr_2$ (E) are mentioned in relation to the 7xxx alloy. Just like the Al_3Zr the Al_3Cr is equiaxed with an average size up

to 100 nm, but they appear irregular in shape. [47] [48], [49]. The E-phase and the Al₁₂Mg₂Cr phase are incoherent with the matrix and large in size (compared to the Al₃Zr), but also irregular in shape [50], [51]. It's crystal structure is a disordered form of the ideal cubic structure (Fd3m) [52].

The Cr and Zr-dispersoids show partial substitution of alloying elements for instance Mg, Cu and Zn can be dissolved in the Al₃Zr, substituting for Al [39], [52].

3.2.9. Phases

7020, 7475, 7050 and Titanal have different compositions leading to the formation of various phases along the heat treatment process.

Table 3.2.9-1 gives a short oversight of which phases to expect in which alloy

Table 3.2.9-1 Expected phases according to literature in the 7020, 7475, 7050 and TITANAL alloy

Symbol	Name	7020	7475	7050	Titanal	Ref.
M (η)	MgZn ₂ or Mg(Al,Cu,Zn) ₂	X	X	X	N/A	[53][26][27]
β	Mg ₂ Si	X	X	X	N/A	[54][26][55]
T	Al ₂ Mg ₃ Zn ₃	X	X	X	N/A	[26][55][55]
S	Al ₂ CuMg	X		X	N/A	[26][56]
θ	Al ₂ Cu	X		X	N/A	[26][56]
Z	Mg ₂ Zn	X			N/A	[26]
	Al ₆ CuMg ₄	X			N/A	[26]
	Al ₇ Cu ₂ Fe	X		X	N/A	[27][55]
	Al ₃ Zr	X		X	N/A	[27][57]
E	Al ₁₈ Mg ₃ Cr ₂	X	X		N/A	[58][57]
	Al ₁₂ Mg ₂ Cr		X		N/A	[50]
	Al ₃ Cr		X		N/A	[59]
	Al ₇ Cr	X			N/A	[26]
	Al-Fe-Si	X			N/A	[26]
	Al-Fe-Mn-Si	X			N/A	[26]

4. Experimental

All investigated probes come from industrial DC cast ingots, which were homogenized under laboratory conditions according to a given procedure. Subsequent to the thermal treatment a metallurgical sample preparation was carried out to prepare all samples for a TEM (Transmission Electron Microscope) and STEM (Scanning Transmission Electron Microscope) analysis. Along with a TEM and STEM analysis an energy dispersive X-ray (EDX) spectroscopy was carried out to determine the chemical composition of selected particles. Via EELS mode, thicknesses were calculated in order to derive the number density (ND) of dispersoids in certain probes.

4.1. Materials and Homogenization

Four different 7xxx aluminium alloys were examined with different thermal treatments. A total of 33 specimens were analysed, each of them taken at a different temperature level from the respective alloy.

- 7020: 6 Samples
- 7475: 9 Samples
- 7050: 11 Samples
- TITANAL: 7 Samples

Apart from the TITANAL alloy, which is a special brand with its own chemical composition, all alloys can be found in the DIN 573-3.

4.1.1. Materials / Samples

All alloys under investigation are industrial DC electromagnetically cast (EMC) alloys.

Position of the etched slices within the ingots:

- Stationary casting condition, 400 mm from the casting end
- Parallel edge distance of 75 mm in respect to the cast surface (1/4 of the thickness), therefore: 65-75 mm; 75-85 mm

Tabel 4.1.1-1 shows the chemical composition of all aluminium alloys according to DIN EN 573-3 and the actual chemical compositions.

For a better understanding of the tables following rules should be considered:

- The chemical composition of aluminium and aluminium alloys is shown as percentage by weight.
- Maximum permissible values of impurities are shown as limits.
- Concentration of alloy components are given as range

- **Table 4.1.1-1 Chemical composition of alloys: 7020, 7475, 7050 and TITANAL**

EN AW-7020

Si	Fe	Cu	Mn	Mg	Cr	Zn	Ti	Zr	Al	Notes
0,35	0,4	0,2	0,05-0,5	1,0-1,4	0,1-0,35	4,0-5,0	-	0,08-0,2	Rem.	^b

ACTUAL ALLOY

CONFIDENTIAL^a

EN AW-7475

Si	Fe	Cu	Mn	Mg	Cr	Zn	Ti	Zr	Al	Notes
0,1	0,12	1,2-1,9	0,06	1,9-2,6	0,18-0,25	5,2-6,2	0,06	-	Rem.	

ACTUAL ALLOY

CONFIDENTIAL^a

EN AW-7050

Si	Fe	Cu	Mn	Mg	Cr	Zn	Ti	Zr	Al	Notes
0,12	0,15	2,06-2,6	0,1	1,9-2,6	0,04	5,7-6,7	0,06	0,08-0,15	Rem.	

ACTUAL ALLOY

CONFIDENTIAL^a

TITANAL

Si	Fe	Cu	Mn	Mg	Cr	Zn	Ti	Zr	Al	Notes
NO REFERENCE										

ACTUAL ALLOY

CONFIDENTIAL^a

^a Property of AUSTRIA METALL AG (AMAG). Please contact AMAG for further information

^b 0,08-0,2 Zr, 0,08-0,25 Zr + Ti

TITANAL

As the TITANAL alloy is a custom aluminium alloy of AMAG the chemical composition is not listed in the DIN EN 573-3.

The investigated material is an industrial DC electromagnetically cast (EMC) aluminium alloy named TITANAL with high levels of Zn and Zr.

Properties²:

R_m [MPa]: > 600

$R_{p0,2}$ [MPa]: > 550

A_{50} for T6 [%]: 5-12

4.1.2. Homogenization

The etched slices were thereafter exposed to a homogenization treatment using a laboratory chamber furnace³, which was designed according to the industrial process.

After the laboratory thermal treatment the samples were abstracted from the furnace and immediately quenched in water to RT.

Figure 4.1.2-1 to Figure 4.1.2-4 represent the time-temperature curves of the homogenization processes. Along the time-temperature curve the specimens are marked with P1-Px representing the microstructural development of the alloy at different stages in the homogenization process.

Figure 4.1.2-5 compares the different homogenization processes regarding time and temperature.

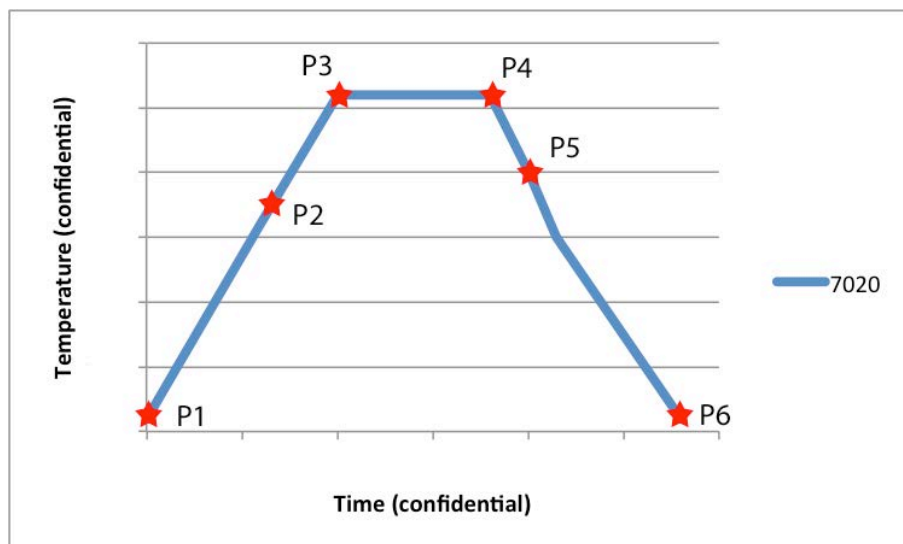


Figure 4.1-1 7020: Homogenization process including withdrawal of samples

² <https://www.amag.at/unser-aluminium/sportartikel-konsumgueter/sportartikel/amag-titanalr.html>

³ Thermal treatment was preformed by AUSTRIA METALL AG (AMAG)

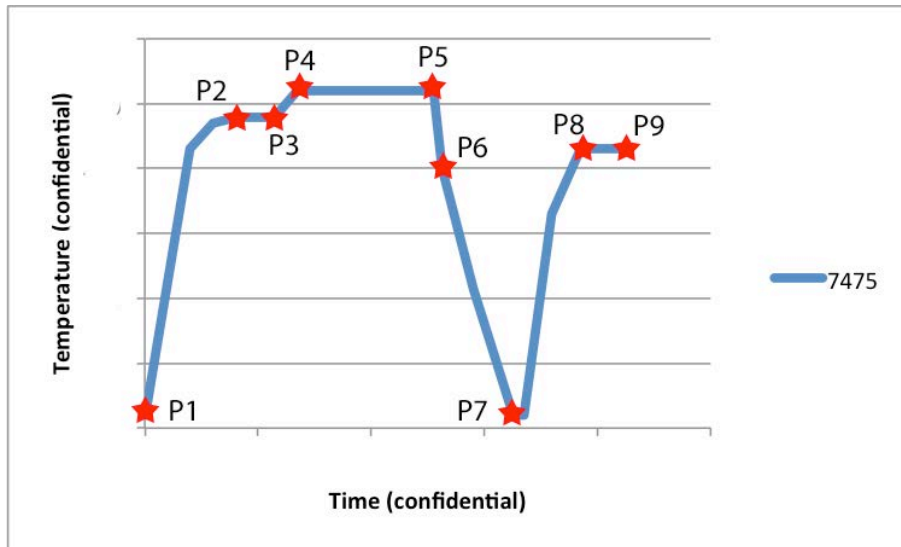


Figure 4.1-2 7475 Homogenization process including withdrawal of samples

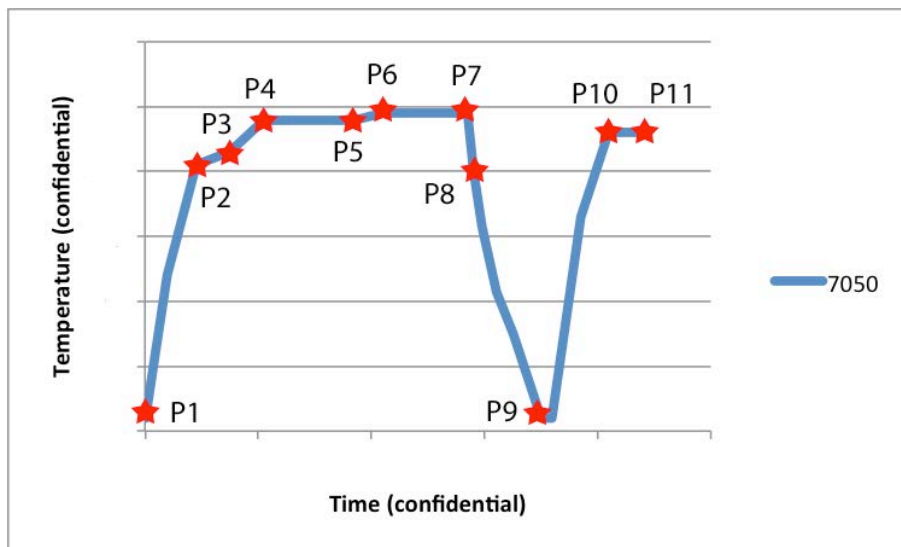


Figure 4.1-3 7050 Homogenization process including withdrawal of samples

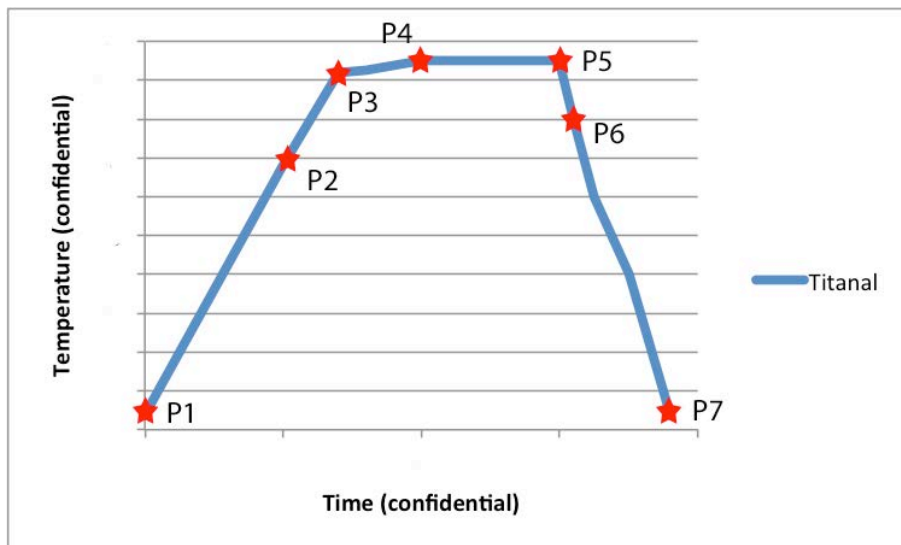


Figure 4.1-4 Titanal Homogenization process including withdrawal of samples

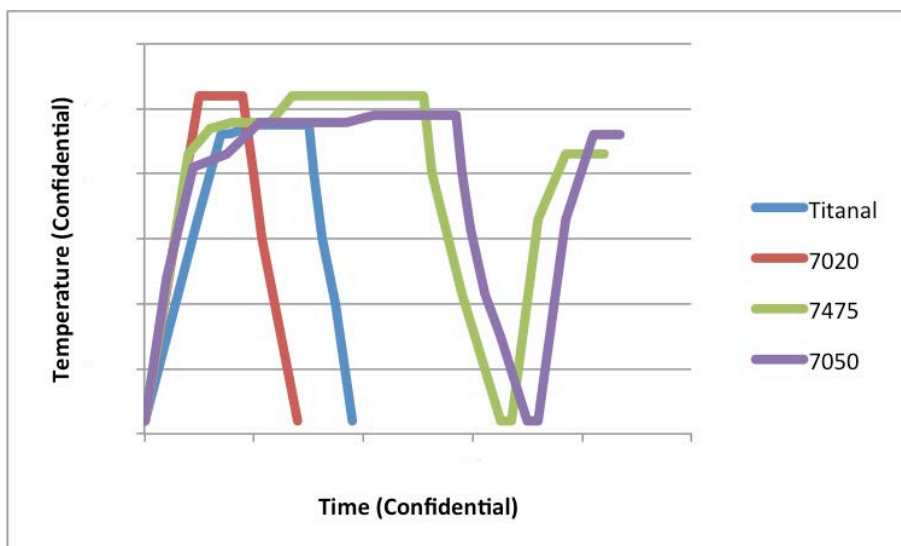


Figure 4.1-5 Homogenization processes in comparison

All specific treatment parameters are confidential and property of the *AUSTRIAN METALL AG (AMAG)*. Please contact *AMAG* for further information.

4.2. Sample Preparation

A 0,5-1 mm thick plate was cut of the etched slices with a precision table top cut-off machine (STRUERS ACCUTOM-50). The plates were then glued to a glass specimen holder. We referred to this specific method to avoid any additional probe exposure to temperatures above 100°C, which usually occur during the embedment with wax.

Subsequently the plates were polished with silicon carbide paper until a thickness of 150 µm was reached. A round sample with a radius of 3 mm was punched out of the plate.

In many studies the samples were twin-jet electro polished at 243K (-30 °C) with different compositions of acids [39], [44], [55]. It was refrained from this method due to the uncertain impact on the dispersoids. Dimpling was the chosen procedure to prepare the specimen for TEM. The mechanical method ensures that the microstructure will be preserved, as there is no unnecessary chemical or thermal exposure to the sample. The 3 mm disc is glued at the center of a small cylindrical support mounted on a rotating plate with adjustable speed. A grinding tool is brought to the specimen perpendicularly. A paste containing the diamond abrasive is applied to the tool specimen interface. The dimple is created through the rotating motion of both the plate and the tool, with a thickness of roughly 15 µm.

Using a Precision Ion Polishing System (PIPS) *Gatan Model 691* the probes were further thinned until a small cavity appeared. Along the edge of this cavity we find regions thin enough for a TEM analysis.

4.3. Transmission Electron Microscopy, Energy Dispersive X-Ray Spectroscopy and Electron Energy-Loss Spectrum

The analysis of the probes was done on a FEI Tecnai F20 transmission electron microscope. The operation voltage was 60-200 kV. All specimens were prepared as described in chapter *SAMPLE PREPARATION*. TEM, STEM, EDX and EELS were used to derive the distribution, chemical composition and thickness of the particles and the specimen in general. Every phase was analysed multiple times on different areas within the sample. Since some phases are very rare they could not be found more than once within a specimen. The missing error bar in the bar charts represents this.

The number density and sizes of the particles was analysed using the image and photo editing software *PAINT.NET*⁴. With EDX analysis and corresponding literature the different phases were identified.

4.3.1. TEM

Light has a certain wavelength and according to the Reyleigh-criterion the maximum magnification where two points are still distinguishable is :

$$r_{ray} = \frac{0,61\lambda}{A_N} \quad (4)$$

Where λ is the wavelength and $A_N = \mu \sin\theta$ the numerical aperture with the refraction index μ and the half angle θ of the projection lens. For visible light this is roughly 0,2 µm. As we are interested in very small particles with diameters far smaller than 0,2 µm we turn to a transmission electron microscope, which can

⁴ <http://www.getpaint.net/>

achieve resolutions of 0,1 nm. This is due to the much smaller wavelength of electrons. De Broglie discovered this fact and postulated the equation :

$$\lambda = \frac{h}{p} \quad (5)$$

where λ is the wavelength, h the Planck's constant and p the momentum.

TEM is an imaging technique whereby a beam of electrons is focused on a specimen to produce a magnified image.

A Transmission Electron Microscope consists of an electron source, a condensor-system, a sample chamber, a projection system and a fluorescent screen or CCD-camera.

The TEM mode was used to capture greater areas, giving a good oversight of the particle distribution within the grain [60].

4.3.2. STEM

Scanning Transmission Electron Microscopy is a type of TEM. The electron beam is focused on a very narrow spot, which is then scanned over in a raster. The signal of the spots is captured by detectors beneath the probe and put together as a picture on the PC screen. The scattering cross section strongly depends on the atomic number Z , that's why heavy elements have a stronger signal than light ones (Z -contrast). Chemical compositions are made observable via the level of brightness. Within the STEM mode it is possible to focus the beam on a desired spot and capture an EDX spectrum [61].

This mode was the chosen method for analysing particles and close-up views.

4.3.3. EDX

If a high-energy beam of electrons hits a sample it will put it into an "excited" state (e.g. a excited electron leaves a inner shell creating a electron hole which is then filled by an electron from an outer shell). By moving to a lower energy level, energy is released via an X-ray. Due to the unique atomic structure of the elements the X-ray emission spectrum shows a unique set of peaks. Hence the chemical composition can be derived from the EDX spectrum. The method strongly depends on the atomic number of an element, making it quite suitable for heavy but not so much for light elements [61].

We used the EDX mode to identify the different particles according to their spectrum.

4.3.1. EELS

The beam of electrons has a known range of kinetic energy, when they hit the sample some electrons will undergo inelastic scattering, meaning they loose energy and are randomly deflected. The amount of energy loss can be detected and interpreted in terms of what caused the energy loss. EELS is used to calculate the thickness of a certain region. For this we use the Log-Ratio method.

Within our number density areas we have regions with different thicknesses. Thickness measurements were placed in the center of said areas to balance the thickness variation within the image [62].

5. Simulation

The simulation was done with *MatCalc – The Materials Calculator*⁵. *MatCalc* is a scientific software for computer simulation of constrained and unconstrained phase equilibria, precipitation kinetics, long-range diffusion, phase transformation and a few more processes.

Version MatCalc 5.61.1003 was used for all alloys along with the thermodynamic database for aluminium (version 2.010) and the diffusion mobility database (version 2.004). The different investigated alloys were constructed with the same chemical compositions as the actual alloys (see Table 4.1.1-1).

The as-cast probes were used to identify all already existing phases. This information was then inserted into the *MatCalc* program and used as a starting point for the simulation. The final results from *MatCalc* were compared to the findings of this thesis to verify the elaborateness of the simulation.

⁵ <http://www.matcalc.tuwien.ac.at>

6. Results

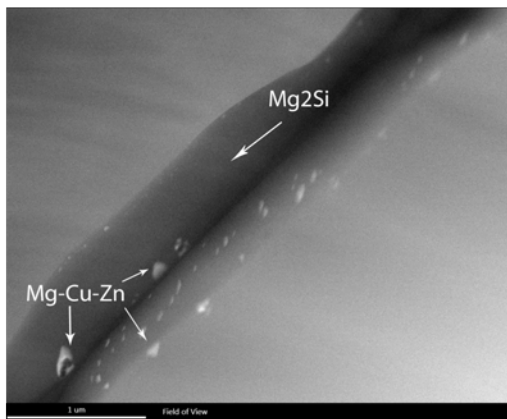
6.1. 7020

6.1.1. As-cast structure

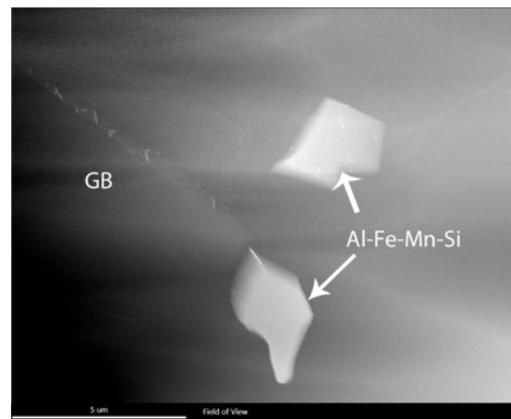
In the as-cast structure Mg-Cu-Zn, Mg-Si and Fe-containing phases were identified as the dominant phases.

On the GB we find large Mg-Si particles together with the Mg-Cu-Zn phase (Figure 6.1.1-1 (a)). The Mg-Cu-Zn phase only contains traces of Cu.

The intermetallic particles (see Figure 6.1.1-1 (b)) consist mainly of the elements Al, Fe, Mn, Si with traces of Cr and are referred to as Al-Fe-Mn-Si-Cr. Quite a few of them were encountered (>10) and they tend to be very coarse (some larger than 1 μm). They were found on GB's and within the grain.



(a) Sample 1

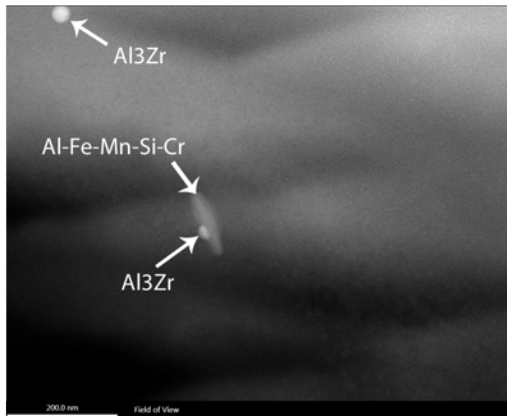


(b) Sample 1

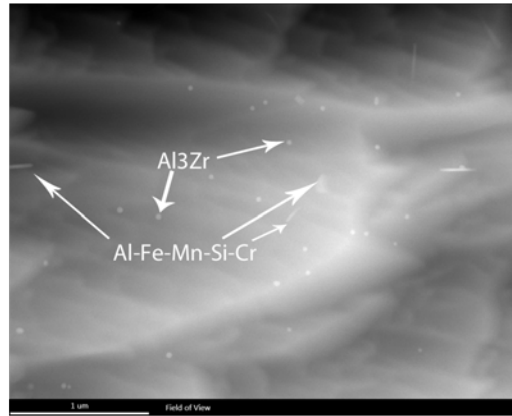
Figure 6.1-1 As-cast structure [7020]

6.1.2. Dispersoids

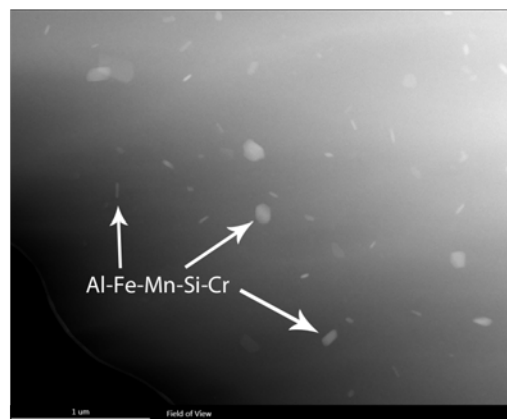
The first Zr-containing dispersoid was encountered in P3 at which the temperature level already exceeded 500°C. The few dispersoids within the matrix are found to nucleate on Fe-containing particles as seen in Figure 6.1.2-1 (a). At P4, P5 and P6 the amount of dispersoids gradually increases. They precipitate within the grain and can now be found in various areas. Nevertheless neither in P4 nor in P6 a homogeneous nucleation was observed. Many regions seem to have a high number density of Zr-containing dispersoids while in others no dispersoid at all was detected. This is very obvious if we compare Figure 6.1.2-1 (c) with (d). While a large number of dispersoids was detected in (c), not a single one was found in (d). All other samples showed the same characteristic.



(a) Sample 4



(b) Sample 5



(c) Sample 5

Figure 6.1-2 Dispersoid images [7020]

Due to the fact that the dispersoids were very inhomogeneously distributed it was impossible to derive a reasonable ND count. Hence only the dispersoid size evolution was documented via *Paint.NET*⁶. A mean dispersoid radius was calculated out of all counted dispersoids, depicting the dispersoid growth.

Especially in P4 and P5 most of the encountered dispersoids were very far apart (sometimes only one was found within a region). This made it necessary to work with absolute numbers instead of the mean from each analysed section. Due to this fact no error bar can be found on the bar chart of Figure 6.1.2-2.

In Figure 6.1.2-3 we find the mean radius of all counted Al_3Zr particles in each sample showing an error bar, which depicts the standard deviation.

Figure 6.1.2-4 shows the mean radius and the size of the smallest and largest dispersoid.

⁶ <http://www.getpaint.net/>

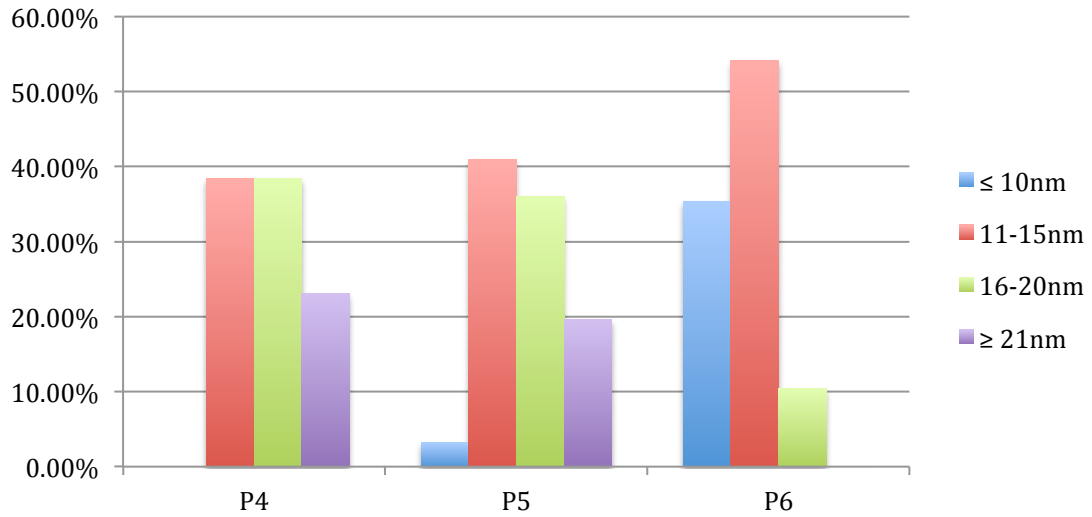


Figure 6.1-3 Dispersoid radius [7020]

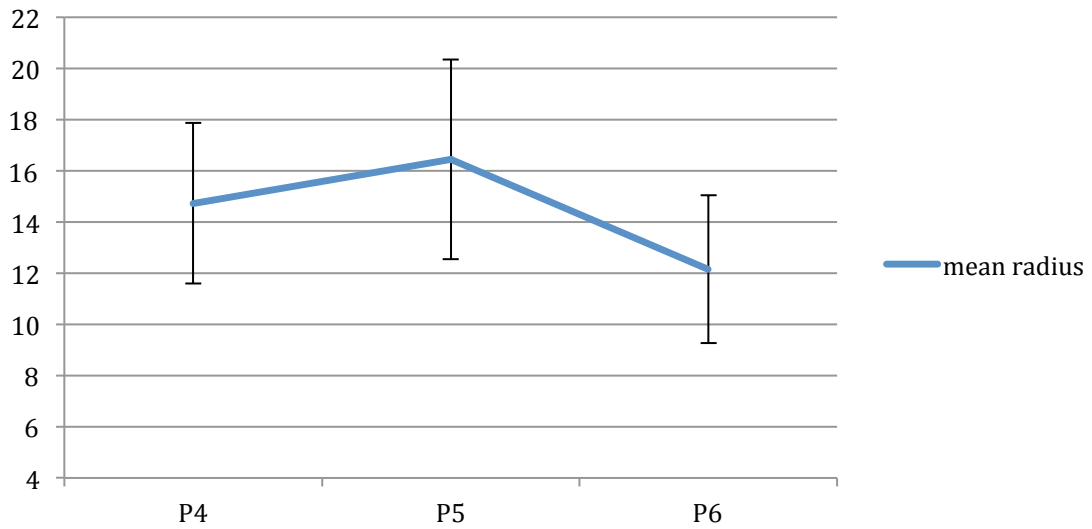


Figure 6.1-4 Mean dispersoid radius [7020]

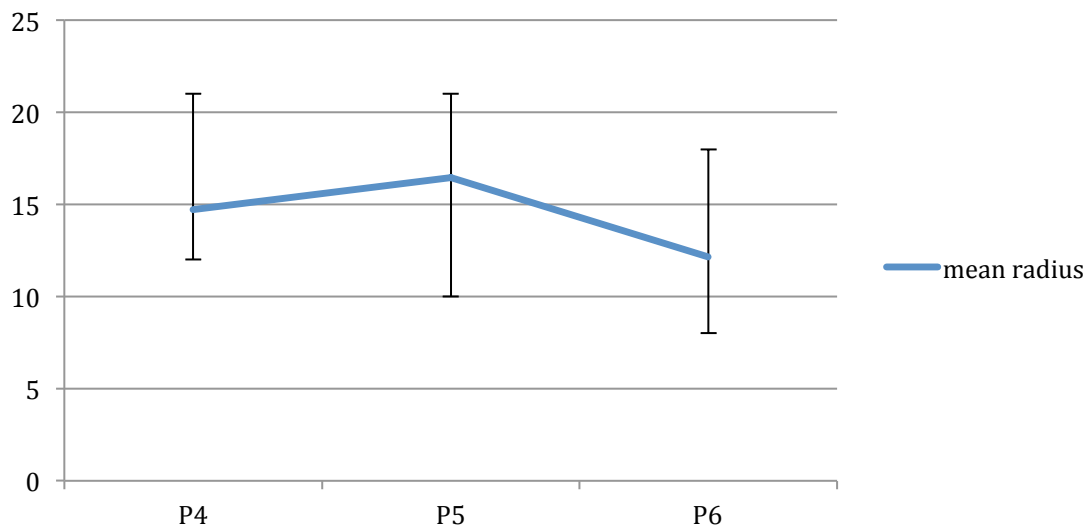


Figure 6.1-5 Mean radius depicting the smallest and largest dispersoid radius [7020]

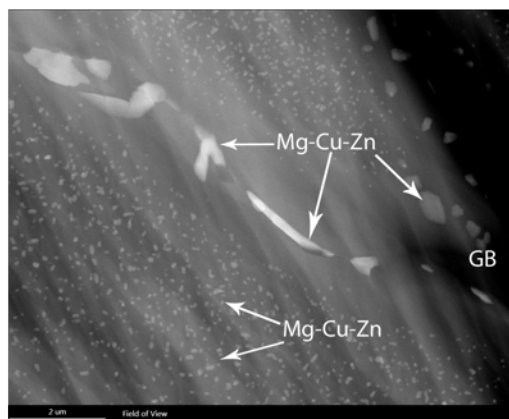
6.1.3. Other Phases

The main second phase is the Mg-Cu-Zn phase. This phase consists of Mg and Zn and contains traces of Cu. It dissolves at P3 only to precipitate back at P6. This indicates that its formation is taking place at slightly elevated temperatures (between 20°C and 350°C) and dissolves at temperatures above 400°C. Some coarse Mg-Cu-Zn phase was encountered in P3 and P5, but it is assumed that those particles precipitated back due to an insufficient cooling rate and are normally not present at those temperatures. We find that the Mg-Cu-Zn phase precipitates very homogeneously near the grain boundary as seen in Figure 6.1.3-1 (a) and can have all sorts of sizes and shapes (b).

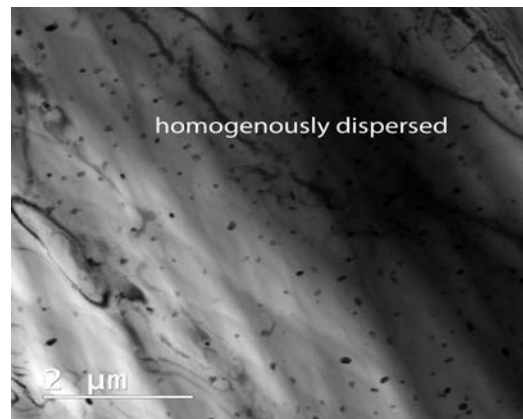
The intermetallic particles were found in almost all samples and did not dissolve during the homogenization process. Some contained Cr and in Figure 6.1.3-2 (c) and (d) their chemical development and the development of all other phases throughout the process is listed.

The Mg-Si was only encountered in samples with temperatures below 500°C. Furthermore a Cr-containing and a Ti containing phase were encountered. Those particles were large in size and irregular in shape. There was only one particle in each sample to be found.

Ni-Cu particles were found in P2 but as they are regarded as contamination, they were not further investigated.



(a) Sample 2

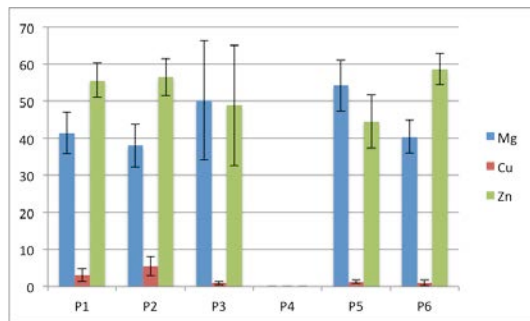


(b) Sample 2

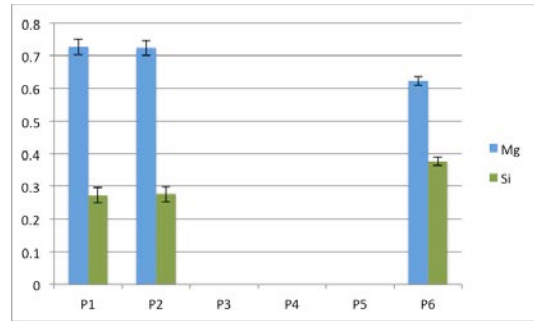
Figure 6.1-6 TEM/STEM images of other phases [7020]

Table 6.1.3-1 Encountered Phases [7020]

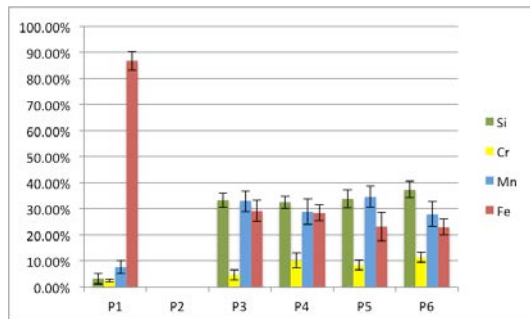
Encountered Phases	Sample #					
	1	2	3	4	5	6
Mg-Cu-Zn	X	X				X
Mg-Si	X	X				X
Fe-Mn-Si-Cr	X		X	X	X	X
Fe-Mn-Si	X	X	X	X		
Ti				X		
Cr (traces of Ti)			X		X	
Zr			X	X	X	X



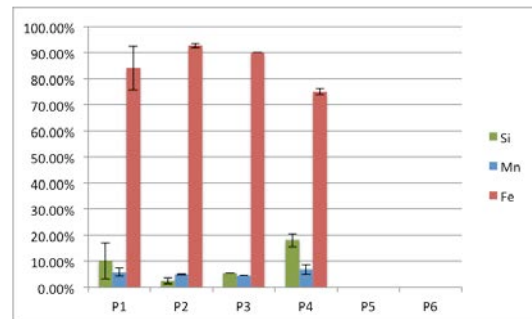
(a) Mg-Cu-Zn [atomic %]



(b) Mg-Si [atomic %]



(c) Fe-Mn-Si-Cr [atomic %]



(d) Fe-Mn-Si [atomic %]

Figure 6.1-7 Chemical composition of obtained phases [7020]

6.2. 7475

6.2.1. As-cast structure

Mg-Cu-Zn and Mg-Cu are the predominant phases in the as-cast structure of the 7475 alloy. The matrix is filled with irregular shaped Mg-Cu-Zn and needle shaped Mg-Cu particles, as seen in Figure 6.2.1-1 (a). Large eutectic phases,

clearly visible thanks to their lamellar structure, occupy the GB's (Figure 6.2.1-1 (b)). They too consist of Mg-Cu-Zn. Some Mg-Si particles were encountered but much smaller in size and less frequent than in the 7020 alloy.

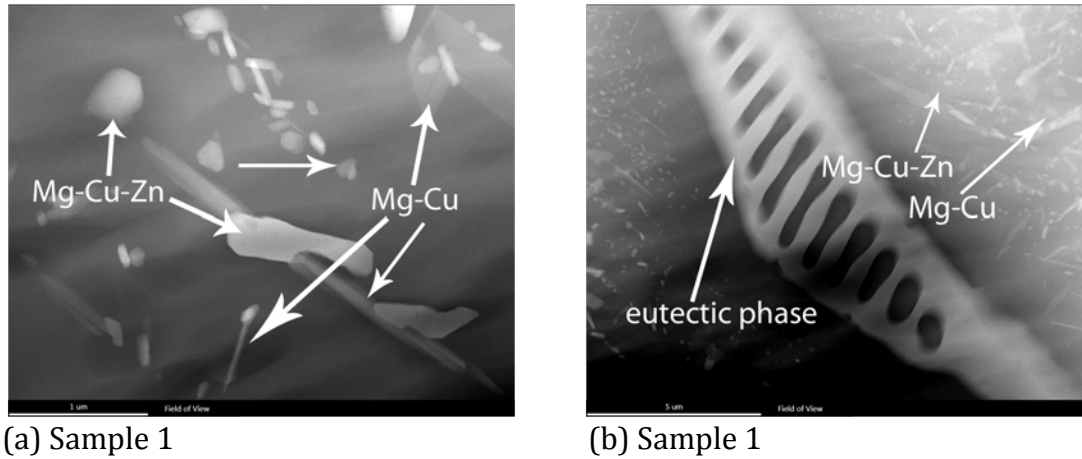


Figure 6.2-1 As-cast structure [7475]

6.2.2. Dispersoids

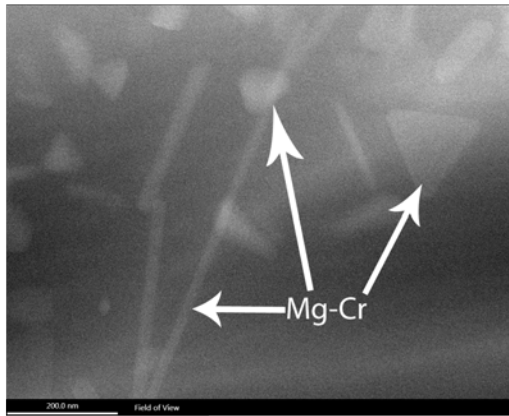
Instead of a Zr-containing dispersoid the 7475 alloy has a Mg-Cr containing one, which was first encountered in P2 at a temperature level above 460°C and a homogenization time of more than 15 hours. From P2-P4 the ND of the dispersoid increases constantly. In sample 4 the matrix is homogeneously filled with a large number of dispersoids and we were able to conduct our first ND count as depicted in Figure 6.2.2-2.

Figures 6.2.2-1 (a) and (b) show the various shapes and the homogeneous distribution.

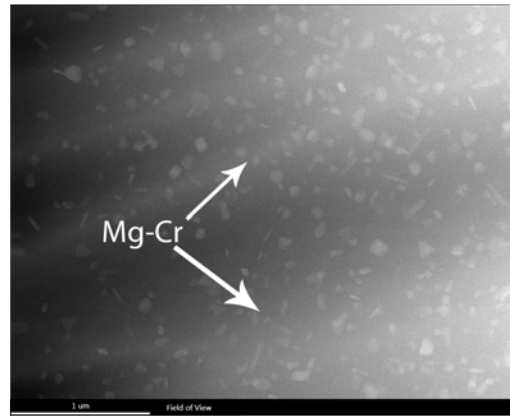
Often times the dispersoids were encountered with little caps (Figure 6.2.2-2 (c)), which seemed to nucleate on them. Those caps consist of Mg-Cu-Zn and have different sizes. They were also encountered in P4 and P9, at temperature levels far above the dissolution rate of the Mg-Cu-Zn phase, and are assumed to nucleate on the Mg-Cr dispersoids as result of a slow cooling rate.

In Figure 6.2.3-2 (e) we find the chemical composition of the Mg-Cr dispersoid. In some of dispersoids traces of Ti were encountered but those traces were too low to be visible in the bar chart.

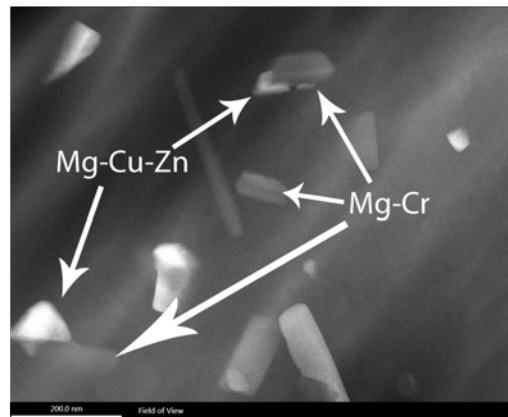
Due to the various shapes of the Cr dispersoid it was not possible to quantify the size evolution as no respective mean radius can be derived. Via optical inspection no distinct coarsening effect can be observed.



(a) Sample 3



(b) Sample 5



(c) Sample 7

Figure 6.2-2 Dispersoid images [7475]

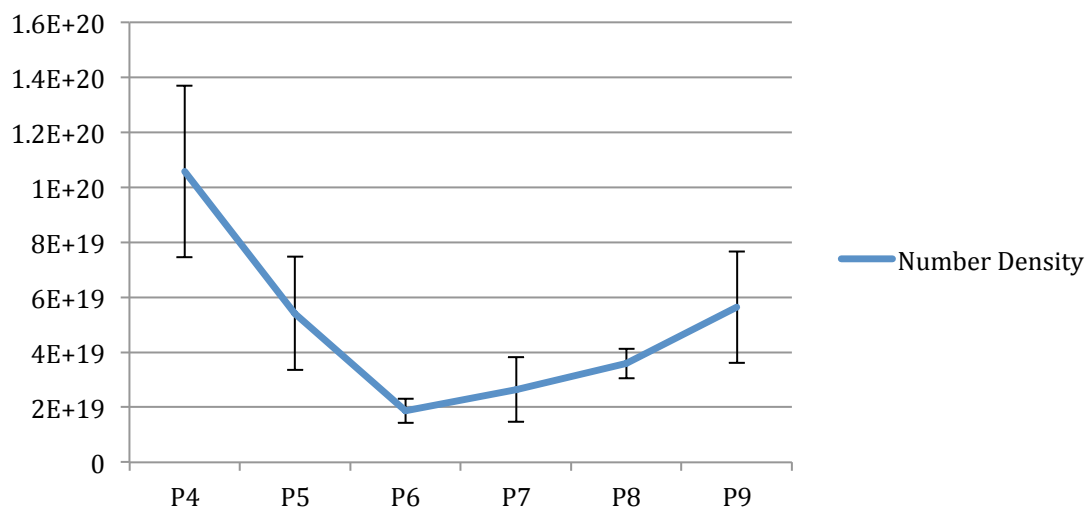


Figure 6.2-3 Number Density [dispersoid per m³]

6.2.3. Non-dispersoid phases

The Mg-Cu-Zn phase with low amounts of Cu has already dissolved back into the matrix at P2 and, as mentioned earlier, all other Mg-Cu-Zn phases encountered between P2 and P5 are due to an insufficient quenching rate. Given that the Cu-low Mg-Cu-Zn phase precipitates back at P6 (Figure 6.2.3-1 (a)) but dissolves into the matrix at P8 we can assume that they start to dissolve at temperatures above 400°C. Unlike the Mg-Cu-Zn phase with low amounts of Cu the Mg-Cu-Zn phase with high amounts of Cu stays present in the matrix at P2, P8 and P9 (Figure 6.2.3-1 (b)) at temperatures above 400°C.

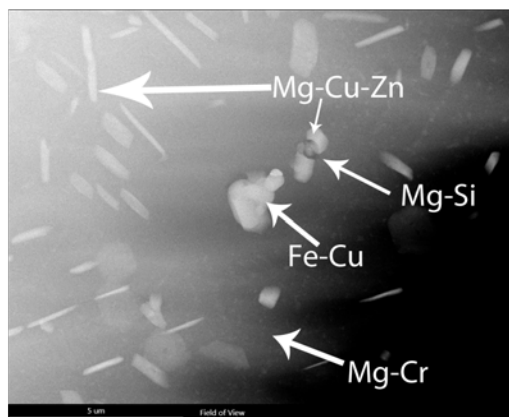
A Mg-Cu phase with similar Mg and Cu amounts (at. %) was encountered in P1 but has already dissolved in P2. The Mg-Cu particles in P2 and P3 show very high levels of Cu and only a few of them near GB's were detected.

Fe-containing particles were found in almost all samples irrespective of the homogenization temperature. Most of them consisted of Fe and Cu, but Mn, Cr and even Ni were also part of some of the particles.

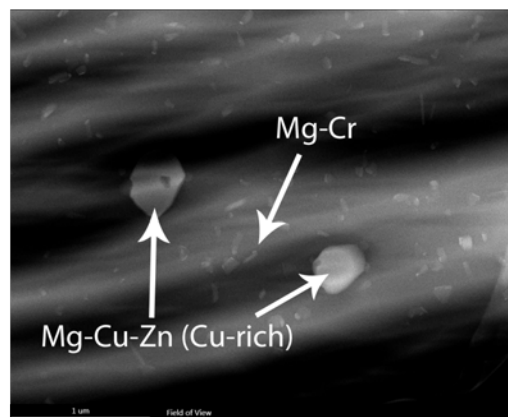
The Mg-Si phase was only present in samples with temperatures below 460°C and similar to the intermetallic particles only a few of them could be found.

Additionally to the mentioned phases we found Ti particles in P4, P5, P7, P8 and P9.

Contamination in form of Pb and Ag containing particles was also encountered but not further investigated.



(a) Sample 6

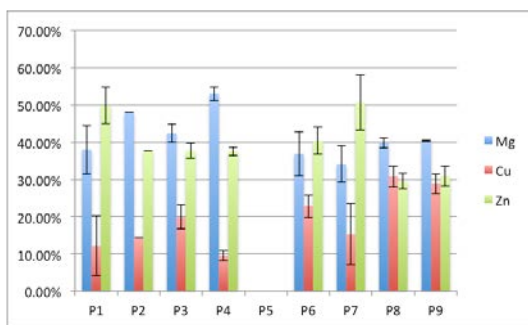


(b) Sample 9

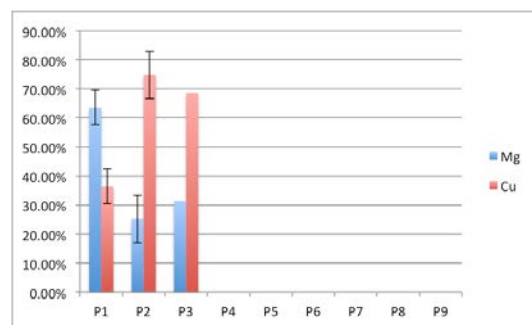
Figure 6.2-4 TEM/STEM images of other phases [7475]

Table 6.2.3-1 Encountered phases [7475]

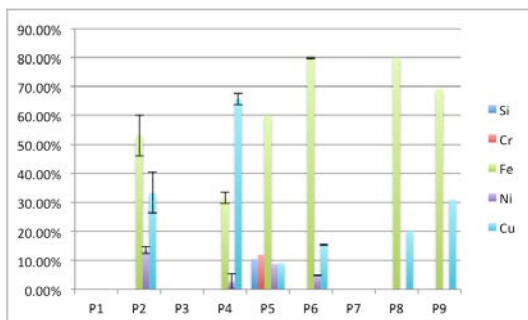
Encountered Phases	Probe #								
	1	2	3	4	5	6	7	8	9
Mg-Cu-Zn	X	X				X	X	X	X
Mg-Cu	X	X	X						
Mg-Si	X					X	X	X	X
Intermetallic		X		X	X	X		X	X
Ti				X	X		X	X	X
Mg-Cr		X	X	X	X	X	X	X	X



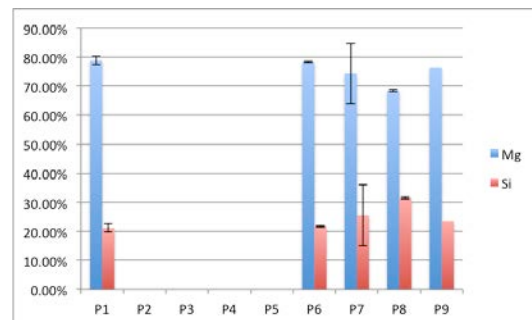
(a) Mg-Cu-Zn



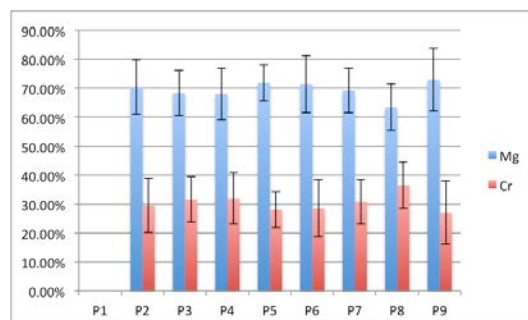
(b) Mg-Cu



(c) Intermetallic



(d) Mg-Si



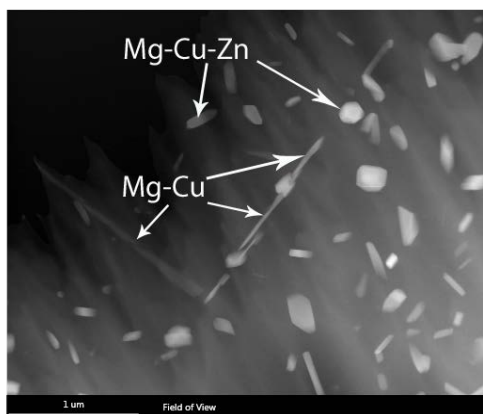
(e) Mg-Cr

Figure 6.2-5 Chemical composition of the encountered phases [7475]

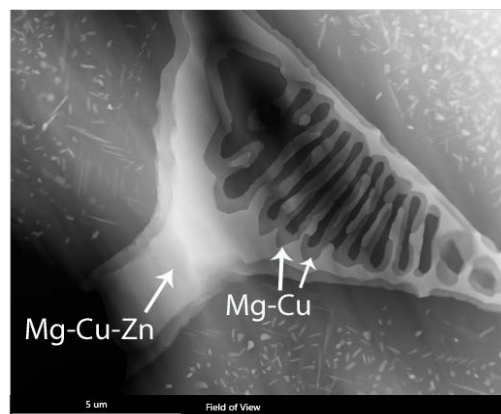
6.3. 7050

6.3.1. As-cast structure

In the as-cast structure we find an ample amount of Mg-Cu-Zn and Mg-Cu phase as seen in Figure 6.3.1-1 (a). Similar to the 7475 alloy the Mg-Cu-Zn particles are irregular-shaped while the Mg-Cu phase is needle-shaped. The GB's are covered with eutectic phase consisting of a bright Mg-Cu-Zn phase and a grey Mg-Cu phase. Just one Mg-Si particle was detected.



(a) Sample 1

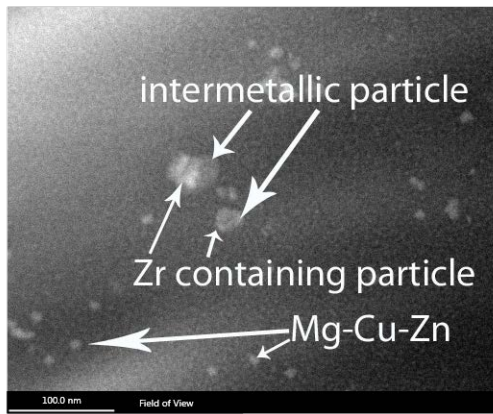


(b) Sample 1

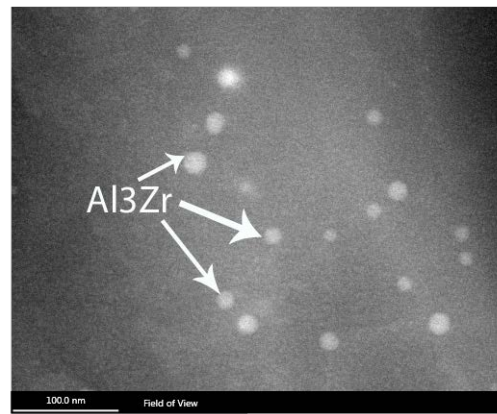
Figure 6.3-1 As-cast structure [7050]

6.3.2. Dispersoids

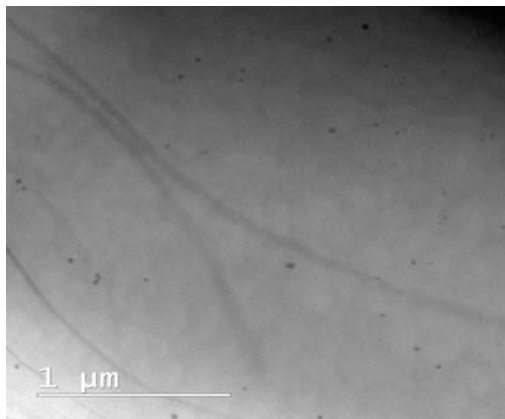
The first Zr-containing dispersoid was encountered in P3 at temperatures above 420°C and a homogenization time of 15 hours. Those dispersoids are encountered on Fe-containing particles as seen in Figure 6.3.2-1 (a). The nucleation of dispersoids on intermetallic particles was already observed in the 7020 alloy. From P3-P6 the dispersoids seem grow in in number and size until enough Zr-containing particles were found in P6 to conduct the first ND count (Figure 6.3.2-1(b)). Although the ND still varies across the grain, Zr-containing particles can be encountered in all areas. Figure 6.3.2-1 (c) and (d) provide a good comparison to illustrate the deviant behaviour of dispersoids across a grain.



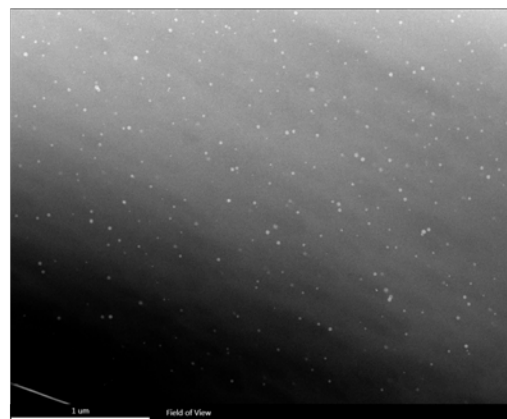
(a) Sample 3



(b) Sample 6



(c) Probe 7



(d) Probe 7

Figure 6.3-2 Dispersoid images

Figure 6.3.2-3 and Figure 6.3.2-5 provide an oversight regarding the sizes of the analysed dispersoids. It can be seen that the smallest dispersoid radius of 5 nm can be found in all samples, while the largest radius constantly increases with time and temperature.

The sudden increase of ND from P9 to P10 is accompanied by a decrease of the mean radius. From P10 to P11 the inverted process can be observed.

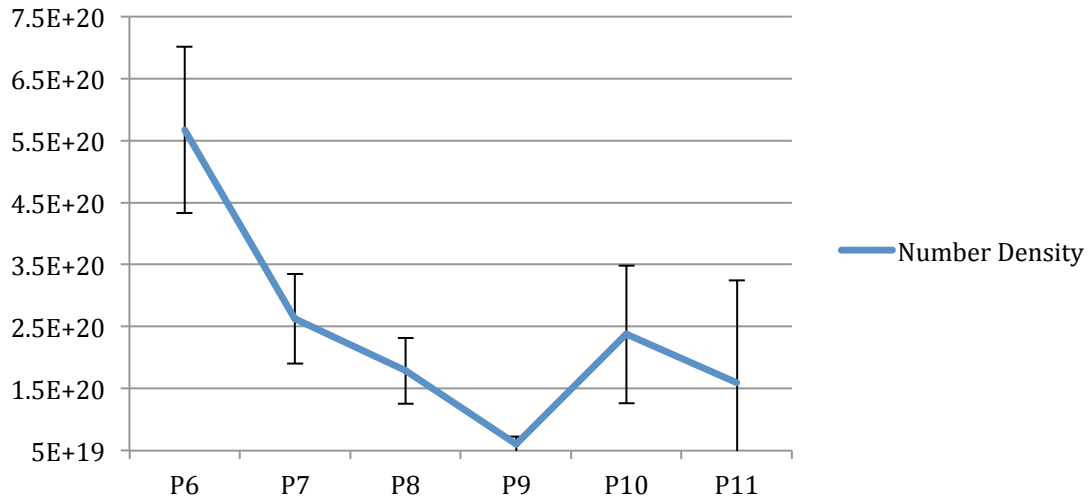


Figure 6.3-3 Number Density (dispersoids per m³) [7050]

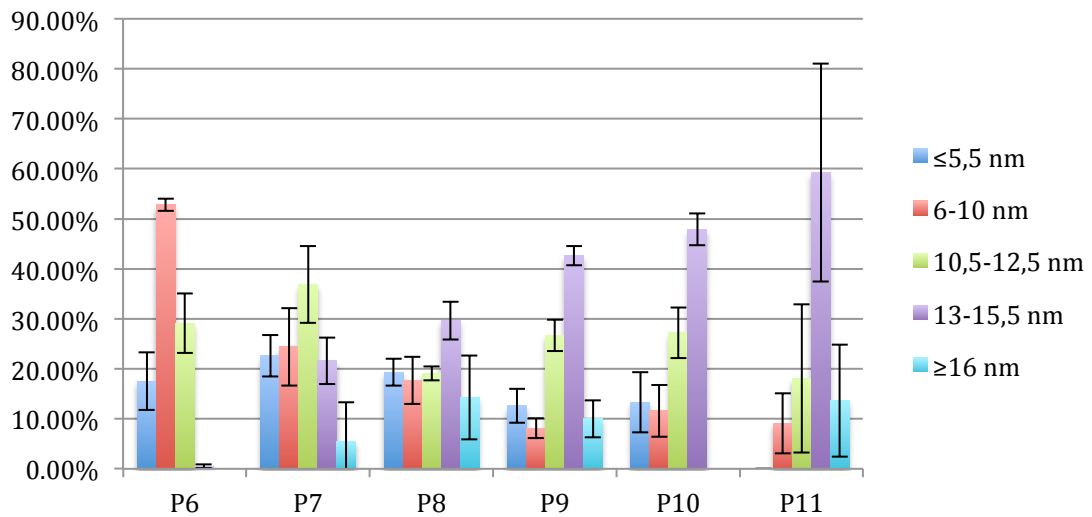


Figure 6.3-4 Dispersoid radius [7050]

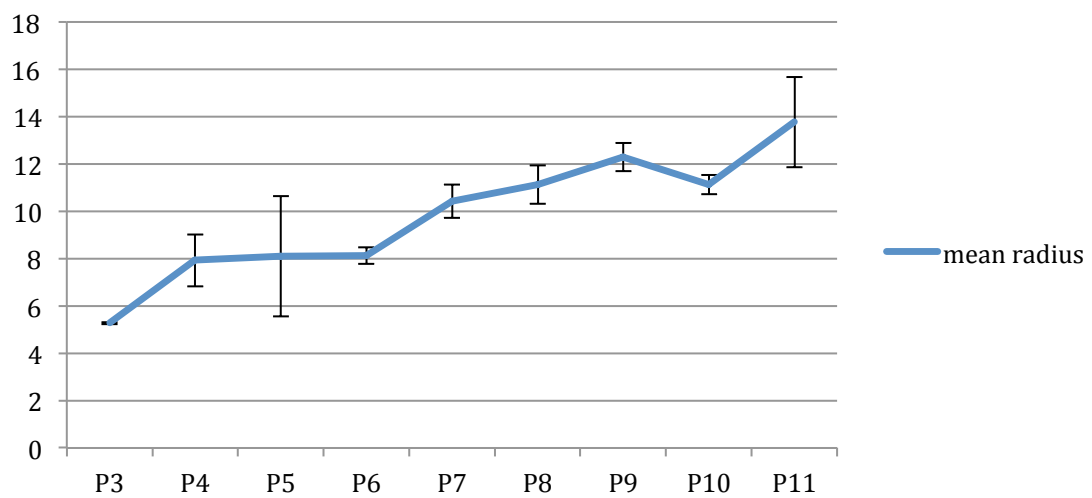


Figure 6.3-5 mean dispersoid radius [7050]

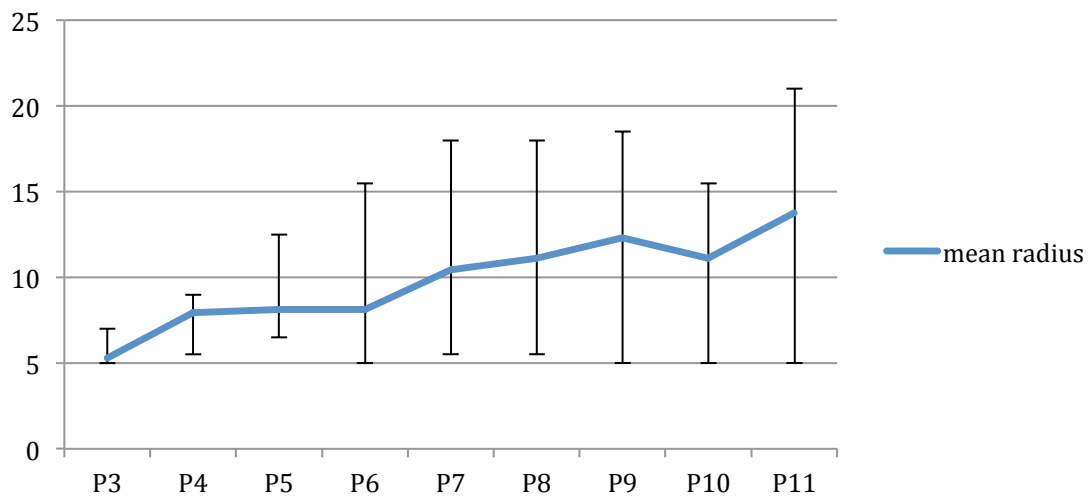


Figure 6.3-6 Mean radius depicting the smallest and largest dispersoid radius [7050]

6.3.3. Non-dispersoid phases

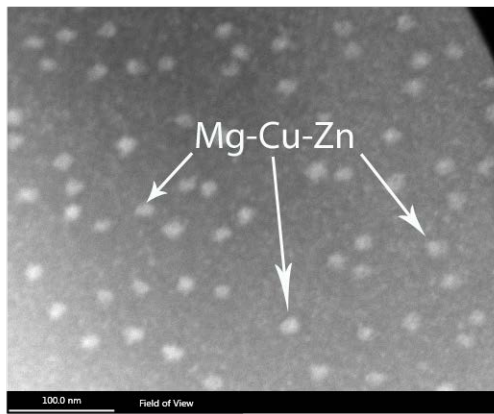
The Mg-Cu-Zn phase encountered in the as-cast structure seems to gradually dissolve into the matrix until no more Mg-Cu-Zn phase can be found in P3. Before it completely dissolves, a spheroidization, as seen in Figure 6.3.3-1 (a), can be observed. At P8 a different Mg-Cu-Zn phase was encountered, very large in size and with a distinct chemical composition (see Figure 6.3.3-2 (b)). This phase was referred to as Mg-Cu-Zn 2. As mentioned above, the Mg-Cu-Zn phase encountered on GB at temperatures above 460°C (P4-P7 and P10-P11) was discarded and assumed to be there due to an insufficient cooling rate.

A few Mg-Cu particles were still found in P3. At P4 temperature reaches a level of around 480°C and no more Mg-Cu phase can be found. Unlike Mg-Cu-Zn, which already precipitates back at P8, the Mg-Cu phase reappears at P9 (Figure 6.3.3-1 (b)).

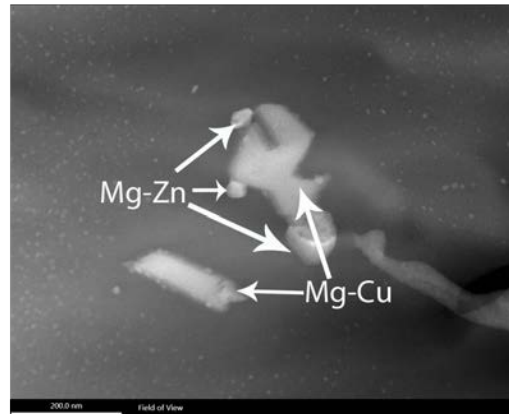
Fe-containing particles were observed in P2 for the first time and can be found throughout the homogenization process and beyond. They appear in different chemical compositions and shapes, see Figure 6.3.3-1 (c).

A few Mg-Si particles were encountered but as they appear to be very rare and difficult to spot, due to their dark appearance, it is possible that some of them were overlooked. Even at temperatures around 480°C a large Mg-Si particle was detected (Figure 6.3.3-1 (d)).

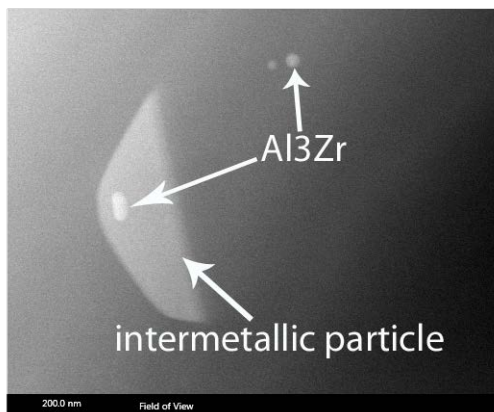
Apart from aforementioned phases a Ti-Cr and a Cu-O phase was detected. Each of them only appeared once in all of the samples, thus they were discarded.



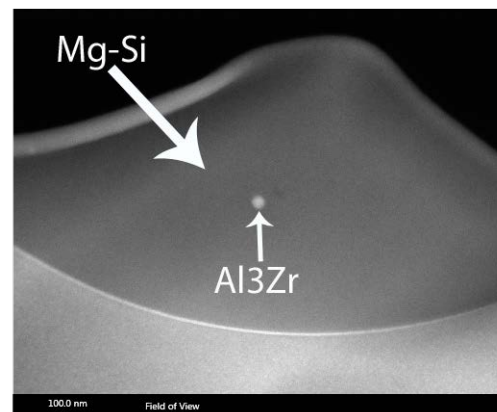
(a) Sample 2



(b) Sample 9



(c) Sample 5

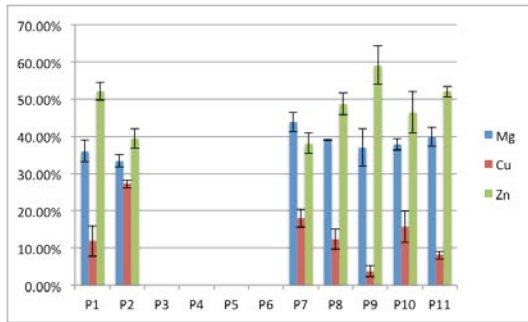


(d) Sample 5

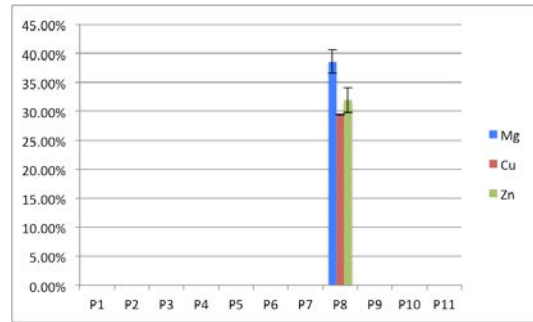
Figure 6.3-7 TEM/STEM images of other phases [7050]

Table 6.3.3-1 Encountered phases [7050]

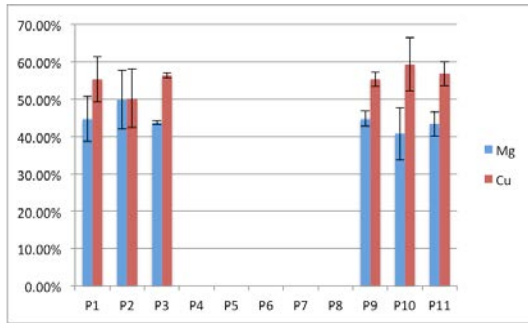
Encountered Phases	<i>Probe #</i>										
	1	2	3	4	5	6	7	8	9	10	11
Mg-Cu-Zn	X	X						X	X		
Mg-Cu	X	X	X						X	X	X
Mg-Si	X				X						X
Fe-Cu		X			X		X	X	X		
Fe-Cu 2		X	X								
Ti-Cr											X
Cu-O		X									
Fe-Mn-Si			X								
Zr			X	X	X	X	X	X	X	X	X



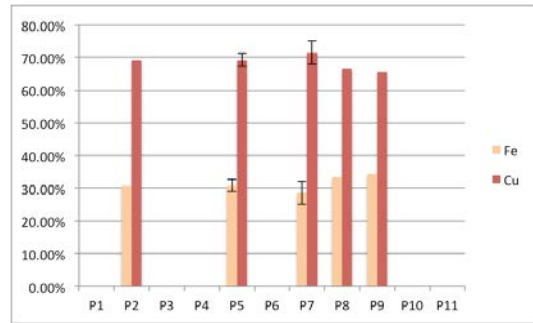
(a) Mg-Cu-Zn [atomic %]



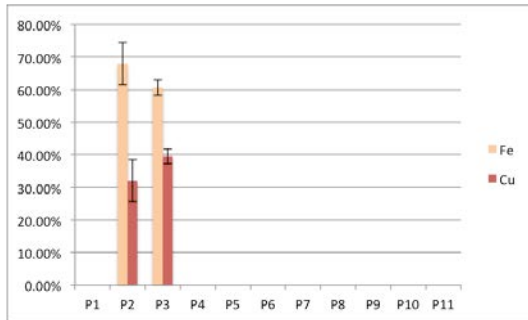
(b) Mg-Cu-Zn 2 [atomic %]



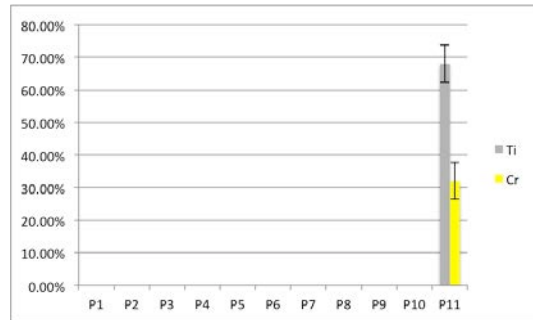
(c) Mg-Cu [atomic %]



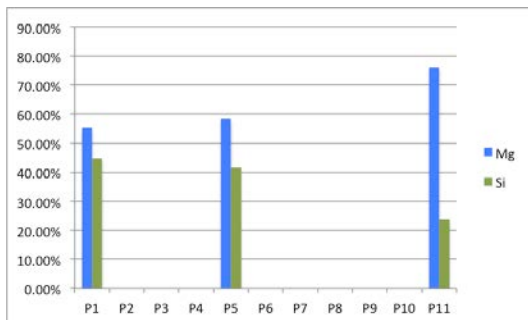
(d) Fe-Cu [atomic %]



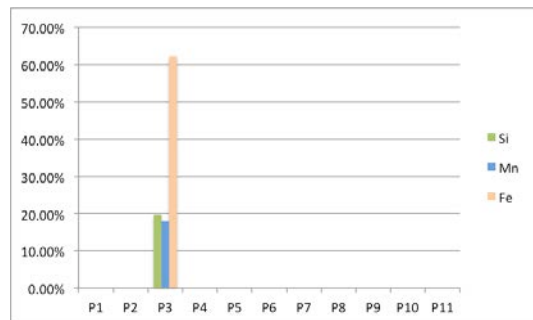
(e) Fe-Cu 2 [atomic %]



(f) Ti-Cr [atomic %]



(g) Mg-Si [atomic %]



(h) Fe-Mn-Si [atomic %]

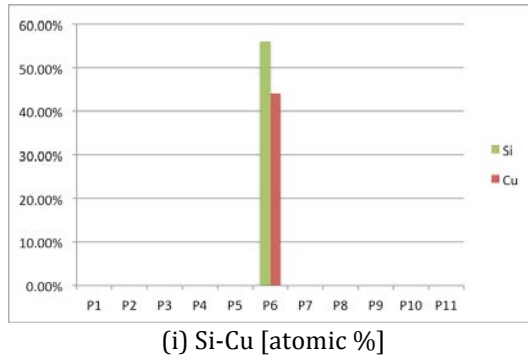
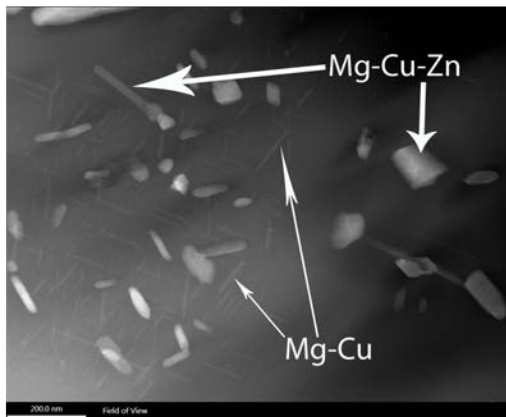


Figure 6.3-8 Chemical composition of the encountered phases [7050]

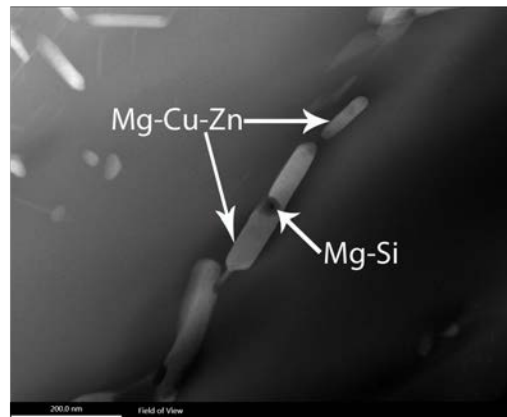
6.4. TITANAL

6.4.1. As-cast structure

The same as-cast phases, which were found in the 7475 and the 7050 alloy, can be detected in the as-cast structure of the TITANAL alloy. Thin and needle-shaped Mg-Cu is surrounded by a Mg-Cu-Zn phase in all sizes and shapes, depicted in Figure 6.4.1-1 (a). The eutectic structure covers most of the GB's. Small particles of the Mg-Si phase were detected on grain boundaries, always in combination with the Mg-Cu-Zn phase as seen on Figure 6.4.1-1 (b).



(a) Sample 1



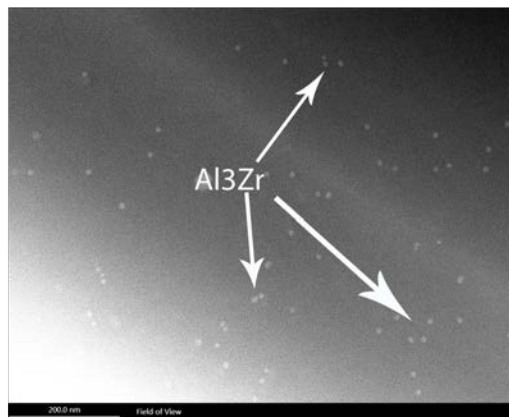
(b) Sample 1

Figure 6.4-1 As-cast structure [TITANAL]

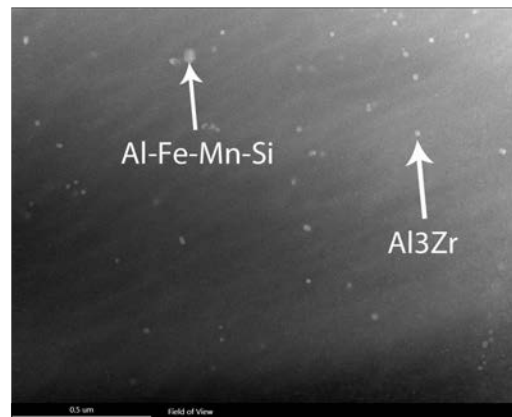
6.4.2. Dispersoids

TITANAL features the same Zr-containing dispersoid as the 7020 and the 7050 alloy. The first dispersoid was detected in P3 at a temperature level above 440°C. We find that the dispersion is already very homogeneously and plenty of dispersoids can be found within the grain (Figure 6.4.2-1 (a)). In comparison to the 7050 alloy, we find that at similar temperature levels and homogenization times, the TITANALA alloy shows far more homogeneously distributed dispersoids (Figure 6.3.2-1(a) and Figure 6.4.2-1 (a)). It should be mentioned that TITANAL has a higher level of Zr and a lower heating rate than the 7050 alloy. The homogeneous distribution stayed constant throughout the homogenization process, see Figure 6.4.2-1 (b).

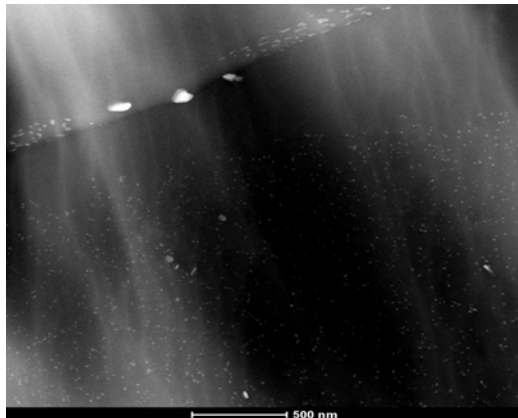
A clear PFZ was visible for samples at elevated temperatures, but this PFZ varied strongly in size as can be seen in Figure 6.4.2-1 (c) and (d).



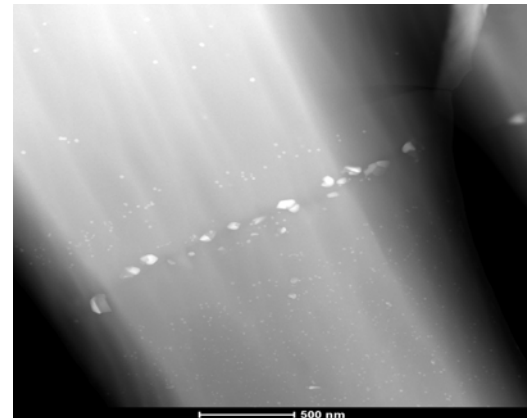
(a) Sample 3



(b) Sample 6



(c) Sample 5



(d) Sample 5

Figure 6.4-2 Dispersoid images [TITANAL]

Figure 6.4.2-2 depicts the ND evolution. There an increase from P3 to P4 can be observed while at the same time the mean radius increases. Those findings are contrary to the observations made with the 7050 alloy (P9-P10), where an increase in ND is always accompanied by a decrease in the mean radius.

The mean radius increases over time and more than doubles during the time period from P3-P6. At P7 a slight decrease can be observed which is in accordance to the findings in 7020, which too shows a decrease in the mean radius for samples at lower temperature levels.

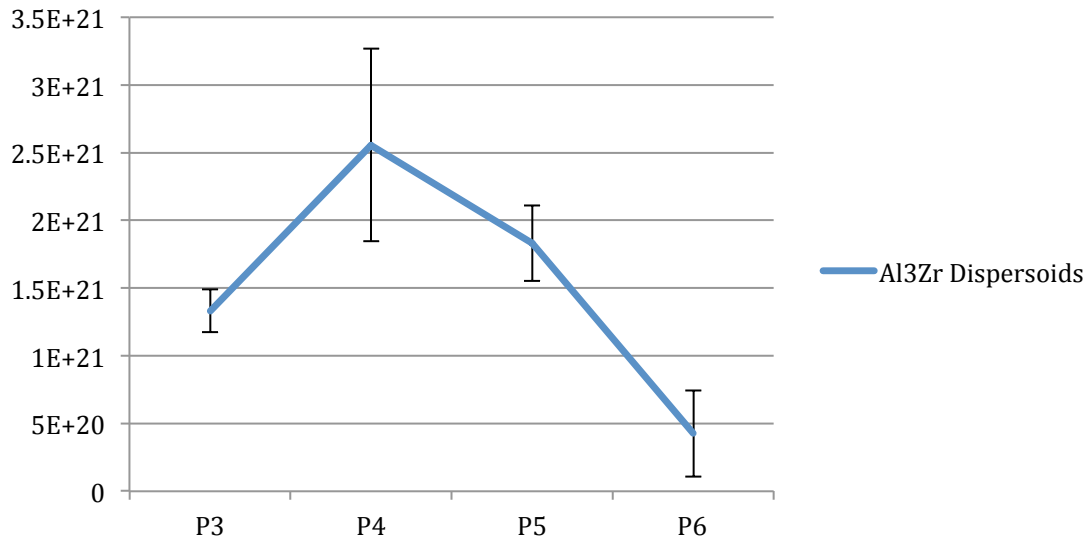


Figure 6.4-3 Number density (dispersoids per m3) [TITANAL]

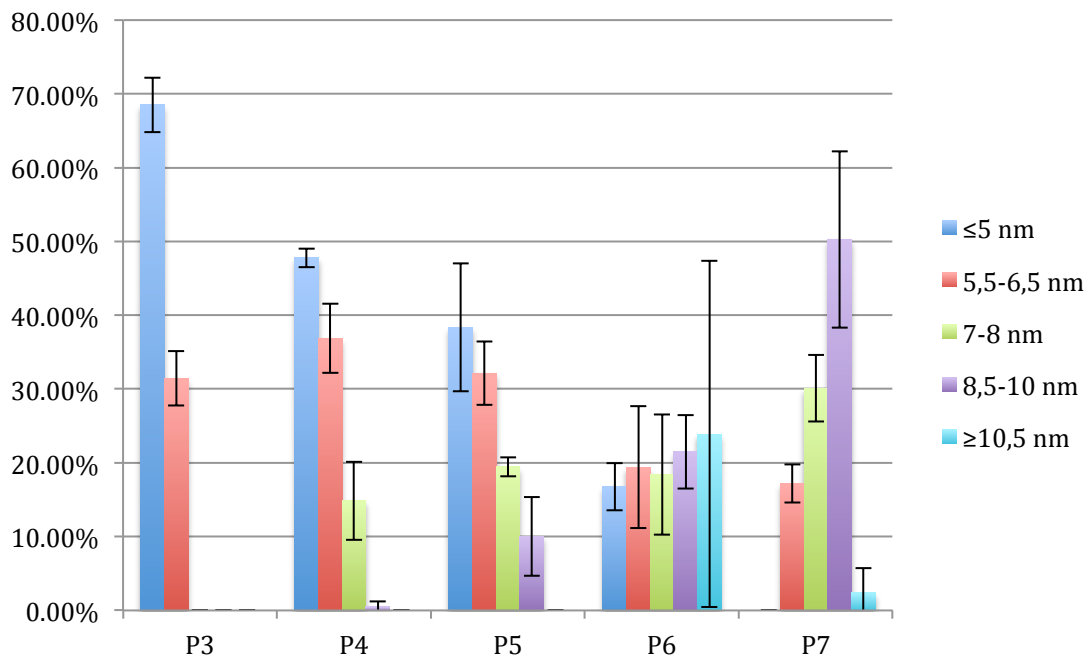


Figure 6.4-4 Dispersoid radius [TITANAL]

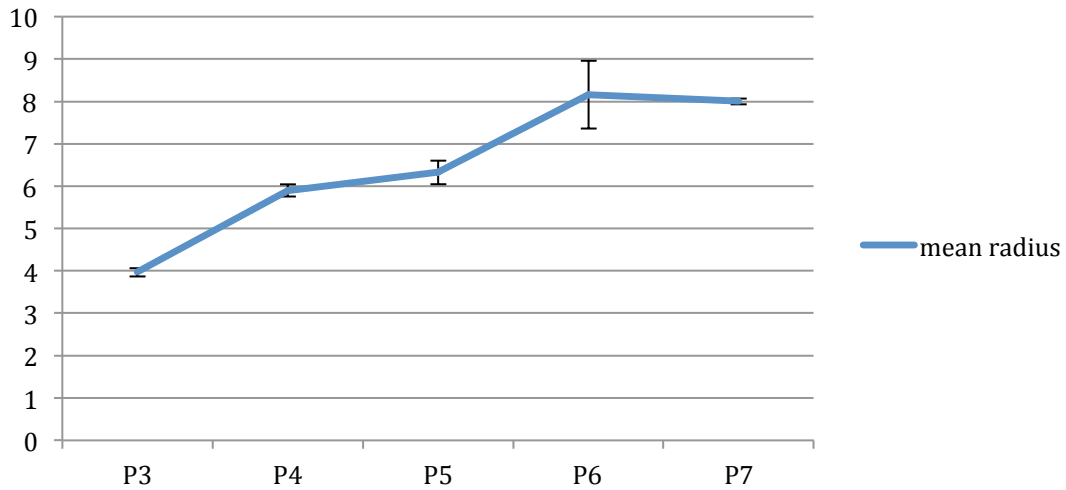


Figure 6.4-5 Mean dispersoid radius [TITANAL]

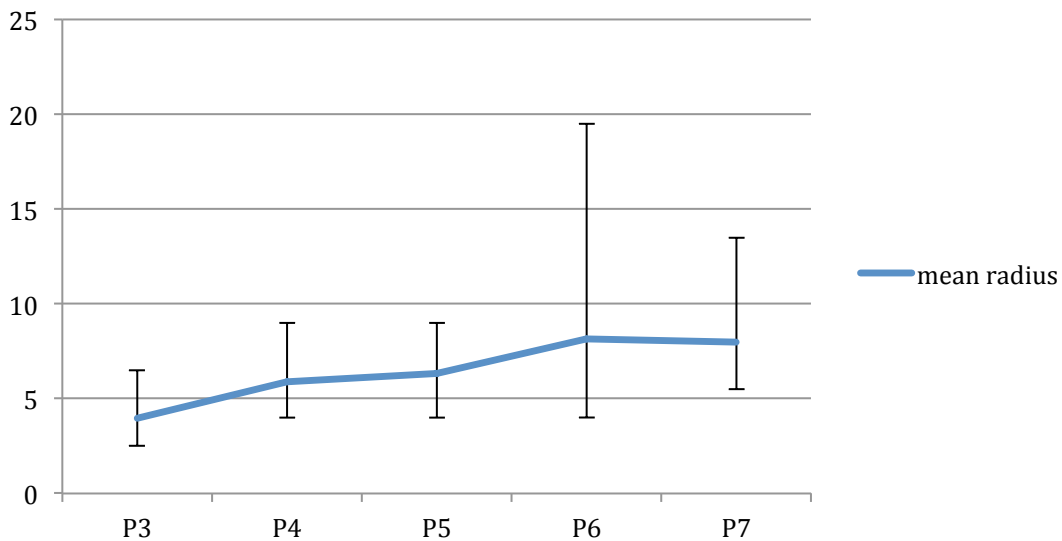


Figure 6.4-6 Mean radius depicting the smallest and largest dispersoid radius [TITANAL]

6.4.3. Non-dispersoid phases

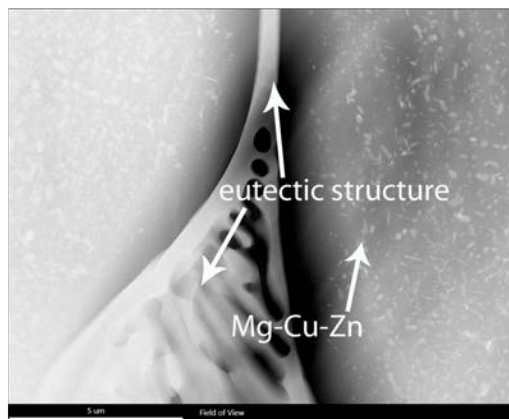
As already observed in the 7050 alloy the eutectic phase starts to gradually dissolve at temperatures above 350°C (Figure 6.4.3-1 (a)). The Mg-Cu-Zn phase is still present in P2 but as a temperature of 440°C is exceeded, this phase dissolve completely. At P6, with a temperature level of around 400°C, very coarse Mg-Cu-Zn particles with a high amount of Cu (Figure 6.4.3-1 (b)) reappear in the matrix. Some of the Al-Fe-Mn-Si-Cr particles found at elevated temperatures show caps of Mg-Cu-Zn, most probably due to an insufficient cooling rate.

Mg-Cu was no longer found in P2 and did not reappear throughout the homogenization process.

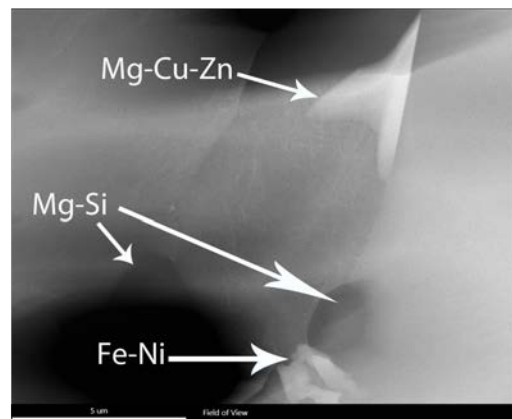
The Mg-Si phase was encountered in samples P2, P3 and P6, all at temperature levels below 480°C.

Intermetallic particles like the Al-Fe-Mn-Si phase were detected at elevated temperatures above 420°C. In many of the samples large Fe-Ni particles were encountered, which is surprising as Ni is regarded as contamination.

3 samples showed Ti-Cr dispersoids, often accompanied by contamination. Furthermore some Si-O phase was detected in P3 on different areas and in P2 a very large Fe-rich particle with large amounts of contamination was found within the grain.



(a) Sample 2

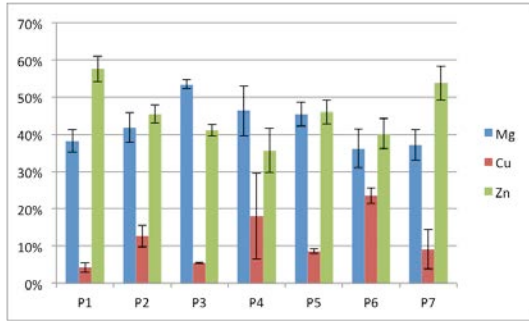


(b) Sample 6

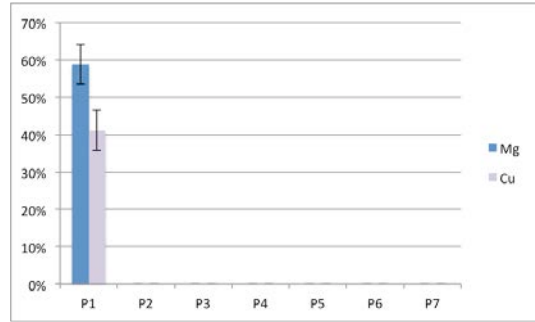
Figure 6.4-7 TEM/STEM images of other phases

Table 6.4.3-1 Encountered phases [TITANAL]

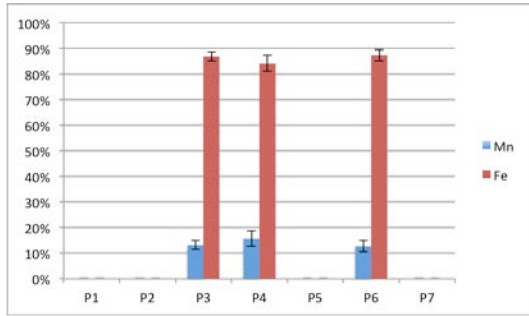
Encountered Phases	<i>Probe #</i>						
	1	2	3	4	5	6	7
Mg-Cu-Zn	X	X				X	X
Mg-Cu	X						
Mg-Si	X	X				X	
Fe-Mn			X	X		X	
Fe-Mn-Si			X	X		X	
Fe-Ni				X	X	X	
Ti-Cr				X	X		X
O-Si			X				
Zr			X	X	X	X	X



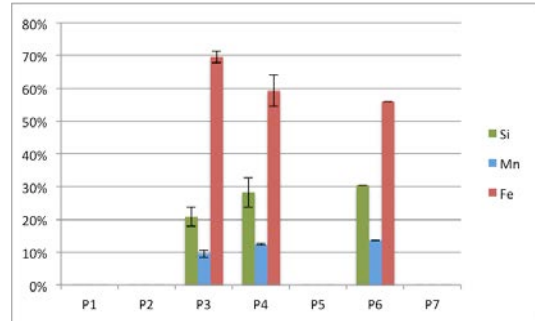
(a) Mg-Cu-Zn [atomic %]



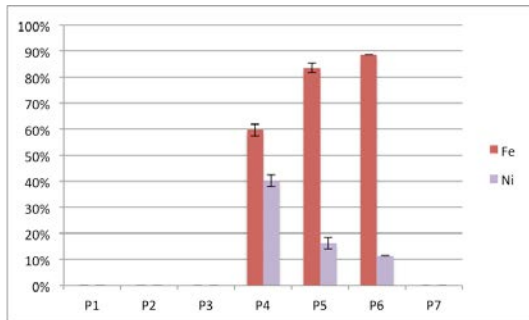
(b) Mg-Cu [atomic %]



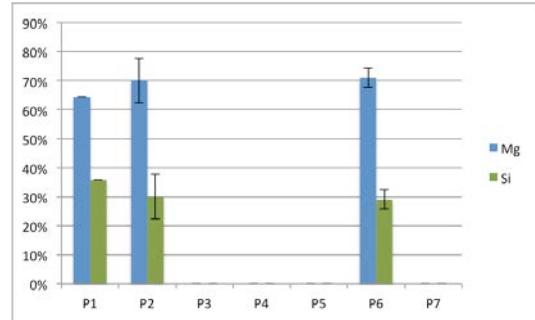
(c) Fe-Mn [atomic %]



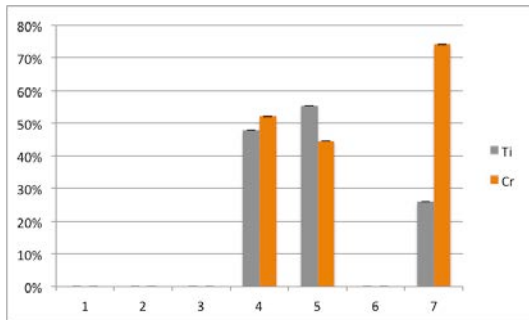
(d) Fe-Mn-Si [atomic %]



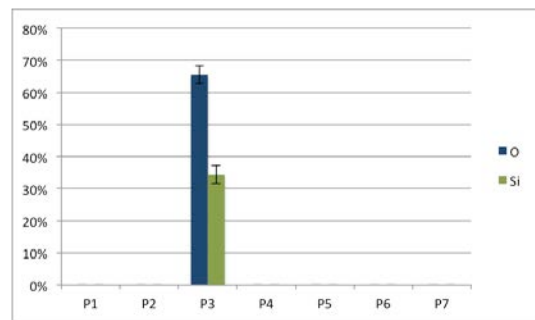
(e) Fe-Ni [atomic %]



(f) Mg-Si [atomic %]



(g) Ti-Cr [atomic %]



(h) O-Si [atomic %]

Figure 6.4-8 Chemical composition of obtained phases [TITANAL]

6.5. Annotations:

As the thickness across a region varies considerably, all EELS thickness measurements were taken in the middle of the images to establish a mean thickness with which the ND count was conducted. Furthermore all windows for the ND counts were placed on areas with similar thicknesses to avoid large discrepancies between the regions.

Figures 6.1.2-2, 6.3.2-3 and 6.4.2-3 show the size classes of the counted dispersoids during the ND counts with their respective standard deviation.

Figures 6.1.2-3, 6.3.2-4 and 6.4.3-4 depict the mean radius and standard deviation of the dispersoids, while Figure 6.1.2-4, 6.3.2-5 and 6.4.2-5 show the mean radius with the largest and smallest counted dispersoid.

Tables 6.1.2-1, 6.2.2-1, 6.3.2-1 and 6.4.2-1 lists all encountered phases and the respective samples, in which those phases were encountered.

Figures 6.1.3-2, 6.2.3-3, 6.3.3-3 and 6.4.3-2 depict all encountered phases (including particles found on the GB's) with their chemical composition according to the EDX analysis. If there is no error bar, not more than 1 particle of the indicated phase was found. Some of the particles are located on or beneath other particles, thus we find higher amounts of certain elements in our spectrum as those particles (or the matrix) slightly "falsify" our spectrum (e.g. a large Mg_2Si particle beneath a Mg-Cu-Zn particle will lead to higher peaks of Mg in the EDX spectrum of the Mg-Cu-Zn particle as well as a Si peak).

6.6. Spectra

Figure 6.5-1 to Figure 6.5-11 depicts the spectra of the main second phase particles. The spectra of phases, which were encountered in more than one alloy, are only listed once.

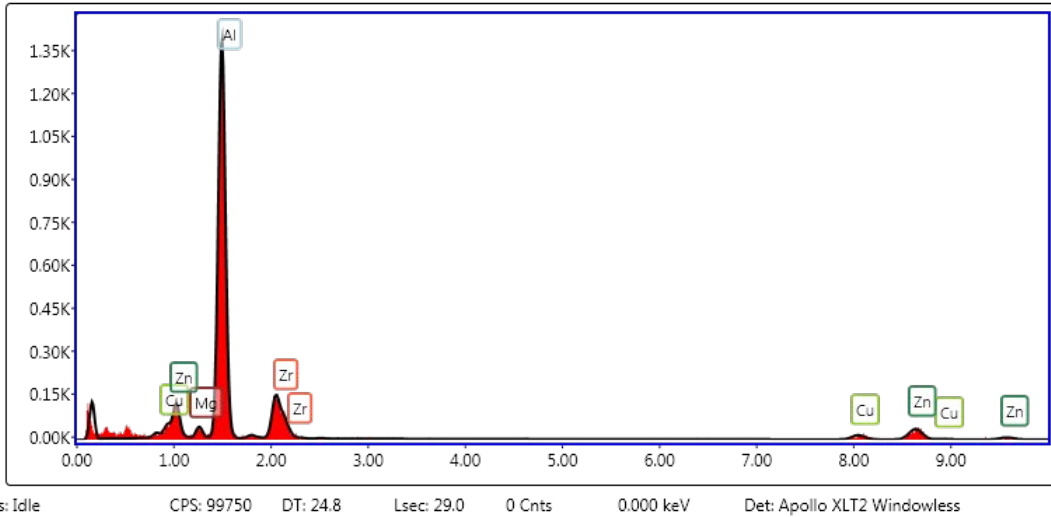


Figure 6.5-6.6-1 Zr-containing dispersoid [7020], [7050], [TITANAL]

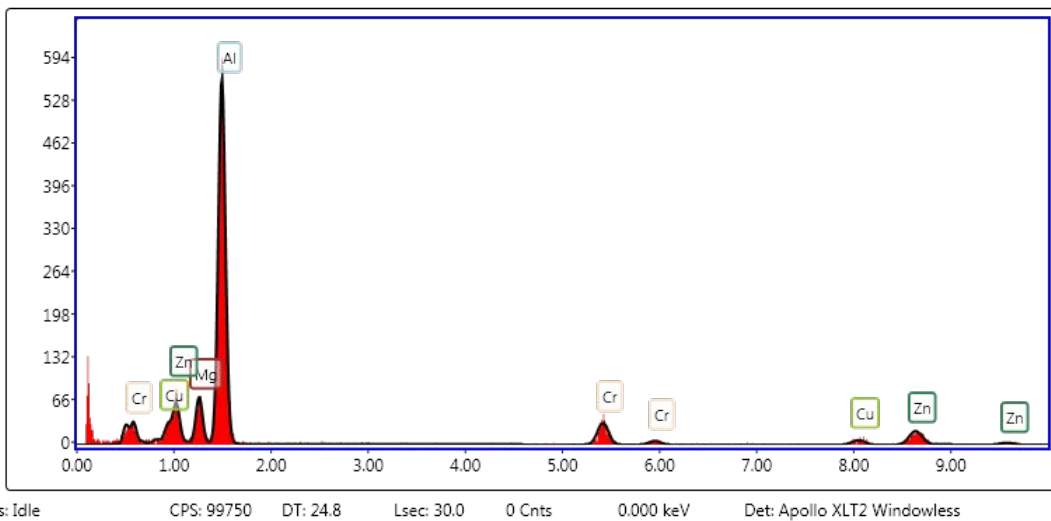
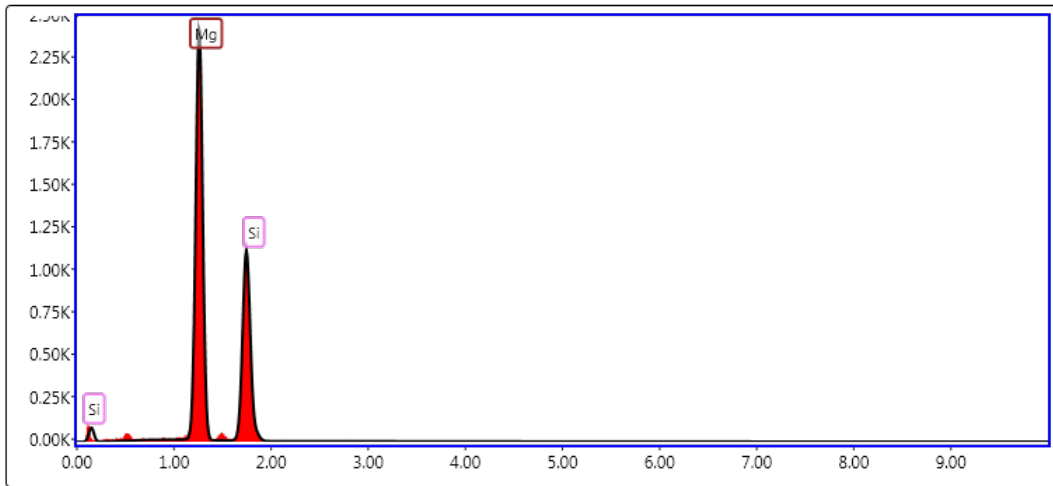
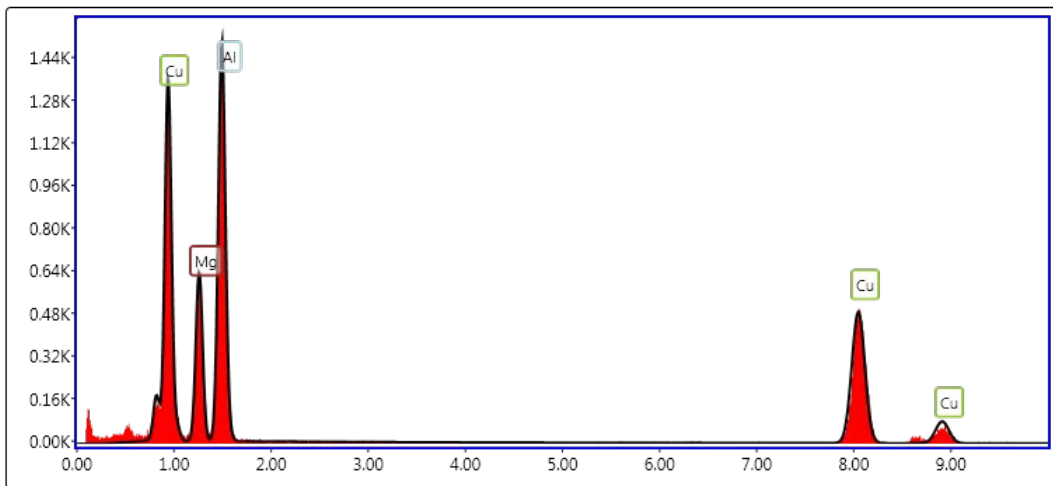


Figure 6.5-6.6-2 Cr-containing dispersoid [7475]



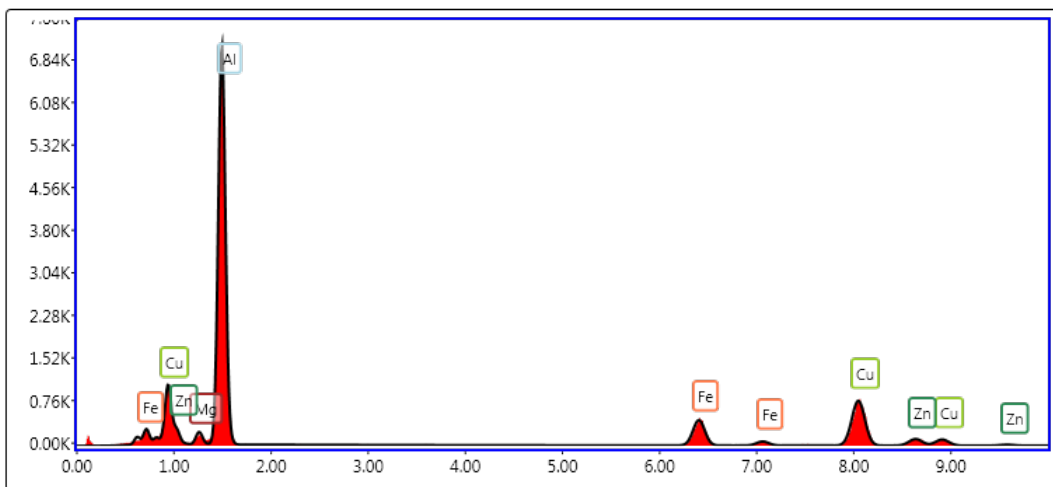
Status: Idle CPS: 99750 DT: 24.8 Lsec: 28.9 0 Cnts 0.000 keV Det: Apollo XLT2 Windowless

Figure 6.5-6.6-3 Mg-Si [7020], [7474], [7050], [TITANAL]



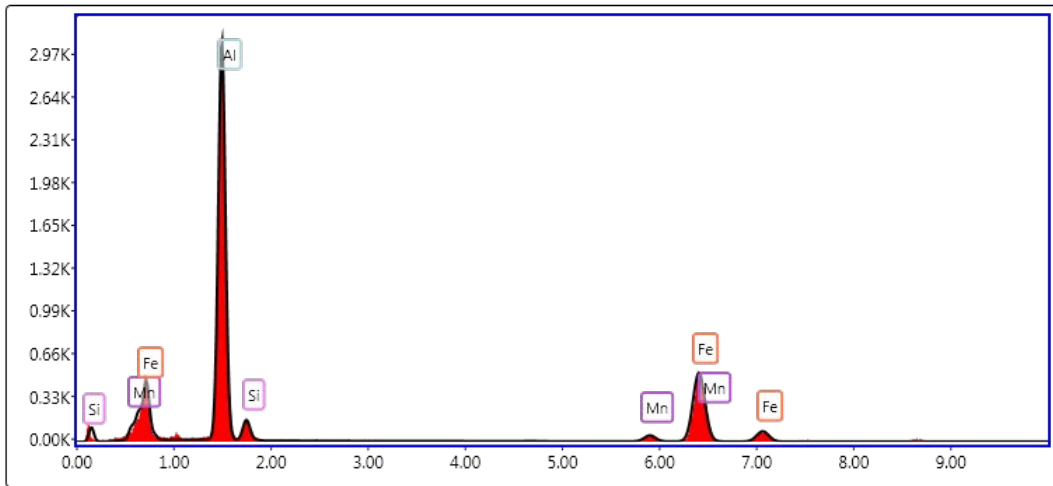
Status: Idle CPS: 99750 DT: 24.8 Lsec: 28.7 0 Cnts 0.000 keV Det: Apollo XLT2 Windowless

Figure 6.5-6.6-4 Mg-Cu [7475], [7050], [TITANAL]



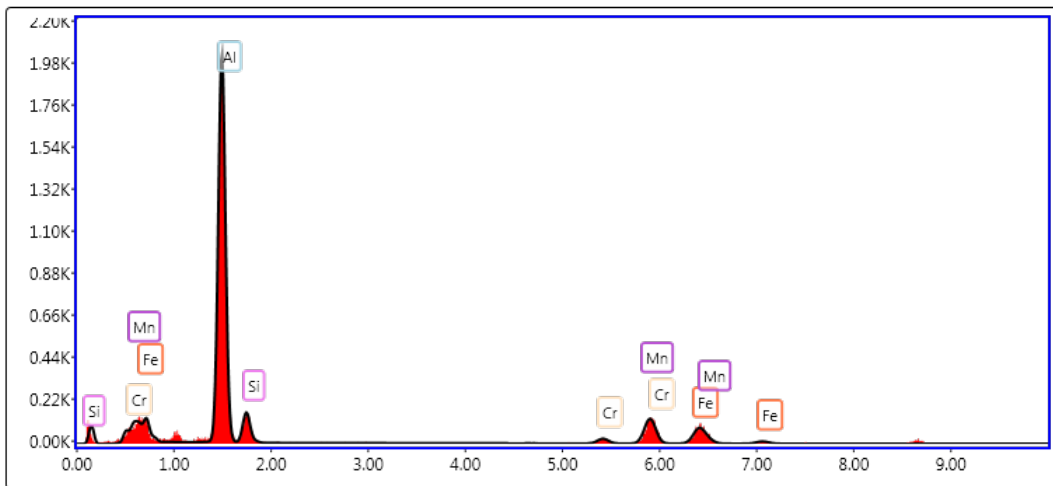
Status: Idle CPS: 99750 DT: 24.8 Lsec: 30.0 0 Cnts 0.000 keV Det: Apollo XLT2 Windowless

Figure 6.5-6.6-5 Fe-Cu [7475], [7050]



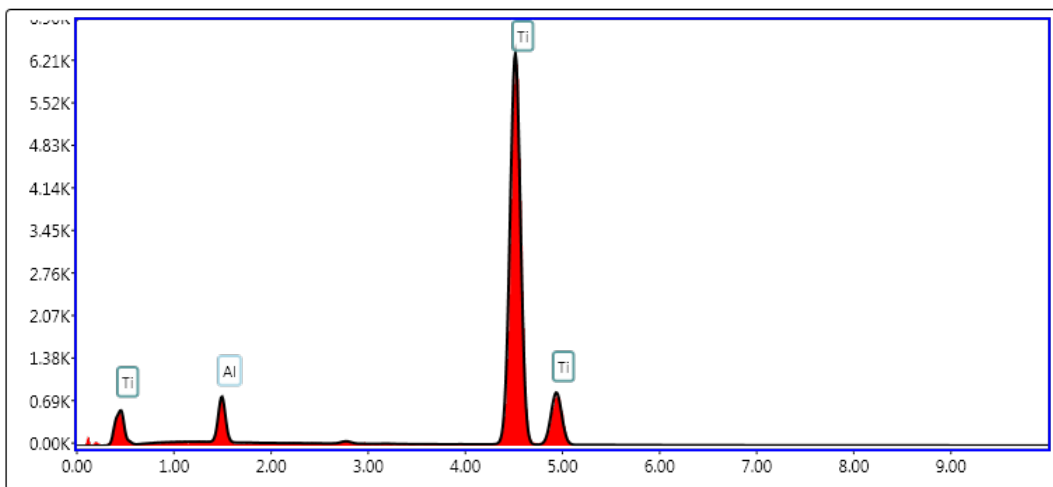
Status: Idle CPS: 99750 DT: 24.8 Lsec: 30.0 0 Cnts 0.000 keV Det: Apollo XLT2 Windowless

Figure 6.5-6.6-6 Fe-Mn-Si [7020], [7475], [7050], [TITANAL]



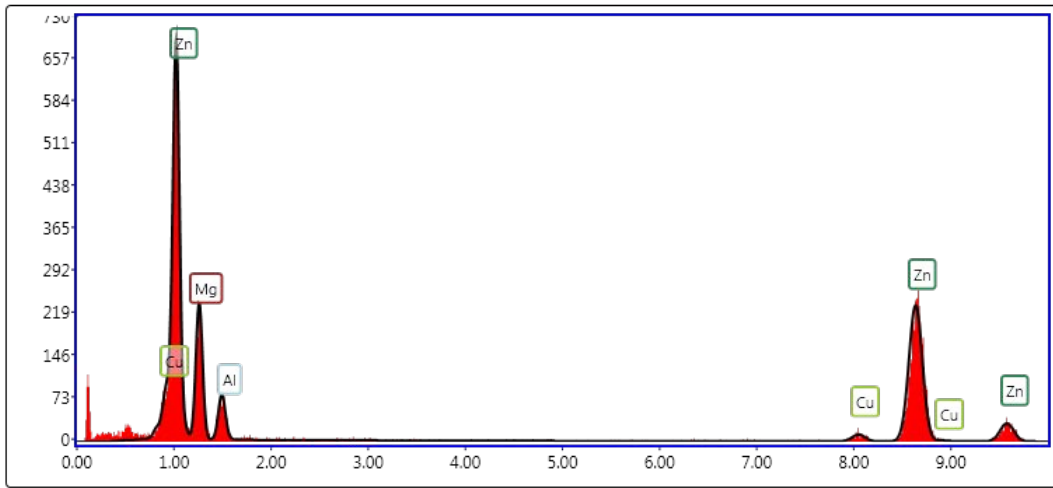
Status: Idle CPS: 99750 DT: 24.8 Lsec: 30.0 0 Cnts 0.000 keV Det: Apollo XLT2 Windowless

Figure 6.5-6.6-7 Fe-Mn-Si-Cr [7020], [7475]



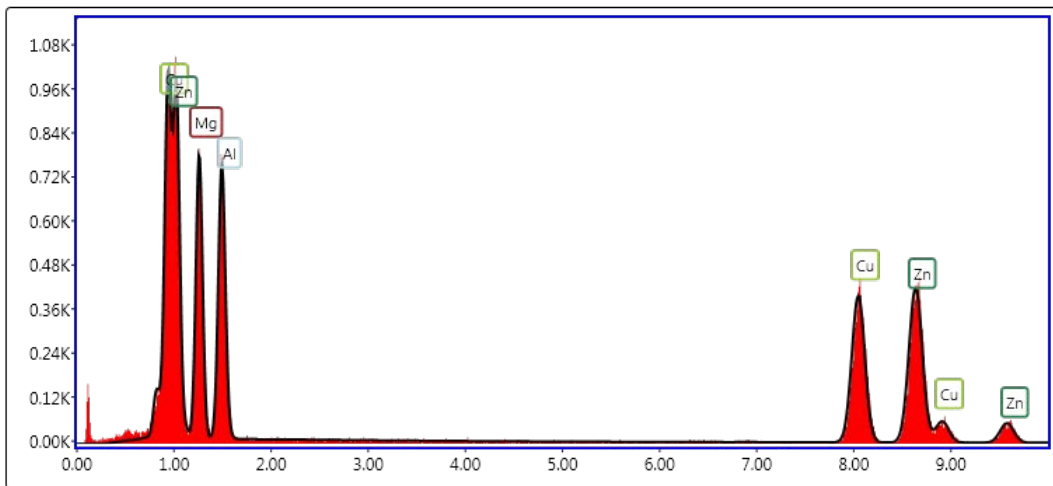
Status: Idle CPS: 99750 DT: 24.8 Lsec: 30.0 0 Cnts 0.000 keV Det: Apollo XLT2 Windowless

Figure 6.5-6.6-8 Ti [7020], [7475]



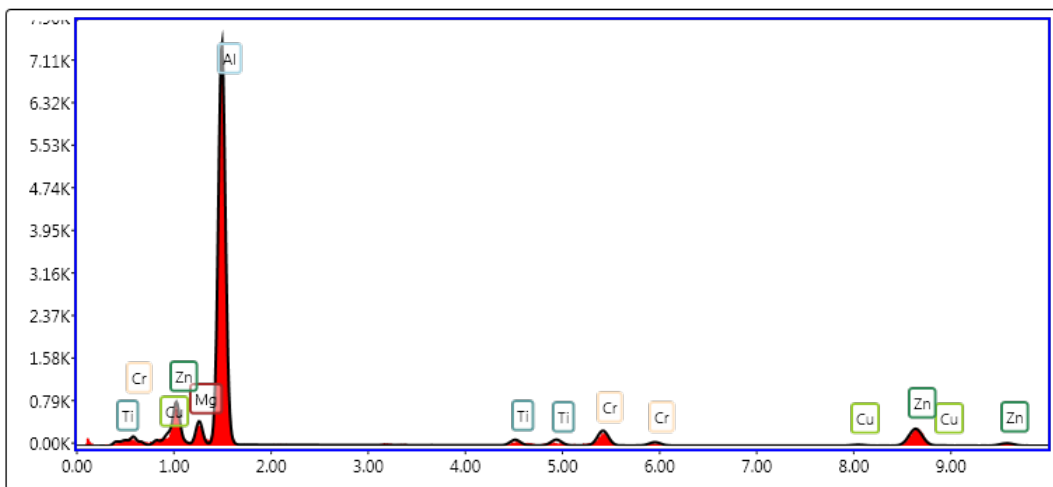
Status: Idle CPS: 99750 DT: 24.8 Lsec: 30.0 0 Cnts 0.000 keV Det: Apollo XLT2 Windowless

Figure 6.5-6.6-9 Mg-Cu-Zn [7020], [7050], [TITANAL]



Status: Idle CPS: 99750 DT: 24.8 Lsec: 30.0 0 Cnts 0.000 keV Det: Apollo XLT2 Windowless

Figure 6.5-6.6-10 Mg-Cu-Zn 2 [7475], [7050]



Status: Idle CPS: 99750 DT: 24.8 Lsec: 30.0 0 Cnts 0.000 keV Det: Apollo XLT2 Windowless

Figure 6.5-6.6-11 Ti-Cr [7020], [7050], [TITANAL]

7. Discussion

7.1. 7020

7.1.1. Non-dispersoid phases

Apart from the Mg-Cu-Zn and the Fe-Mn-Si-Cr phase in P1 all other phase compositions stay almost unchanged irrespective of the holding times and temperatures. The Zn fraction of the Mg-Cu-Zn phase reduces slightly with ascending temperature, as Zn has a higher solubility than Mg and Cu [26]. The large amount of Fe in particles found in P1 is due to the very low solid solubility of Fe in Al, which results in severer microsegregation of Fe toward the grain boundaries, leading to the formation of other intermetallic compounds. According to literature at temperatures below $<470^{\circ}\text{C}$ new precipitates start to form and the volume fraction of particles increases, while at temperatures above $>470^{\circ}\text{C}$ the particles start to dissolve back into the matrix [26]. This is in good accordance with the findings as an increasing amount of particles, homogeneously distributed, from P1 to P2, was observed while, from P2-P4, the volume fraction significantly reduced.

The Mg-Si particles were identified as the Mg_2Si phase, which usually dissolves at temperatures of around 520°C . As P3 reaches a similar temperature level the Mg_2Si phase is not expected. This assumption corresponds well with the encountered Mg-Si particles as they can only be found again in P6 at the end of homogenization [63].

Some works regarding the 7020 alloy found Zr-containing, Cr-containing and Mn-containing dispersoids [26], [64]. While the Zr-containing dispersoids were encountered none of the other types of dispersoids could be detected. Cr-dispersoids are much larger than the Zr-dispersoids and as there is quite a good amount of Cr in the Al-Fe-Mn-Si-Cr particles, there might not be enough Cr left in the matrix to form said dispersoids.

The large Ti and Cr particles are assumed to be primary precipitates due to their size and occurrence (just one of each was found).

7.1.2. Dispersoids, number density and size evolution

The only encountered dispersoid type was a Zr-containing one, which was detected for the first time in P3 and identified as the Al_3Zr phase. But the observed frequency was too low for a number density count. Furthermore there was no sample in which the dispersion was homogeneously enough to conduct a ND count. This is apparent on Figure 6.1.2-1 (b) and (c), showing a high number density of Zr-containing dispersoids and no dispersoids, all within the same sample.

Hence only the size of the Al_3Zr particles was characterized. As the heating rate from P1 to P3 is very fast compared to the other alloys we expect fewer but

larger dispersoids [44]. According to Figure 6.1.3-2 at P4 the mean dispersoid radius is 14,7 nm. From P4 to P5 they continue to increase in size, but as the time difference between these two probes is short in comparison to the other homogenization holding times, the growth is quite low (16,5 nm). A sudden drop in the dispersoid radii can be observed at P6. This might be explained through the precipitation of new and smaller dispersoids, as not all Al_3Zr dispersoids were able to nucleate during the first heating up stage of the homogenization process. 7020 has the highest heating rate and thus not all dispersoids have sufficient time to form large enough clusters, needed for nucleation. As the sample is cooled again from P5 to P6 the nucleation process starts again and small dispersoids can be found reducing the overall mean radius. According to *Robson* a high homogenization temperature and heating rate leads to heterogeneous nucleation and coarse particles as the nucleation rate at temperature levels above 500°C (for 0,09 wt.% Zr) equals almost zero and the growth rate of the dispersoids hits its peak [29]. Heterogeneous nucleation is demonstrated via the nucleation of Al_3Zr on large intermetallic particles, especially during the early stages of the homogenization process (Figure 6.1.2-1 (a)).

7.2. 7475

7.2.1. Non-dispersoid phases

According to Table 4.1.1-1, the Cu level in the 7475 alloy is lower than it is in the 7050 and the TITANAL alloy, but the mean chemical composition of the Mg-Cu-Zn phase contains similar or higher amounts of Cu than in those two alloys. Although they have dissolved within the grain at P2, at P6 the Mg-Cu-Zn phase with a high level of Cu has already precipitated back and is still present in P8 and P9. Cu-rich Mg-Cu-Zn particles appear to be more stable at higher temperatures as they can still be found above 400°C . At RT Mg-Cu-Zn particles with a Cu amount below 10 at. % were encountered quite regularly, while at elevated temperatures only particles with Cu levels around 20 at. % were encountered. This is due to the fact that Cu has a slower diffusion velocity than Mg and Zn [65]. The chemical analysis of the needle-shaped particles in P1 identified them as the S-phase (Al_2CuMg). Literature doesn't state an exact temperature at which the S-phase dissolves, but it is assumed that around 480°C , or 460°C and holding times longer than 12h [65]. This is the case for P2 in which no more S-phase was encountered.

Mg-Cu particles found at P2, P3 and P9 appear to have a very high Cu content and are assumed to be Al_2Cu , which can be found in the as-cast structure and is due to the low Cu diffusion velocity quite stable [56]. The scarce amount of intermetallic phases is due to the very low Fe content (Table.4.1.1-1) [52]. The Mg-Si particles are identified as the Mg_2Si phase and dissolution of Mg_2Si is expected to happen around 520°C , which is in accordance to the findings. The intermetallic phase is not expected to dissolve, not even at very high

temperatures. Those particles can be found throughout the homogenization treatment [30],[65].

7.2.2. Dispersoids, number density and size evolution

Unlike the other alloys under investigation, the 7475 alloys main dispersoid is a Cr-containing one, which was identified as the $\text{Al}_{18}\text{Mg}_3\text{Cr}_2$ phase. The Cr dispersoid was found homogeneously and in a large number from P2 to P9.

From our first ND count up to P6 we find that the ND declines while a surprising ND rise at P7 was encountered. The temperature drop from P6-P7 might be a possible explanation for the unexpected ND increase, as the $\text{Al}_{18}\text{Mg}_3\text{Cr}_2$ nucleation rate seems to be higher at temperatures around 400°C. Similar to the 7020 alloy, the heating rate is quite high and not all Cr-dispersoids have enough time to nucleate. Hence during cooling in which the optimum nucleation temperature is crossed, new dispersoids form and cause an ND increase. The ND continues to rise from P7-P9 and the lower temperature level, as it is the case in P6-P7, could be the reason for this increase. As the ND also increases from P7 to P8, with both of them at the same temperature level, it can be concluded that a temperature of around 420°C seems very suitable for the nucleation of the Cr-dispersoids. This is contradictory to the findings earlier and a look at the error bar shows, that it is possible that the ND stays constant from P8 to P9.

Some Cr-containing dispersoids show traces of Ti, which is due to a substitution process in the $\text{Al}_{18}\text{Mg}_2\text{Cr}_2$ and was also detected by *Ayer et al.*

The Cr-dispersoids show three main shapes, triangular, rod-like, irregular (Figure 6.2.2-1 (a)). According to literature the rod-like shaped dispersoids are most probably triangular shaped ones viewed parallel to the plane of the triangle [52].

Due to the fact that the dispersoids had such different shapes it was not possible to calculate a mean radius or analyse the size evolution. Optical inspection and comparison did not provide any more information, but a coarsening of the dispersoids is assumed due to long homogenization times and high temperatures.

7.3. 7050

7.3.1. Non-dispersoid phases

The Mg-Cu-Zn phase shows a decrease of Zn and an increase of Cu level, compensating for the Zn decrease, with an ascending of temperature. As mentioned earlier this is due to a higher solubility of Zn in Al at higher temperatures and lower Cu solubility [65]. All other phases seem relatively unchanged. The variation of the Mg-Si, which is identified as the Mg_2Si phase, are assumed to be due to more or less matrix measured in the EDX analysis, as the

Mg₂Si phase usually stays constant during the homogenization treatment at temperatures below 500°C [63].

As mentioned earlier, literature states that the S-phase starts to dissolve at temperatures around 480°C, or 460°C with holding times longer than 12h. This, together with the analysis of the chemical composition, led to the conclusion that the Mg-Cu phase will most probably be the S-phase as no more Mg-Cu particles were encountered in P4, which lies above the dissolution temperature of the S-phase. [30], [65]. At P5, P6 and P7 intermetallic phases with different constituent elements like Cu, Mg and Si were found. Those particles tend to be very coarse. Furthermore the Fe-Cu particles had very different compositions. The Fe-Cu phase was identified as the Al₇Cu₂Fe phase, while for Fe-Cu 2 phase no reference in literature was found [66].

According to literature no more Mg-Cu phase at P9 should be found within the grain (can still exist on GB). As a Mg-Cu phase is still present it is assumed that due to a low cooling rate the S-phase precipitated again [66].

7.3.2. Dispersoids, number density and size evolution

All Zr-containing dispersoids were identified as the Al₃Zr phase. The first of these dispersoids was found in P3 and similar to the 7020 alloy it nucleated on an intermetallic particle. A heating rate of more than 0,8°C per minute (P1-P2) seems to stimulate heterogeneous nucleation as the 7020 and 7050 alloy have very similar heating rates up to the temperature level of 400°C. Figure 6.3.2-2 shows that the ND constantly decreases until it reaches a level below 1E+20 dispersoids per m³ at P9. P6 and P7 are taken at the highest homogenization temperature level. The diffusion rate increases with temperature and the diffusion process accelerates from solute rich to solute poor regions [67]. Ostwald ripening describes the process, which dissolves finer particles and diffuses the solute to the coarser particles increasing the mean size of the dispersoids and decreasing the ND [68]. Due to the high homogenization temperatures a significant drop in the ND is expected as the coarsening rate increases at high temperatures [69]. This is well reflected in Figure 6.3.2-2 as the ND experiences a large decrease between P6 and P7. During the cooling stage from P7 to P9 we would expect the formation of new dispersoids as already observed in the 7020 and the 7475 alloy. For the 7050 alloy this is not the case. A look at the cooling rates shows that from P7 to P8 the alloy experiences a very high cooling rate of around 1,5°C/min while the cooling rate from P8-P9 is only around 0,5°C/min. This indicates that at temperatures above 400°C nucleation of new dispersoids takes place, but is prevented through the high cooling rate.

After the homogenization the alloy is heated again close to the final homogenization temperature, causing an increase in the ND at P10 and P11. This can be explained by the nucleation of dispersoids during the heating up phase from P9 to P10. At slow heating rates, in the case of the 7050 alloy of around 0,7°C/min, plenty of very small dispersoids are formed. But as the temperatures rises and the holding time increases, the coarsening effect takes over and ND reduces [68],[46], [70].

Further analysis of the ND declines from P6-P7, P7-P8, P8-P9 and P10-P11 in regards to temperature and time show a correlation between the reduction in ND's per hour and those two parameters. In Table 7.3.2-1 we see that the ND reduction per hour correlates with the temperature level, as we find that the higher the temperature the larger the factor. This is in good accordance with literature [68], [67],[46].

Table 7.3.2-1 Number density reduction per hour [7050]

Probes	ND reduction per hour
P6 – P7 ^a	2,35
P7 ^a – P8	1,79
P8 – P9	1,08
P10 – P11	1,57

^a All values apart from the ND of P7 are the mean ND's. The new P7 ND = P7 mean ND-St.Dev.*0,667

The mean Al₃Zr radius constantly increases until the end of homogenization up to 12,3 nm. After homogenization the mean dispersoid radius reaches almost 14 nm. Just looking at the homogenization process, the mean particle radius grows around 2,3 times in size from P3 to P9 and a total of 2,6 times from P3 to P9.

Similar to the nucleation of dispersoids the growth and coarsening process strongly depends on time and temperature. *Guo et al* looked at the Al₃Zr at different homogenization temperatures and holding times, achieving a coarsening effect of around 0,52 nm per hour (radius) at 500°C (0,3125 nm per hour at 470°C). His smallest dispersoid has a radius of 20 nm (largest dispersoid radius: 40 nm) [44]. This is much higher than our growth rate of 0,1275 nm per hour and our mean radius of around 12 nm (P9). A possible explanation could be the that *Guo et al* used pure Al, while our alloy included Zn, Cu and Mg, which decreases the Zr solubility when added to Al [71].

According to the Orowan strengthening mechanism, the volume fraction plays a critical role. The higher the volume fraction and the smaller the mean size, the larger the strengthening effect [72]. As Al₃Zr has a spherical shape the volume fraction can be calculated with the number density and mean size of the particles [73]. It was found that the highest volume fraction (0,13%) during homogenization is reached at P6 and P11 (0,17%) shows the highest volume fraction out of all 11 samples. During the dispersoid growth the volume fraction should increase and during coarsening the volume fraction should stay the same. Samples P3 to P5 show a growing mean radius indicating that the dispersoids are in the growth phase. From P6-P7 only a slight reduction in volume fraction can be observed leading to the conclusion that the dispersoids are in the coarsening phase. But as we can see, the volume fraction reduces constantly at elevated temperatures during homogenization from P7 to P9, meaning that a precipitate reversion is taking place [29]. Table 7.3.2-2 shows that in sample P10 and P11 the volume fraction suddenly significantly increases. Taking the growing mean radius into account, the dispersoids are now assumed to be in the nucleation and growth stages. This leads to the conclusion that temperatures of around 460°C are very favourable for the dispersoid development. This assumption is confirmed by *Robson*, which states a maximum homogenization temperature for a Zr concentration of 0,09 wt. % at 450°C [29].

Table 7.3.2-2 Volume fraction [7050]

Probe	Volume fraction (in %)
P6	0,13 %
P7	0,12 %
P8	0,10 %
P9	0,05 %
P10	0,14 %
P11	0,17 %

7.4. Titanal

As TITANAL is a specially made alloy by the *AMAG*, no corresponding literature could be found. Thus the alloy was compared to other alloys with similar levels of Zn and a similar Zn/Mg ratio. Out of our 3 other alloys 7050 has the most similarities, but differs in the amount of Cu.

7.4.1. Non-dispersoid phases

The Mg-Cu-Zn and the Mg-Cu phase can be found, similar to the findings in the 7050-alloy, in ample amounts (Figure 6.4.1-1 (a)). A look at the changes in the chemical composition shows that the Zn content in the Mg-Cu-Zn phase reduces much slower than in the 7050 alloy. This might be due to a slower heating rate, lower maximum homogenization temperature and shorter holding time at those temperatures, as those factors strongly influence the dissolution rate [30]. With a lower maximum homogenization temperature some Mg-Cu, which was identified as the S-phase, would still be expected to exist in the matrix, but this phase was not detected and seemed to have dissolved faster than assumed. After the homogenization treatment we still find no Mg-Cu phase, which might be due to the fast cooling rate (0,95°C/min). 7050 has a lower cooling rate (0,60°C/min, P7-P9) and there the Mg-Cu phase can be found again after cooling [66].

The intermetallic phases were encountered in samples P3-P6 (Table 6.4.3-1) and seem to change little in chemical composition. The same applies for the Mg₂Si phase which can already be found in P1 and due to the low homogenization temperature will not dissolve into the matrix [63],[65].

The few Ti-Cr containing particles were detected on GB's or larger Mg-Cu-Zn particles in P4, P5 and P6.

7.4.2. Dispersoids, number density and size evolution

The Zr-containing dispersoid, identified as the Al₃Zr phase, precipitated homogeneously within the grains from P3 until the end of homogenization at P7.

No ND count was preformed for P7 as too many other phases populated the matrix.

Although the homogenization time at P3 is below 15 hours a ND of more than $1E+21$ dispersoids per m^3 can be found. This is an indicator that a lower heating rate and/or lower maximum homogenization temperature increases the nucleation rate of Al_3Zr dispersoids significantly.

Figure 6.4.2-2 shows a significant further increase of the ND from P3 to P4. A possible explanation might be, that at lower temperatures ($<480^\circ C$) the Al_3Zr phase continues to nucleate as the temperature level favours the nucleation process and the dispersoids are thus finer in size and more homogeneously distributed [27], [68].

During the early stages of the homogenization process (P3-P4), dispersoids are in the growth phase as the ND and the mean radius increases. From P4 to P6 a continuous decline of the ND can be observed. As previously discussed, the Al_3Zr ND decreases in respect to high homogenization temperatures and long holding times. During P4-P5 the volume fraction reduced only by a little, leading to the conclusion that the alloy is now in the coarsening phase. From P5 to P6 a significant drop in volume fraction can be observed. This behaviour is very similar to the one seen in the 7050 alloy where the largest volume fraction drop also took place in the last sample before end of homogenization. In the 7050 as well as in the TITANAL alloy the volume fraction dropped by 50%.

Regarding the mean radius of the dispersoids, we see a constant increase from P3-P6 (Figure 6.4.3-3). Compared to the 7050-alloy they appear to be smaller in size. If we compare the two alloys at temperatures above $400^\circ C$ we find that the dispersoids in the TITANAL-alloy coarsen faster than in the 7050-alloy (Table 7.4.2-1).

Table 7.4.2-1 Coarsening rate

Alloy	Growth rate [nm/h]
7050 (P3-P7)	0,12
TITANAL (P3-P5)	0,15

The volume fraction percentage shows a peak at P4, with 0,22 %, which is the highest measured value out of all four alloys. This might be due to the slow heating rate with $0,5^\circ C/min$ (P1-P3) and a high Zr level, causing the nucleation of an ample amount of very small dispersoids [46].

According to *Robson* the maximum nucleation rate for a Zr concentration of 0,13 wt. % is at $475^\circ C$ [29]. The TITANAL alloy, with a Zr concentration close to 13 wt. %, shows a homogenization temperature (P3-P5) close to the postulated ideal one. This might be another reason for the very homogeneous distribution of the dispersoids.

Table 7.4.2-2 Volume fraction [TITANAL]

Probe	Volume fraction (in %)
P3	0,03 %
P4	0,22 %
P5	0,19 %
P6	0,10 %

8. Simulation vs laboratory investigation

In this chapter the results gained through laboratory investigation are compared to the outcome of the *MatCalc* calculations in order to verify the credibility of the simulation.

Unlike the simulation, which takes all dispersoids irrespective of their size into account, the laboratory investigation can only include dispersoids visible in TEM and STEM images. The smallest counted dispersoid had a radius of 3,5 nm and represents the lower threshold. Any particles below this size are not represented in the experimental ND's. Thus all experimental ND's are expected to be lower than the simulation ones, as the small dispersoids were not included. This also affects the mean radius, leading to a lower mean radius in the simulation. Hence the precise values are not expected to match perfectly, it is rather important that the slopes correlate.

8.1. 7020

In Figure 8.1-1 it can be seen that the predicted mean radius is even higher than found in sample 4 and 5. This is surprising, as due to the many very small dispersoids, the predicted mean radius is usually lower than the mean radius of the counted dispersoids. During the cooling from P5 to P6 new Al_3Zr nucleates with much lower radii, which reduces the mean radius significantly. This is found to be true in the experimental samples and the simulation, represented by a sharp downward bend at P5. Simulation and experimental results seem to correspond in their behaviour throughout the homogenization process, but differ in the inclination, regarding the descending mean radius from P5 to P6.

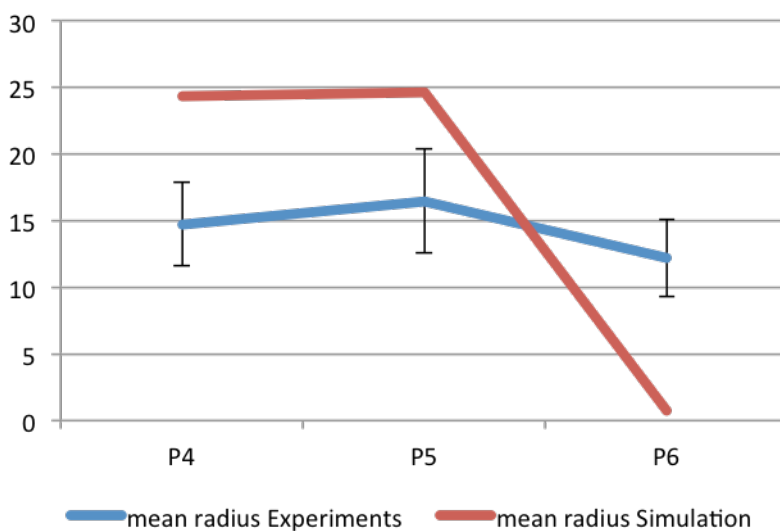


Figure 8.1-1 Mean radius Simulation/Experimental [7020]

8.2. 7475

Comparing the simulation results from P4 to P6 with the laboratory ones, it can be seen that both slopes point downwards and the values are only apart by the factor 10. From P6 to P7 constant ND increase in the experimental results can be observed. This upward trend is followed by the simulation, but in an extreme manner. The ND suddenly increases by the factor 100, all within 13 hours. From P7 to P8 the ND drops to similar levels observed in P6. This behaviour is not reflected in the experimental results. Thus the simulation outcome has to be regarded with great caution and further improvements have to be made.

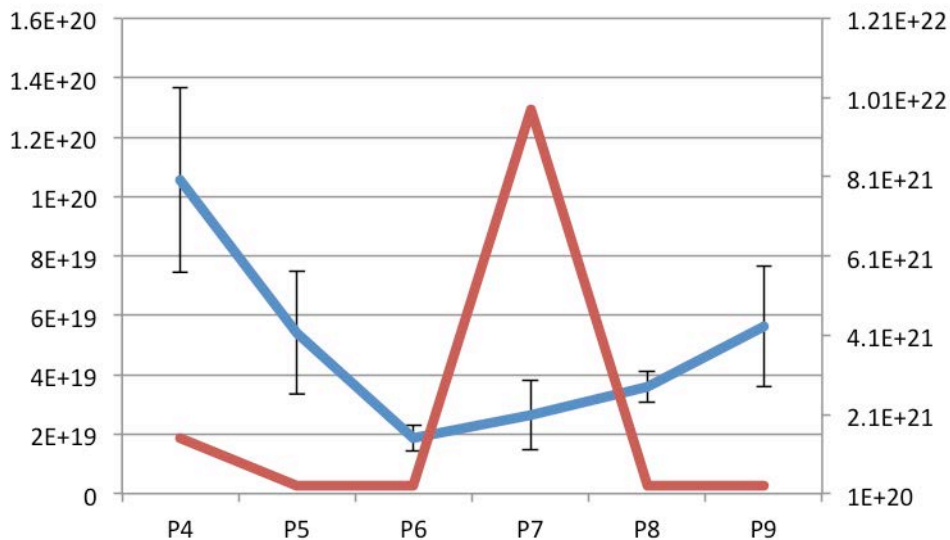


Figure 8.2-1 Mean ND Simulation/Experiment [7050]

8.3. 7050

The simulation indicates that after a significant drop from P6 to P7 the ND should remain at a constant level. Looking at the experimental results, a similar ND drop from P6 to P7 can be observed. From P7 until P8 the ND shows only slight fluctuations, and is basically moving sideways.

Although the results don't match each other perfectly the general trend is verified. Taking the standard deviation into account, the steepness of the drop from P6 to P7 could increase significantly. The sideways movement would also be affirmed, reflecting the simulated behaviour much better.

Figure 8.3-2 depicts the dispersoid evolution. The trend of a constant dispersoid growth is confirmed and growth leaps match each other as seen at the increase from P6-P7. At P5 and P11 the results seem to differ, but taking the error bar into account, those results are still within the limits and fit the predicted behaviour.

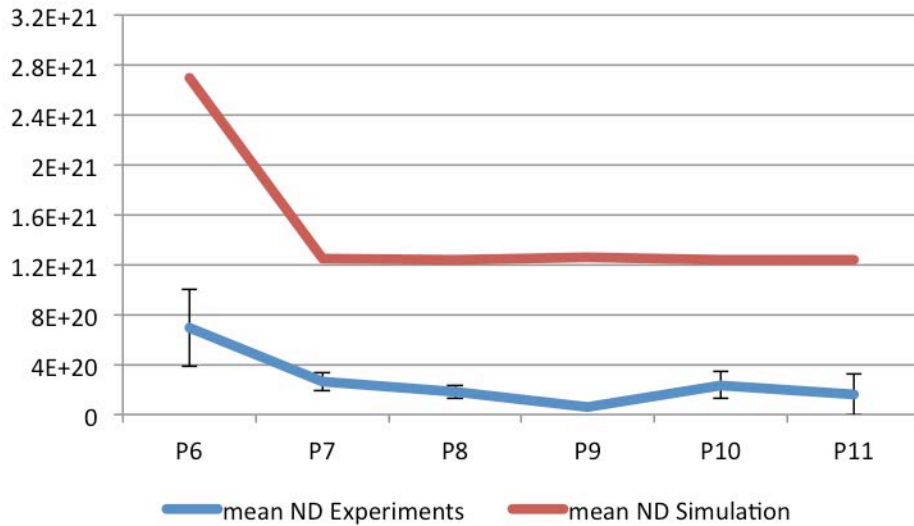


Figure 8.3-1 Mean ND Simulation/Experiment [7050]

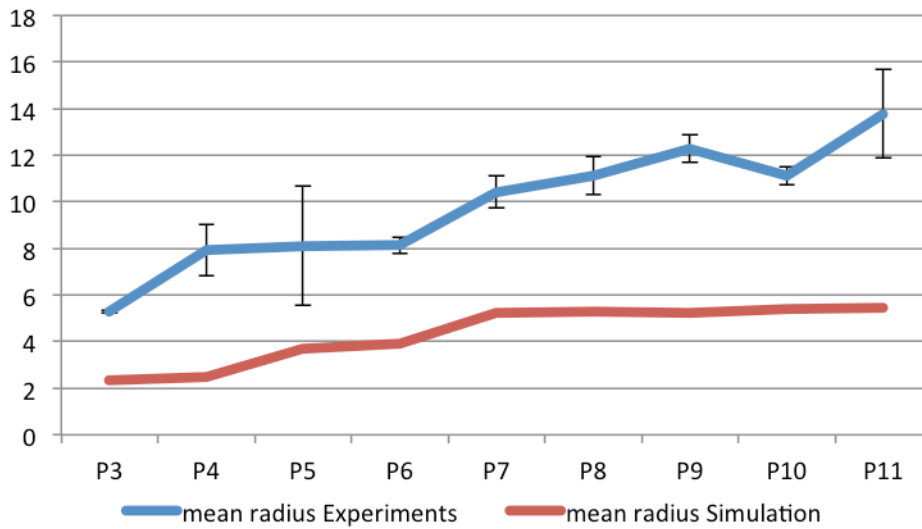


Figure 8.3-2 Mean radius Simulation/Experimental [7050]

8.4. TITANAL

Figure 8.4-1 shows two very different trends. The simulation seems to show a constant reduction in ND, while the experimental results indicate an increase from P3-P4. At first sight this seems to be contradictory, but taking the mean radius into account makes this development more reasonable. As the simulation predicts a mean radius of 1 nm (Figure 8.4-2), most of the dispersoids are out of our visible range, hence the large gap between simulation and experiment. As the radius doubles from P3 to P4, much more dispersoids become visible within our

magnification and can be taken into account. This leads to the large ND increase in the experimental results. As the dispersoids reached a size, which makes them visible in TEM observations, the development of the dispersoids can now be analysed correctly. Both the simulation and the experimental analysis show a constant ND decline from sample 4 to 6. In the simulation P5 and P6 have values of $7,52E+21$ and $7,34 E+21$, which are quite similar to the experimental values. The mean radius of the dispersoids grows constantly, in the simulation as well as in the experimental findings. Simulation results and experimental findings seem to confirm the same trend.

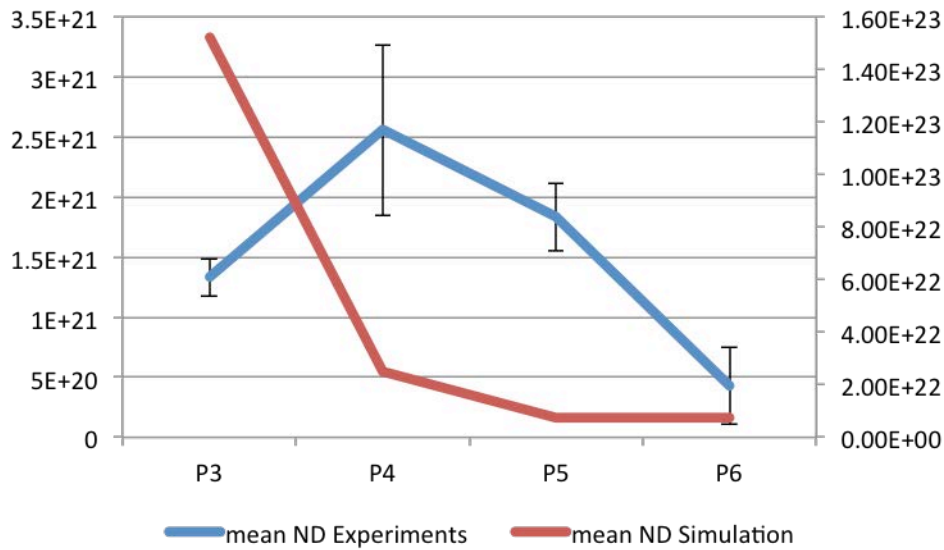


Figure 8.4-1 Mean ND Simulation/Experiment [TITANAL]

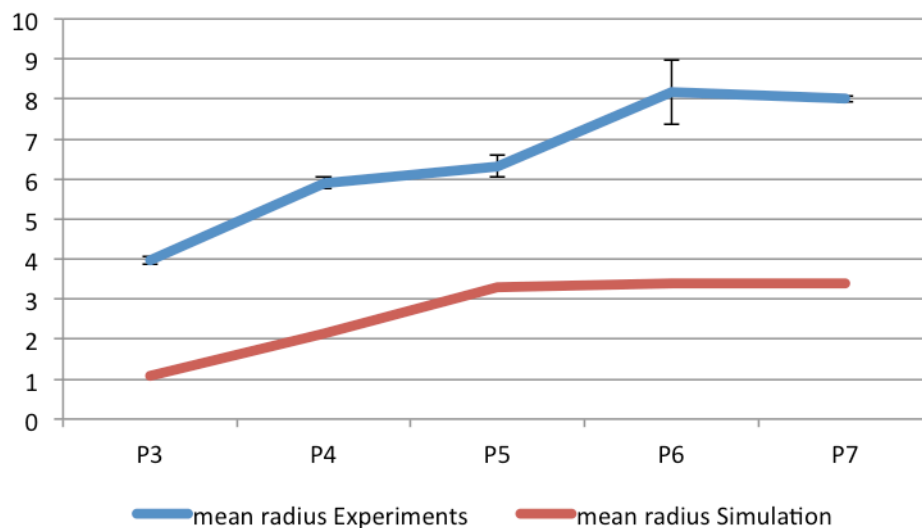


Figure 8.4-2 Mean radius Simulation/Experimental [TITANAL]

9. Summary and Conclusion

In this thesis four different 7xxx alloys were examined. All dominant phases were analysed according to their chemical composition, shape and dissolution temperature. A strong focus was placed on the development of dispersoids in the respective alloys. Dispersoid number densities, mean radii and volume fraction percentages were calculated to gain knowledge about the dispersoid evolution during the homogenization treatments. The investigation was conducted with a TEM/STEM analysis. Via EDX analysis the chemical composition was identified and thickness measurements were made using EELS. The laboratory investigations were accompanied by a *MatCalc* kinetic simulation to review the findings in the specimen.

- a. For all alloys with Al_3Zr dispersoids the heating rate played a crucial role in determining the size and dispersion of the dispersoids. A low heating rate (TITANAL: 0,52 °C/min) leads to very fine and homogeneously distributed dispersoids. While a heating rate of more than 0,83 °C/min, which was applied to the 7020 alloy, led to a heterogeneous distribution and a mean radius of more than 14 nm (TITANAL: 4 nm).
- b. Irrespective of the dispersoid type (Al_3Zr or $\text{Al}_{18}\text{Mg}_3\text{Cr}_2$) the number density significantly reduced at high temperatures with time. At the end of the homogenization process the number density was found to always be significantly lower than the first calculated number density.
- c. Looking at the development of the mean radius and the number density at different temperatures, it was concluded that the highest nucleation rate for Al_3Zr dispersoids is achieved at temperatures between 400-470°C. The ideal temperature also seems to vary with Zr concentration.
- d. The $\text{Al}_{18}\text{Mg}_3\text{Cr}_2$ dispersoid seems to nucleate very homogeneously at temperatures below 400°C, resulting in a number density increase every time this temperature level was crossed.
- e. Simulation results did confirm the general trends regarding number density and mean radius evolution. Although most of the experimental findings are supported by the homogenization simulation further improvements of the simulation and the databases is necessary. Especially regarding the 7475 alloy, simulation results did not match the experimental findings well.

References

- [1] K. Krone, *Aluminiumrecycling: vom Vorstoff bis zur fertigen Legierung*. Aluminium Verlag, 2000.
- [2] A.-Z. Dusseldorf, *Aluminium Taschenbuch. (14. Aufl.) Aluminium-Verlag*. Dusseldorf, 1988.
- [3] W. F. Gale and T. C. Totemeier, *Smithells Metals Reference Book*. Butterworth-Heinemann, 2003.
- [4] I. Balaz, "Europäische Aluminiumwerkstoffe-European Aluminium Materials (Hans-Werner Wenglorz)," *ZVARANIE SVAROVANI*, vol. 56, no. 8, p. 225, 2007.
- [5] F. Ostermann, "Konstruieren mit Aluminium (Einführung)," in *Anwendungstechnologie Aluminium*, Springer Berlin Heidelberg, 2014, pp. 685–721.
- [6] E. DIN, "10025-2: 2005: Warmgewalzte Erzeugnisse aus Baustählen–Teil 2: Technische Lieferbedingungen für unlegierte Baustähle," *Dtsch. Fass. EN*, pp. 10025–2, 2004.
- [7] C. Kammer and D. Aluminium-Zentrale, *Aluminium-Taschenbuch. 1. Grundlagen und Werkstoffe*, 16. Aufl. Düsseldorf: Aluminium-Verl, Berlin ; Wien ua, 2002.
- [8] "USGS Minerals Information: Mineral Commodity Summaries." [Online]. Available: <http://minerals.usgs.gov/minerals/pubs/mcs/>. [Accessed: 13-Jul-2015].
- [9] V. V. Medvedev and S. N. Akhmedov, "Evolution of the Technology for the Production of Alumina from Bauxites," *Light Met. 2014*, pp. 1–9, 2014.
- [10] T. Weisz, *Comparison of the aging behavior in industrial and laboratory-made pure aluminium 6xxx-series alloys*. 2014.
- [11] L. Pinter, *Manufacturing and characterization of Al-Cu and Al-Cu-Mg alloys and analysis of the precipitation kinetics with DSC measurement*. 2010.
- [12] D. G. Eskin, J. Zuidema Jr., V. I. Savran, and L. Katgerman, "Structure formation and macrosegregation under different process conditions during DC casting," *Mater. Sci. Eng. A*, vol. 384, no. 1–2, pp. 232–244, Oct. 2004.
- [13] R. Nadella, D. G. Eskin, Q. Du, and L. Katgerman, "Macrosegregation in direct-chill casting of aluminium alloys," *Prog. Mater. Sci.*, vol. 53, no. 3, pp. 421–480, Mar. 2008.
- [14] D. G. Eskin, *Physical Metallurgy of Direct Chill Casting of Aluminum Alloys*. CRC Press, 2008.
- [15] Z. Cao, F. Jia, X. Zhang, H. Hao, and J. Jin, "Microstructures and mechanical characteristics of electromagnetic casting and direct-chill casting 2024 aluminum alloys," *Mater. Sci. Eng. -Struct. Mater. Prop. Microst*, vol. 327, no. 2, pp. 133–137, 2002.
- [16] M. Ferry, *Direct Strip Casting of Metals and Alloys*. Woodhead Publishing, 2006.

- [17] D. G. Eskin, Suyitno, and L. Katgerman, "Mechanical properties in the semi-solid state and hot tearing of aluminium alloys," *Prog. Mater. Sci.*, vol. 49, no. 5, pp. 629–711, 2004.
- [18] W. H. Suyitno and L. Katgerman, "EVALUATION OF MECHANICAL AND NON-MECHANICAL HOT TEARING CRITERIA FOR DC CASTING OF AN ALUMINUM ALLOY," *Light Met.*, pp. 753–758, 2003.
- [19] J. F. Major, "Porosity control and fatigue behavior in A356-T61 aluminum alloy," *Trans.-Am. Foundrymens Soc.*, pp. 901–906, 1998.
- [20] E. J. Whittenberger and F. N. Rhines, "Origin of porosity in castings of magnesium-aluminum and other alloys," *J. Met.*, vol. 7, pp. 409–420, 1952.
- [21] C. E. Ransley and H. Neufeld, "The solubility of hydrogen in liquid and solid aluminium," *J. Inst. Met.*, vol. 74, no. 12, pp. 599–620, 1948.
- [22] A. Chaijaruwanich, P. D. Lee, R. J. Dashwood, Y. M. Youssef, and H. Nagaumi, "Evolution of pore morphology and distribution during the homogenization of direct chill cast Al–Mg alloys," *Acta Mater.*, vol. 55, no. 1, pp. 285–293, Jan. 2007.
- [23] V. S. Zolotarevsky, M. V. Glazoff, and N. A. Belov, *Casting Aluminum Alloys*. Elsevier, 2010.
- [24] A. R. Eivani, H. Ahmed, J. Zhou, and J. Duszczuk, "Evolution of Grain Boundary Phases during the Homogenization of AA7020 Aluminum Alloy," *Metall. Mater. Trans. A*, vol. 40, no. 3, pp. 717–728, Jan. 2009.
- [25] A. S. M. Handbook, "Volume 4: Heat Treating," *ASM Int.*, pp. 72–74, 1991.
- [26] A. R. Eivani, J. Zhou, and J. Duszczuk, *Microstructural Evolution During the Homogenization of Al-Zn-Mg Aluminum Alloys*. INTECH Open Access Publisher, 2011.
- [27] J. D. Robson and P. B. Prangnell, "Dispersoid precipitation and process modelling in zirconium containing commercial aluminium alloys," *Acta Mater.*, vol. 49, no. 4, pp. 599–613, Feb. 2001.
- [28] S. T. Lim, Y. Y. Lee, and I. S. Eun, "Microstructural Evolution during Ingot Preheat in 7xxx Aluminium Alloys for Thick Semiproduct Applications," *Mater. Sci. Forum*, vol. 519–521, pp. 549–554, 2006.
- [29] J. D. Robson, "Optimizing the homogenization of zirconium containing commercial aluminium alloys using a novel process model," *Mater. Sci. Eng. A*, vol. 338, no. 1–2, pp. 219–229, Dec. 2002.
- [30] Y. Deng, Y. Zhang, L. Wan, A. A. Zhu, and X. Zhang, "Three-Stage Homogenization of Al-Zn-Mg-Cu Alloys Containing Trace Zr," *Metall. Mater. Trans. A*, vol. 44, no. 6, pp. 2470–2477, Feb. 2013.
- [31] T. Gladman, "Precipitation hardening in metals," *Mater. Sci. Technol.*, vol. 15, no. 1, pp. 30–36, Jan. 1999.
- [32] H. R. Mohammadian Semnani, *Precipitation kinetics in al-alloys observed by dilatometry*. 2009.
- [33] H.-J. Bargel and G. Schulze, Eds., *Werkstoffkunde*. Berlin, Heidelberg: Springer Berlin Heidelberg, 2008.
- [34] A. R. Farkoosh, X. Grant Chen, and M. Pekguleryuz, "Dispersoid strengthening of a high temperature Al–Si–Cu–Mg alloy via Mo addition," *Mater. Sci. Eng. A*, vol. 620, pp. 181–189, Jan. 2015.
- [35] L. F. Mondolfo, *Aluminum Alloys: Structure and Properties*. Elsevier, 2013.

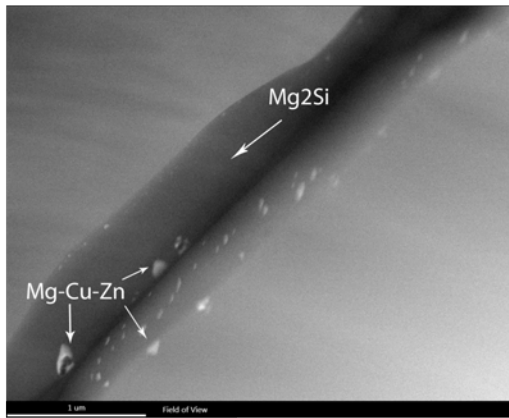
- [36] G. Peng, K. Chen, H. Fang, and S. Chen, "Effect of Cr and Yb additions on microstructure and properties of low copper Al–Zn–Mg–Cu–Zr alloy," *Mater. Des.*, vol. 36, pp. 279–283, Apr. 2012.
- [37] B. Ilshner and R. F. Singer, *Werkstoffwissenschaften und Fertigungstechnik: Eigenschaften, Vorgänge, Technologien*. Springer-Verlag, 2013.
- [38] E. Arzt, R. Behr, E. Göhring, P. Grahle, and R. P. Mason, "Dispersion strengthening of intermetallics," *Mater. Sci. Eng. A*, vol. 234–236, pp. 22–29, Aug. 1997.
- [39] H. C. Fang, K. H. Chen, X. Chen, L. P. Huang, G. S. Peng, and B. Y. Huang, "Effect of Zr, Cr and Pr additions on microstructures and properties of ultra-high strength Al–Zn–Mg–Cu alloys," *Mater. Sci. Eng. A*, vol. 528, no. 25–26, pp. 7606–7615, Sep. 2011.
- [40] P. Lehto, H. Remes, T. Saukkonen, H. Hänninen, and J. Romanoff, "Influence of grain size distribution on the Hall–Petch relationship of welded structural steel," *Mater. Sci. Eng. A*, vol. 592, pp. 28–39, Jan. 2014.
- [41] K. E. Knipling, D. N. Seidman, and D. C. Dunand, "Ambient- and high-temperature mechanical properties of isochronally aged Al–0.06Sc, Al–0.06Zr and Al–0.06Sc–0.06Zr (at.%) alloys," *Acta Mater.*, vol. 59, no. 3, pp. 943–954, Feb. 2011.
- [42] Y. Zhang, C. Bettles, and P. A. Rometsch, "Effect of recrystallisation on Al₃Zr dispersoid behaviour in thick plates of aluminium alloy AA7150," *J. Mater. Sci.*, vol. 49, no. 4, pp. 1709–1715, Nov. 2013.
- [43] J. D. Robson, "A new model for prediction of dispersoid precipitation in aluminium alloys containing zirconium and scandium," *Acta Mater.*, vol. 52, no. 6, pp. 1409–1421, Apr. 2004.
- [44] Z. Y. Guo, G. Zhao, Y. Liu, and N. Tian, "The Effect of Pretreatment and Homogenization on the Precipitation of Spherical Al₃Zr Phase in Aluminium Alloy Containing Trace of Zr," *Adv. Mater. Res.*, vol. 287–290, pp. 1140–1143, Jul. 2011.
- [45] E. Nes, "Precipitation of the metastable cubic Al₃Zr-phase in subperitectic Al–Zr alloys," *Acta Metall.*, vol. 20, no. 4, pp. 499–506, Apr. 1972.
- [46] B. Morere, R. Shahani, C. Maurice, and J. Driver, "The influence of Al₃Zr dispersoids on the recrystallization of hot-deformed AA 7010 alloys," *Metall. Mater. Trans. A*, vol. 32, no. 3, pp. 625–632, Mar. 2001.
- [47] G. M. Ludtka and D. E. Laughlin, "The Effect of Solute Content on the Slip Behavior in 7XXX Series Aluminum Alloys," *Metall. Trans. A*, vol. 12, no. 12, pp. 2083–2091, Dec. 1981.
- [48] R. Kaibyshev, O. Sitdikov, A. Goloborodko, and T. Sakai, "Deformation Behavior of 7475 Aluminum Alloy at High Temperature," in *Key Engineering Materials*, 1999, vol. 171, pp. 355–362.
- [49] T. Sakai, H. Miura, A. Goloborodko, and O. Sitdikov, "Continuous dynamic recrystallization during the transient severe deformation of aluminum alloy 7475," *Acta Mater.*, vol. 57, no. 1, pp. 153–162, Jan. 2009.
- [50] C. C. Bampton and J. W. Edington, "Microstructural observations of superplastic cavitation in fine grained 7475–Al," *Metall. Trans. A*, vol. 13, no. 10, pp. 1721–1727, Oct. 1982.
- [51] C. Q. Chen and J. F. Knott, "Effects of dispersoid particles on toughness of high-strength aluminium alloys," *Met. Sci.*, vol. 15, no. 8, pp. 357–364, Aug. 1981.

- [52] R. Ayer, J. Y. Koo, J. W. Steeds, and B. K. Park, "Microanalytical study of the heterogeneous phases in commercial Al-Zn-Mg-Cu alloys," *Metall. Trans. A*, vol. 16, no. 11, pp. 1925–1936, Nov. 1985.
- [53] T. C. Tsai and T. H. Chuang, "Role of grain size on the stress corrosion cracking of 7475 aluminum alloys," *Mater. Sci. Eng. A*, vol. 225, no. 1–2, pp. 135–144, Apr. 1997.
- [54] P. ACHON, J. EHRSTROM, and A. PINEAU, "Microstructural modeling of the fracture toughness of 7000 Al alloys," in *ECF11, Poitiers 1996*, 2013.
- [55] Z. Chen, Y. Mo, and Z. Nie, "Effect of Zn Content on the Microstructure and Properties of Super-High Strength Al-Zn-Mg-Cu Alloys," *Metall. Mater. Trans. A*, vol. 44, no. 8, pp. 3910–3920, Apr. 2013.
- [56] F. Xie, X. Yan, L. Ding, F. Zhang, S. Chen, M. G. Chu, and Y. A. Chang, "A study of microstructure and microsegregation of aluminum 7050 alloy," *Mater. Sci. Eng. A*, vol. 355, no. 1–2, pp. 144–153, Aug. 2003.
- [57] A. N. Abood, M. H. Tolephih, and E. J. Ebraheam, "Effect of Diffusion Bonding on Fatigue Strength of Aluminum Alloy AA 7020-O."
- [58] I. Charit, R. S. Mishra, and M. W. Mahoney, "Multi-sheet structures in 7475 aluminum by friction stir welding in concert with post-weld superplastic forming," *Scr. Mater.*, vol. 47, no. 9, pp. 631–636, Nov. 2002.
- [59] O. Sitdikov, T. Sakai, A. Goloborodko, and H. Miura, "Grain fragmentation in a coarse-grained 7475 Al alloy during hot deformation," *Scr. Mater.*, vol. 51, no. 2, pp. 175–179, Jul. 2004.
- [60] L. Lazzarini, L. Nasi, and V. Grillo, "Transmission electron microscopy techniques for imaging and compositional evaluation in semiconductor heterostructures-5." Elsevier Science & Technology.
- [61] J. Thomas and T. Gemming, *Analytische Transmissionselektronenmikroskopie: Eine Einführung für den Praktiker*. Springer-Verlag, 2013.
- [62] R. Egerton, *Electron Energy-Loss Spectroscopy in the Electron Microscope*. Springer Science & Business Media, 2011.
- [63] F. Uyama, *Untersuchungen auf dem Gebiet der Al-Mg-Si- und Al/Mg₂Si-in-situ-Legierungen*. 2007.
- [64] X. M. Li and M. J. Starink, "Identification and analysis of intermetallic phases in overaged Zr-containing and Cr-containing Al-Zn-Mg-Cu alloys," *J. Alloys Compd.*, vol. 509, no. 2, pp. 471–476, Jan. 2011.
- [65] X. Fan, D. Jiang, Q. Meng, and L. Zhong, "The microstructural evolution of an Al-Zn-Mg-Cu alloy during homogenization," *Mater. Lett.*, vol. 60, no. 12, pp. 1475–1479, Jun. 2006.
- [66] J. D. Robson, "Microstructural evolution in aluminium alloy 7050 during processing," *Mater. Sci. Eng. A*, vol. 382, no. 1–2, pp. 112–121, Sep. 2004.
- [67] W. D. Callister, *Materials Science and Engineering: An Introduction*, 7. Auflage. New York: John Wiley & Sons, 2006.
- [68] L.-M. Wu, W.-H. Wang, Y.-F. Hsu, and S. Trong, "Effects of homogenization treatment on recrystallization behavior and dispersoid distribution in an Al-Zn-Mg-Sc-Zr alloy," *J. Alloys Compd.*, vol. 456, no. 1–2, pp. 163–169, May 2008.
- [69] B. Forbord, W. Lefebvre, F. Danoix, H. Hallem, and K. Marthinsen, "Three dimensional atom probe investigation on the formation of Al₃(Sc,Zr)-

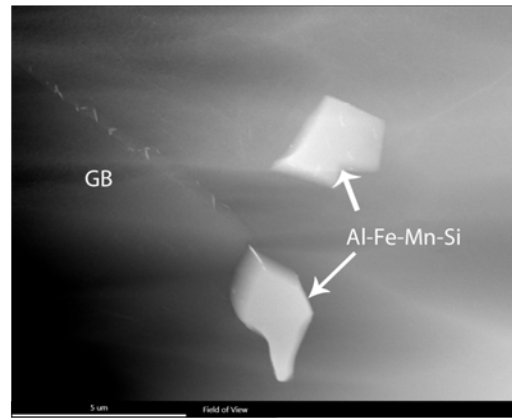
- dispersoids in aluminium alloys," *Scr. Mater.*, vol. 51, no. 4, pp. 333–337, Aug. 2004.
- [70] O. N. Senkov, R. B. Bhat, S. V. Senkova, and J. Tatalovich, "Effect of Sc and Heat Treatment on Microstructure and Properties of a 7XXX DC Cast Alloy," Mar. 2004.
- [71] Z. Jia, G. Hu, B. Forbord, and J. K. Solberg, "Effect of homogenization and alloying elements on recrystallization resistance of Al–Zr–Mn alloys," *Mater. Sci. Eng. A*, vol. 444, no. 1, pp. 284–290, 2007.
- [72] M. Ahmadi, E. Povoden-Karadeniz, K. I. Oksuz, A. Falahati, and E. Kozeschnik, "A model for precipitation strengthening in multi-particle systems," *Comput. Mater. Sci.*, vol. 91, pp. 173–186, 2014.
- [73] Y. Deng, Z. Yin, K. Zhao, J. Duan, and Z. He, "Effects of Sc and Zr microalloying additions on the microstructure and mechanical properties of new Al–Zn–Mg alloys," *J. Alloys Compd.*, vol. 530, pp. 71–80, Jul. 2012.

A. Appendix

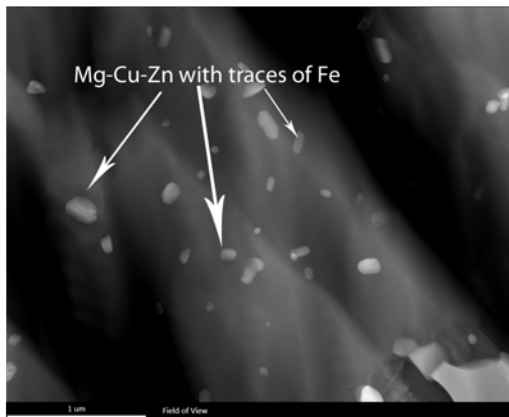
7020 - TEM/STEM images



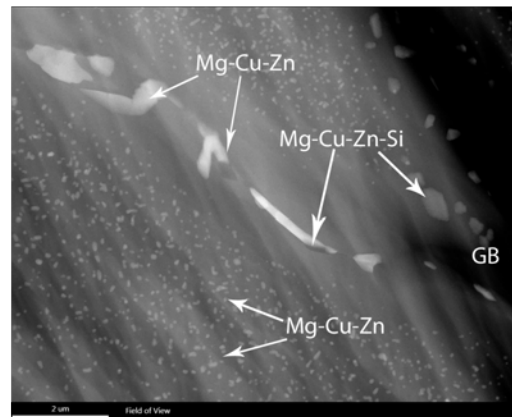
(a) Sample 1



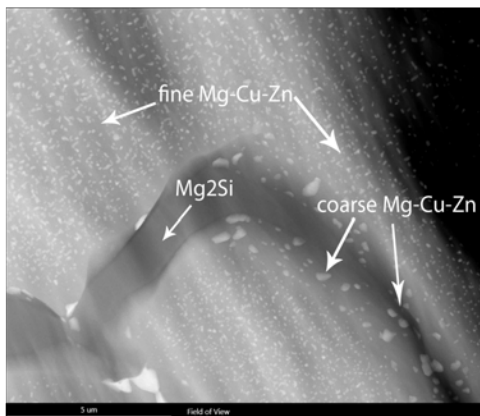
(b) Sample 1



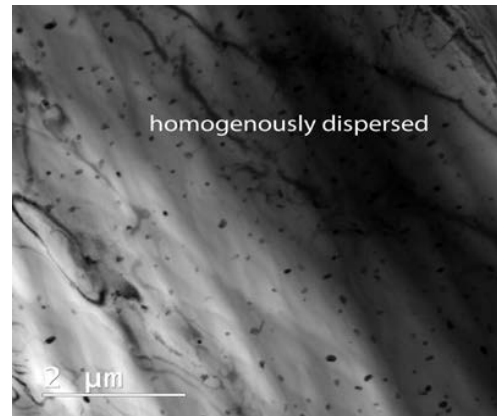
(c) Sample 2



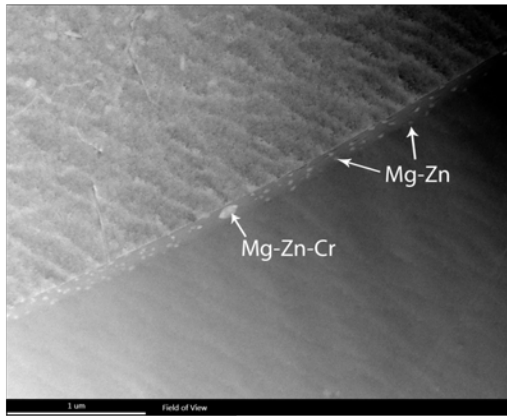
(d) Sample 2



(e) Sample 2



(f) Sample 2



(g) Sample 3



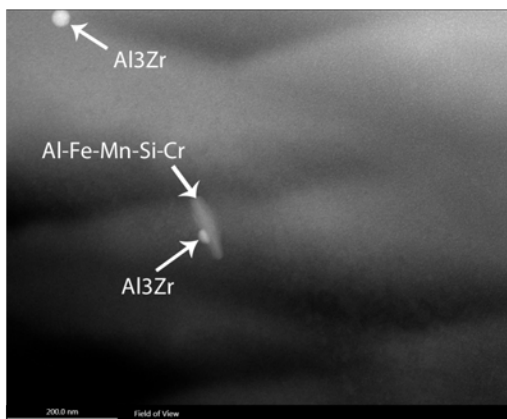
(h) Sample 3



(i) Sample 3



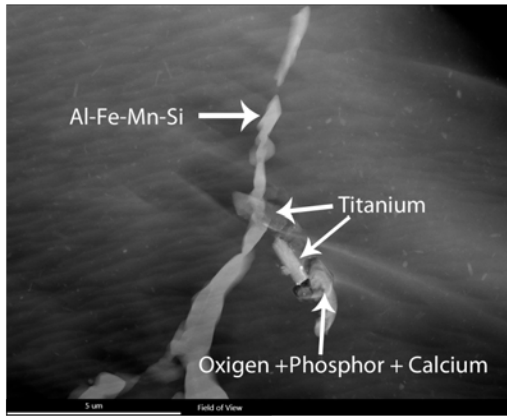
(j) Sample 4



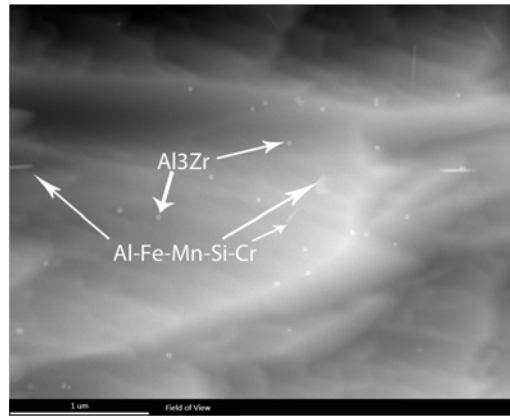
(k) Sample 4



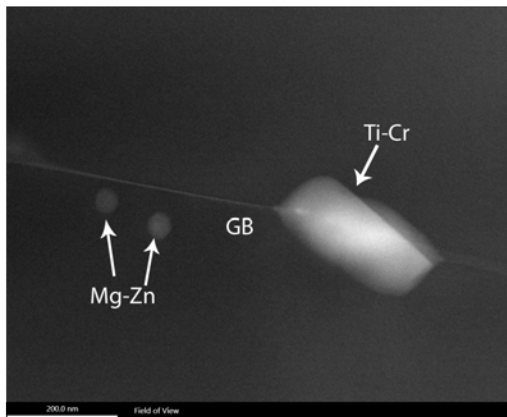
(l) Sample 4



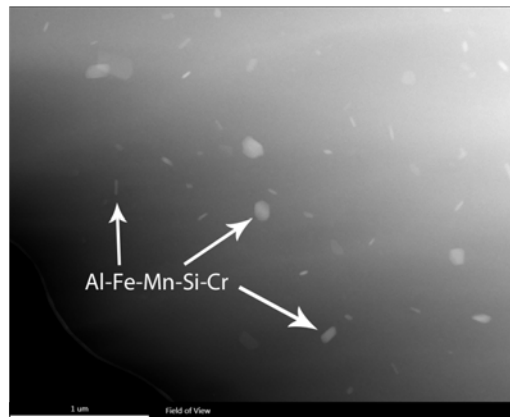
(m) Sample 4



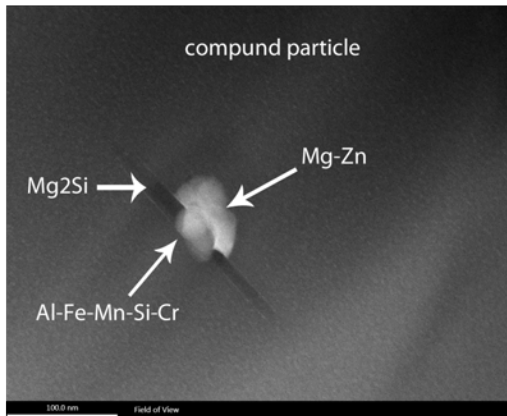
(n) Sample 5



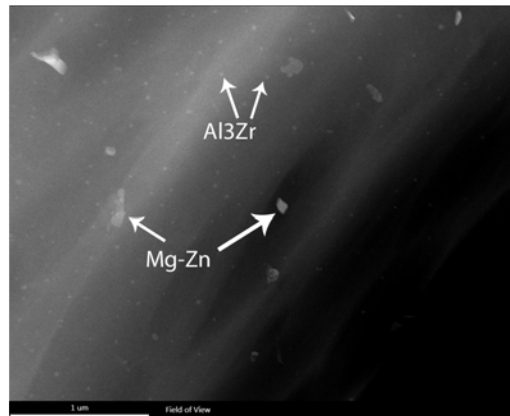
(o) Sample 5



(p) Sample 5



(q) Sample 6



(r) Sample 6

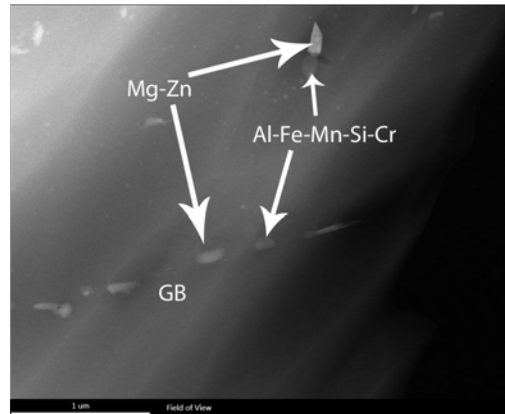


Figure A -1 TEM/STEM images [7020]

(s) Sample 6

Observations:

Sample 1:

In the as-cast structure we find 3 different second phase particles. Coarse intermetallic particles, Mg-Si particles and a phase containing Mg-Cu-Zn. On the GB we find large Mg-Si particles together with the Mg-Cu-Zn phase (Figure 6.1.1-1 (a)). The Mg-Cu-Zn phase only contains traces of Cu. The Al-Fe-Mn-Si particles with traces of Cr can be found near the GB and also within the grain. Those particles tend to be very coarse.

Sample 2:

Within the grain the Mg-Cu-Zn phase is fine and homogenously dispersed. On the GB large Mg-Cu-Zn phases can be found along with large amounts of Mg-Si particles. In some Mg-Cu-Zn phases Si was also found, this might be due to a Mg-Si particle beneath or above. Furthermore were some Mg-Cu-Zn particles found with traces of Fe. The intermetallic particles stay unchanged.

Sample 3:

On the large Al-Fe-Mn-Si-Cr phase Zr-containing and Mg-Cu-Zn-containing particles were encountered quite frequently (Figure 6.1.1-1 (h)). One particle containing a considerable amount of Cr was found on a GB. With some exceptions, most of the Mg-Zn-Cu phase has dissolved into the matrix.

Sample 4:

No more Mg-Cu-Zn phase could be found. The only coarse phase left is the Al-Fe-Mn-Si-Cr phase. Zr-containing dispersoids grow in number. Near the GB 2 Ti-particles were detected, next to some O-P-Ca containing particles (Figure 6.1.1-1 (m)).

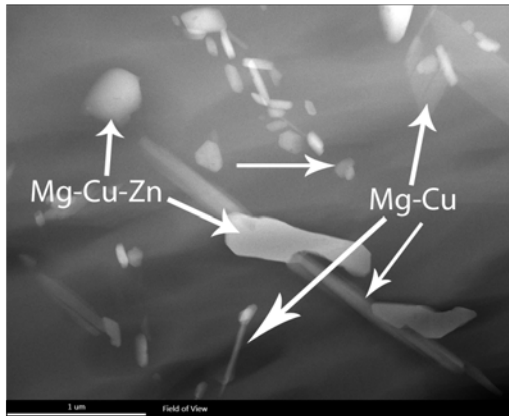
Sample 5:

Large Mg-Zn particles can be found again along the GB with the still unsolved Al-Fe-Mn-Si-Cr particles (Figure 6.1.1-1 (n), (o)). A Cr dispersoid containing traces of Ti was also detected along the GB (Figure 6.1.1-1 (o)). Zr-containing dispersoids are still not homogenously distributed. On

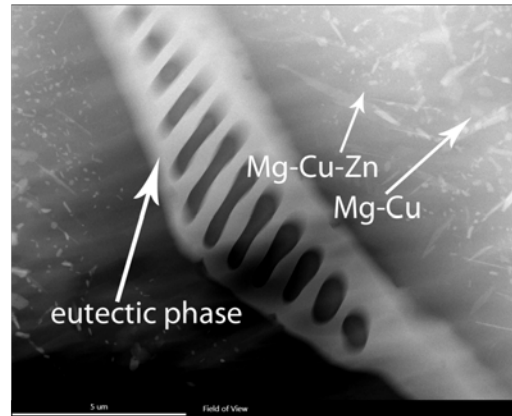
certain areas no Zr was found while on other areas an ample amount of those dispersoids was encountered (Figure 6.1.1-1 (n), Figure 6.1.1-1 (p)).

Sample 6: This probe was taken at the end of the homogenization process. All three phases from the as-cast structure can be found again with the addition of the Zr-containing dispersoids (Figure 6.1.1-1 (q)). The dispersoids were still not homogeneously distributed throughout the grain.

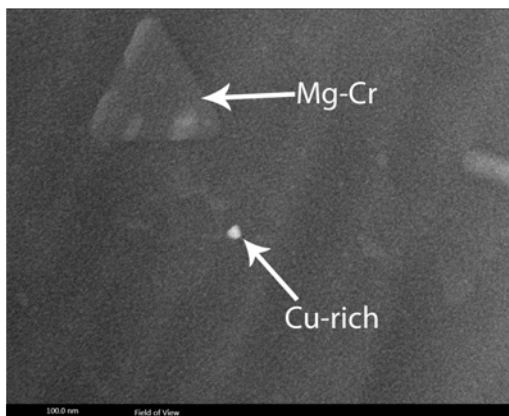
7475 - TEM/STEM images



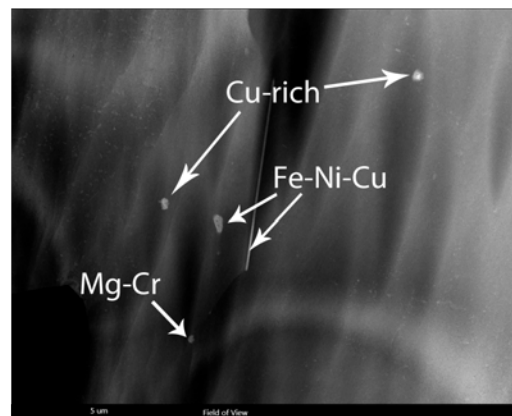
(a) Sample 1



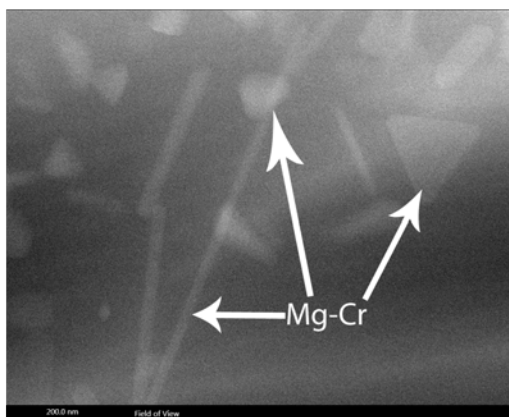
(b) Sample 1



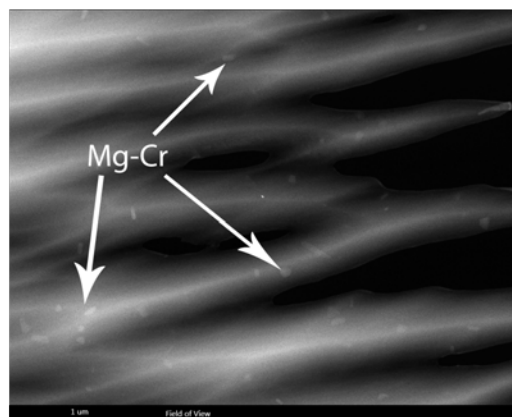
(c) Sample 2



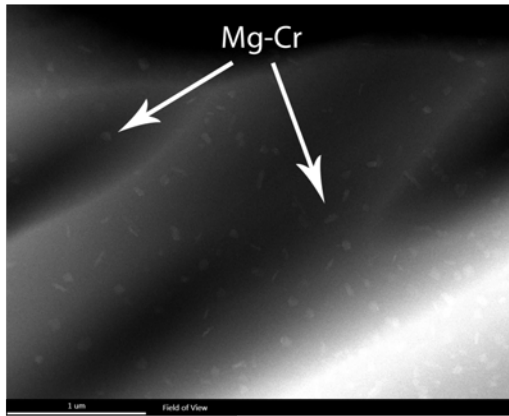
(d) Sample 2



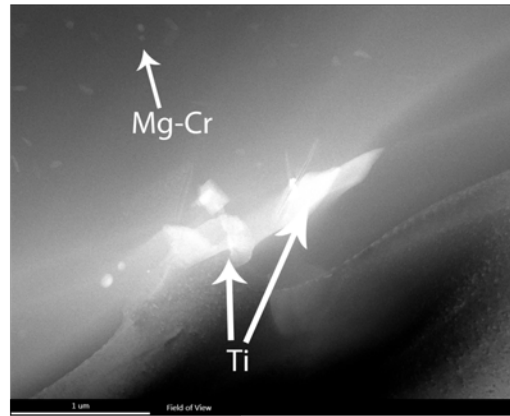
(e) Sample 3



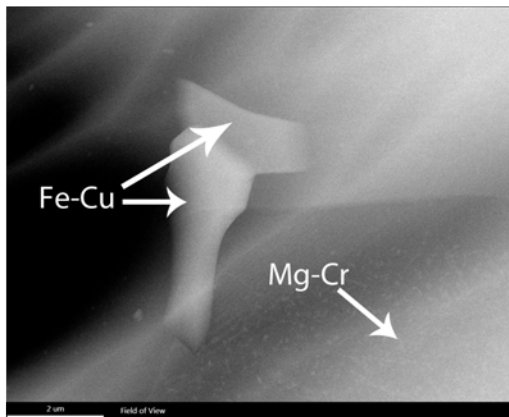
(f) Sample 3



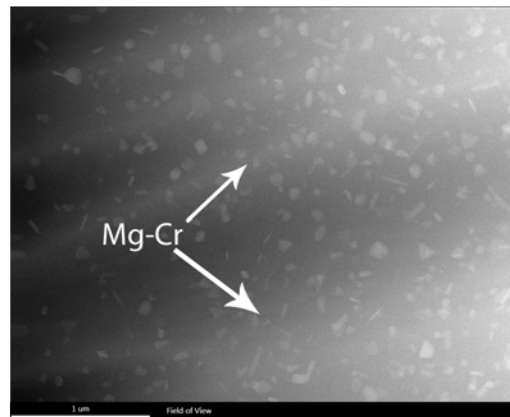
(g) Sample 4



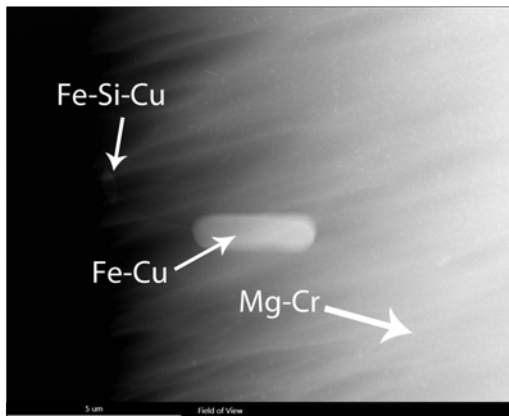
(h) Sample 4



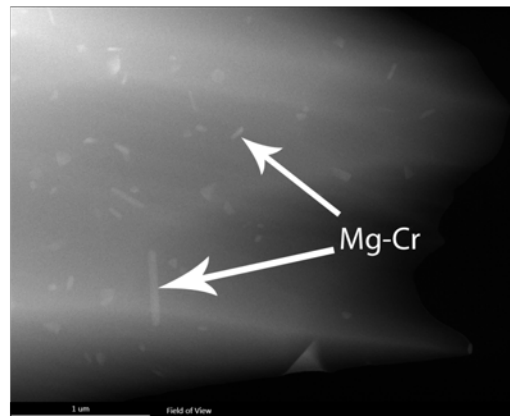
(i) Sample 4



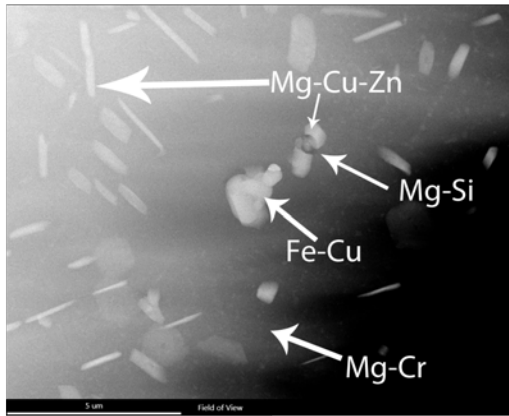
(j) Sample 5



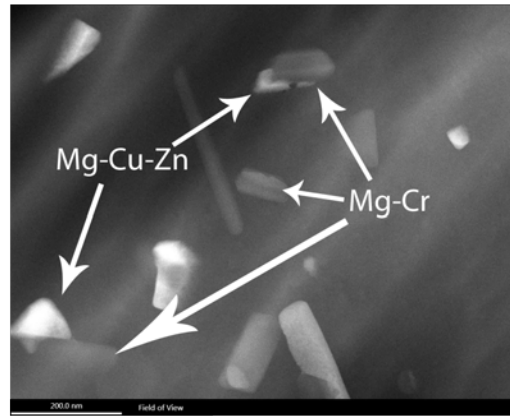
(k) Sample 5



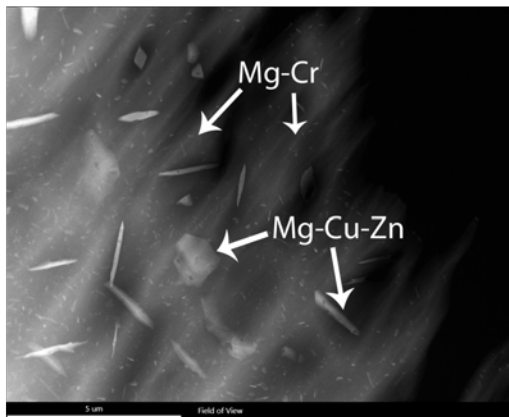
(l) Sample 6



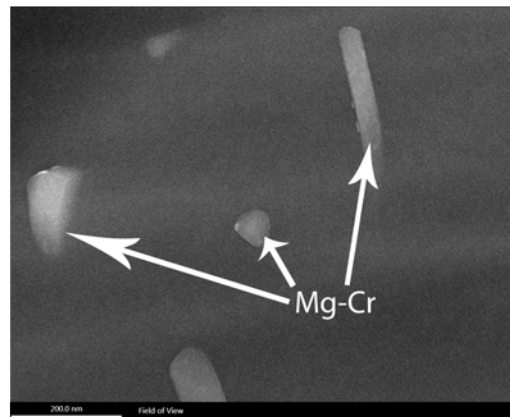
(m) Sample 6



(n) Sample 7



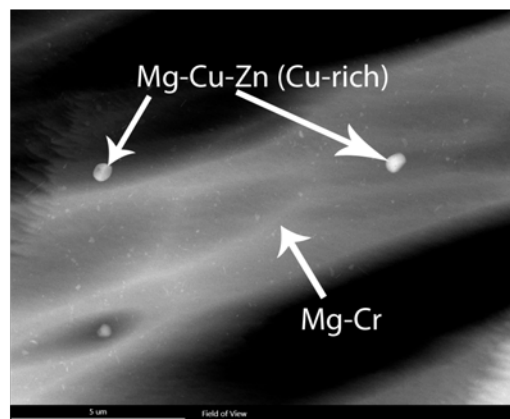
(o) Sample 7



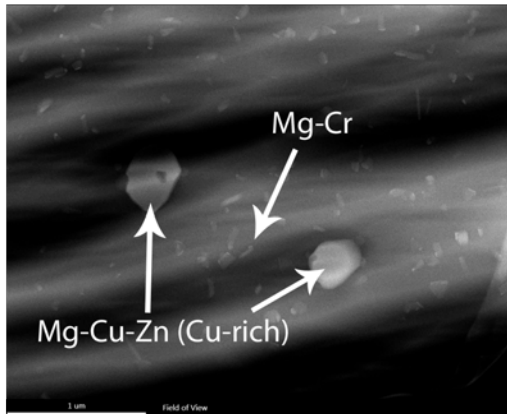
(p) Sample 8



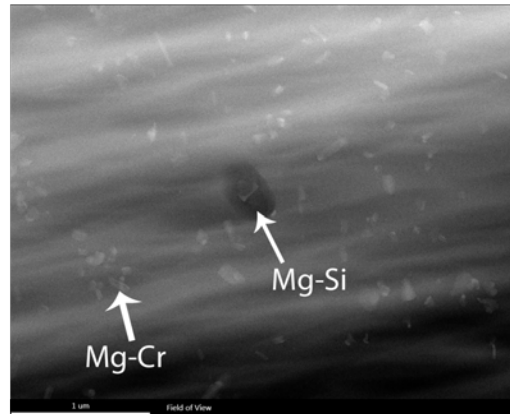
(q) Sample 8



(r) Sample 8



(s) Sample 9



(t) Sample 9

Figure A - 2 TEM/STEM images [7475]

Observations:

Sample 1:

The as-cast structure is filled with Mg-Cu-Zn and Mg-Cu phase (Figure 6.2.1-1 (a)). The GB's are populated with the eutectic phase and Mg-Si was encountered (Figure 6.2.1-1 (b)).

Sample 2:

The Mg-Cu-Zn phase seems to have dissolved completely. Some particles with very high amounts of Cu are still within the matrix (Figure 6.2.1-1 (c)). The intermetallic particles show high amounts of Fe and Cu with traces of Ni. Mg-Cr containing dispersoids precipitated, but not quite homogeneously and with a fairly low ND (Figure 6.2.1-1 (d)).

Sample 3:

The amount of encountered Cu-rich particles reduced and the matrix is now filled homogeneously with a high number of Cr dispersoids (Figure 6.2.1-1 (f)). The dispersoids seem to have all kinds of different shapes and sizes (Figure 6.2.1-1 (e)). Along the GB some Mg-Cu-Zn and some Mg-Cu phase was found.

Sample 4:

Along with large intermetallic particles a Ti containing phase was encountered (Figure 6.2.1-1 (h)). The Cr dispersoids are present in ND and throughout the grain.

Sample 5:

Apart from coarse intermetallic particles and dispersoids no other phase was detected within the matrix (Figure 6.2.1-1 (k)).

Sample 6:

Very large (>1 μm) Mg-Cu-Zn phase precipitated back into the matrix (Figure 6.2.1-1 (m)). Mg-Si and intermetallic particles were also encountered. The Cr-dispersoids fill the matrix between the large particles.

Sample 7:

At the end of homogenization the matrix is populated again with Mg-Cu-Zn in various sizes and shapes (Figure 6.2.1-1 (o)). Mg-Si was found. Some Cr dispersoids contained traces of Ti and a large Ti particle was found again.

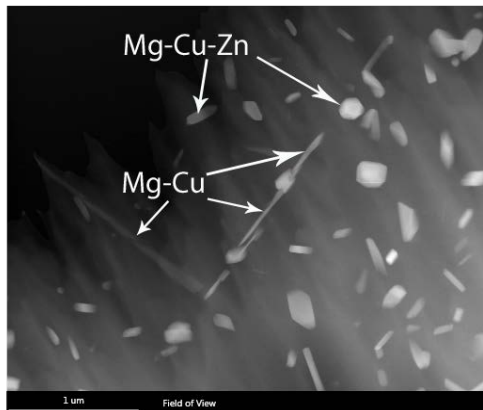
Sample 8:

The Mg-Cu-Zn particles show a very high amount of Cu and are thus referred to as Cu-rich Mg-Cu-Zn phase (Figure 6.2.1-1 (r)). Apart from some coarse intermetallic, Mg-Si and a Ti particles the matrix is only populated by Cr dispersoids (Figure 6.2.1-1 (q)).

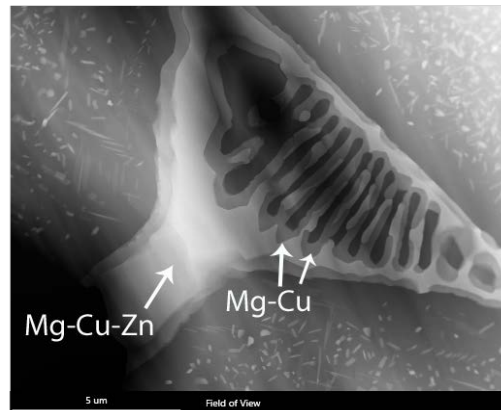
Sample 9:

The Cu-rich Mg-Cu-Zn phase and the Mg-Si phase are still present (Figure 6.2.1-1 (s)). The rest of the matrix is homogeneously filled with Cr dispersoids. Some Mg-Cu phase was found near along the GB.

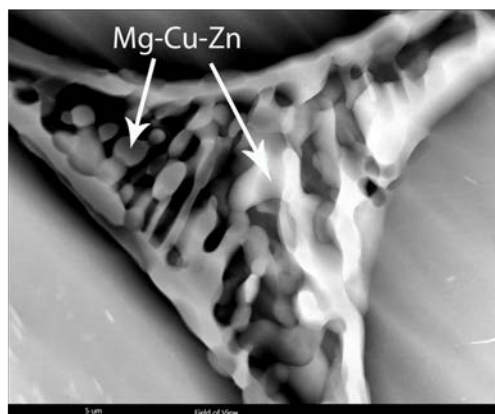
7050 – TEM/STEM images



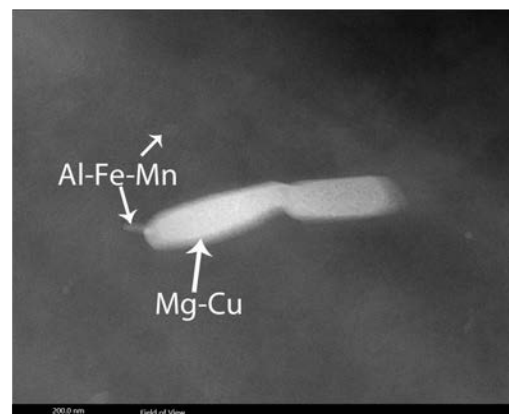
(a) Sample 1



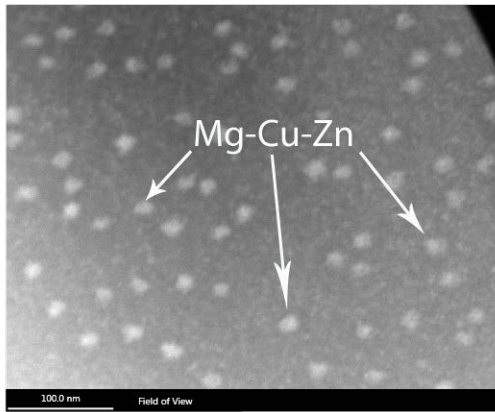
(b) Sample 1



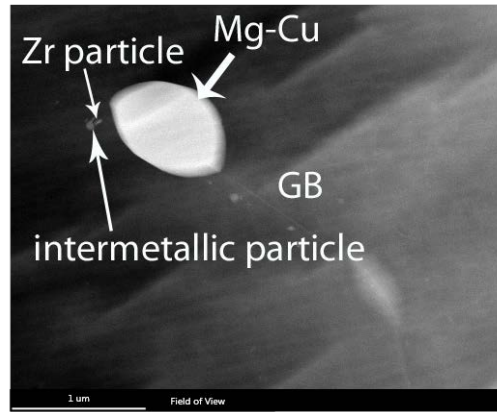
(c) Sample 2



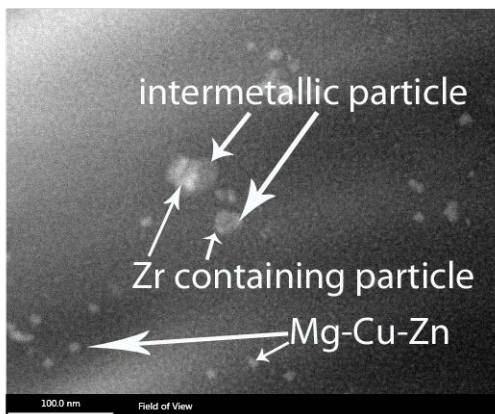
(d) Sample 2



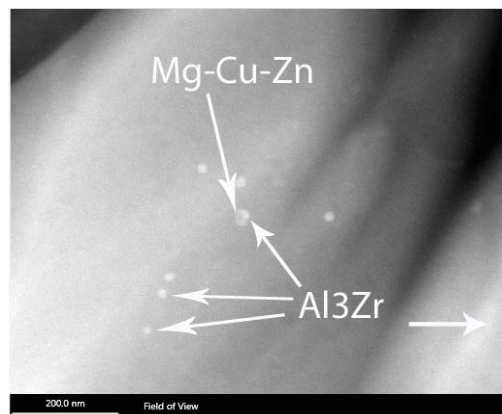
(e) Sample 2



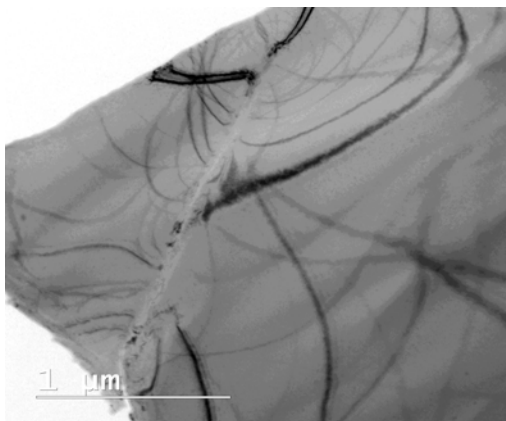
(f) Sample 3



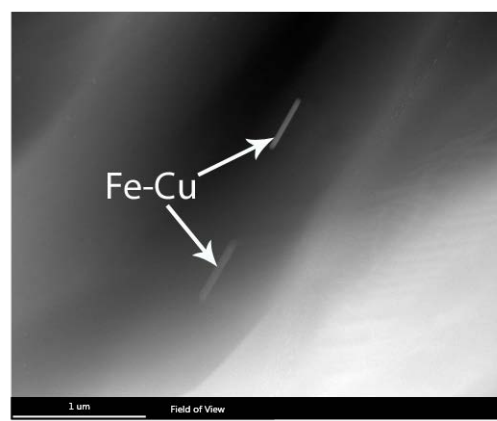
(g) Sample 3



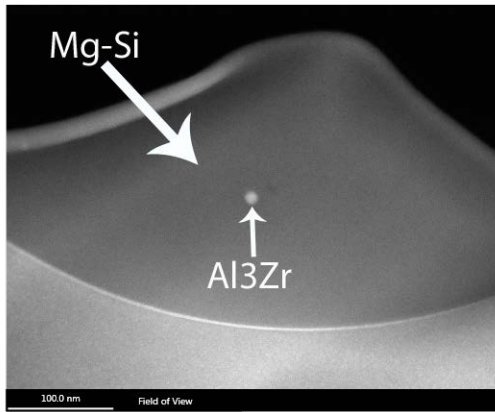
(h) Sample 4



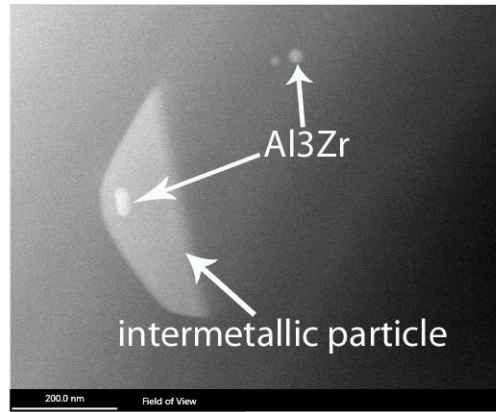
(i) Sample 4



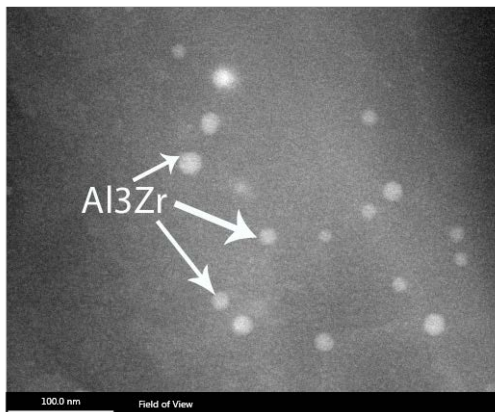
(j) Sample 5



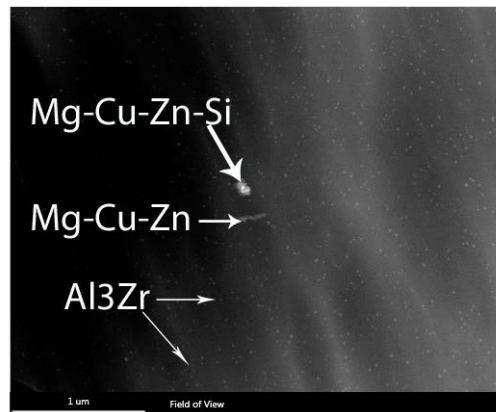
(k) Sample 5



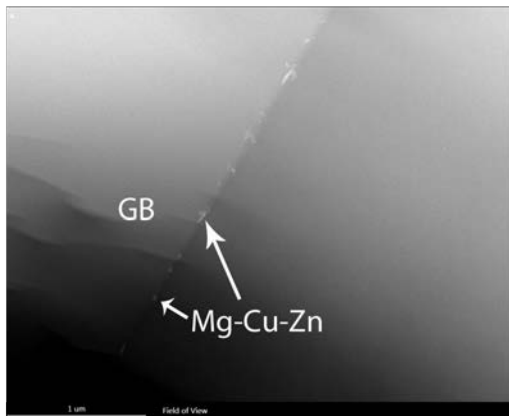
(l) Sample 5



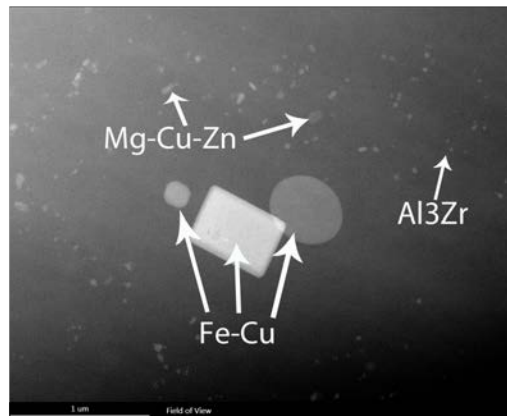
(m) Sample 6



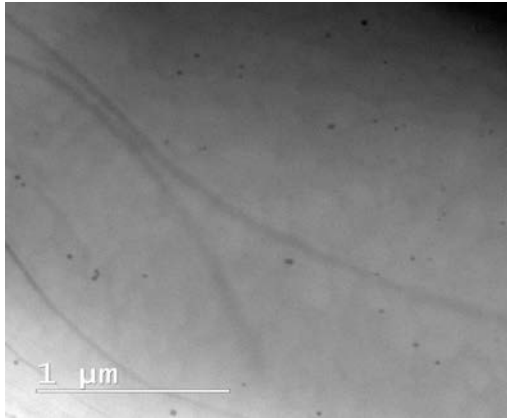
(n) Sample 6



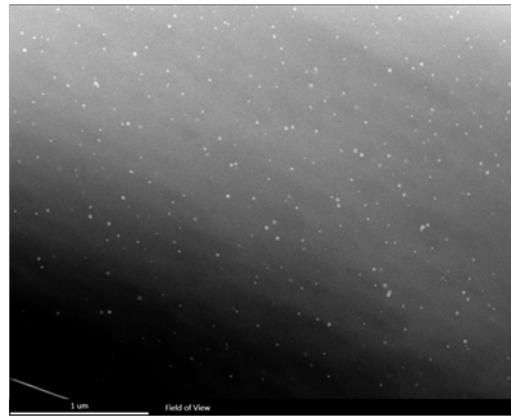
(o) Sample 7



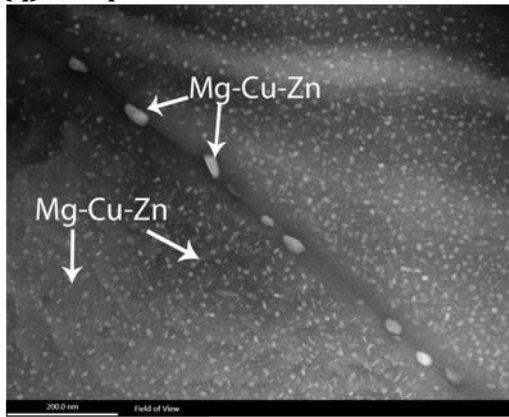
(p) Sample 7



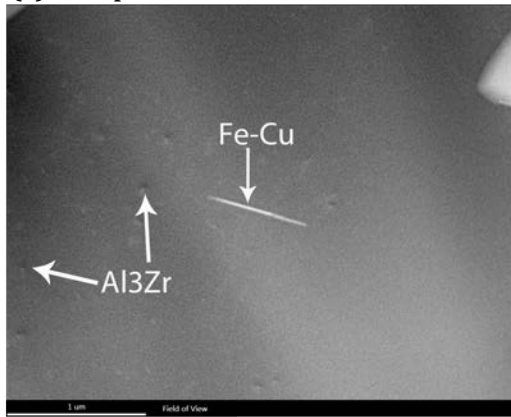
(q) Sample 7



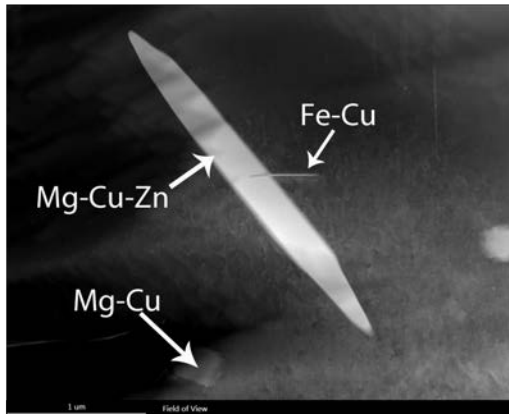
(r) Sample 7



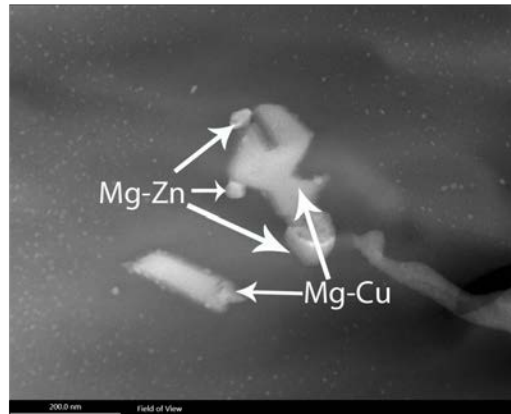
(s) Sample 8



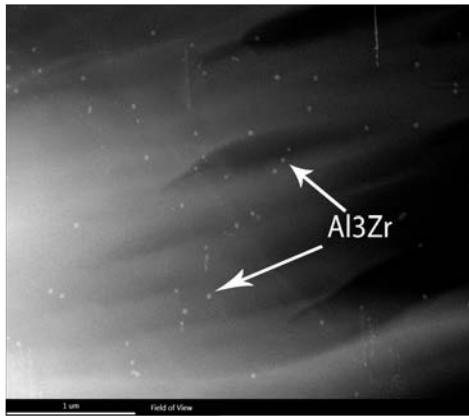
(t) Sample 8



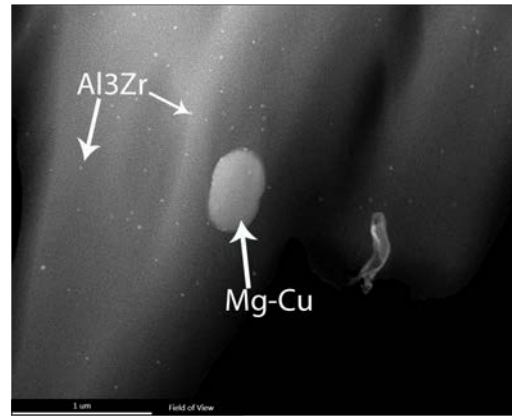
(u) Sample 9



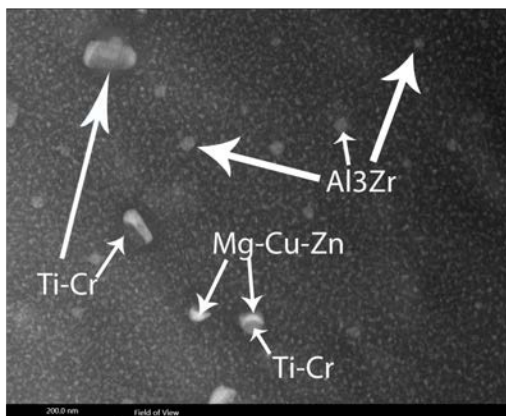
(v) Sample 9



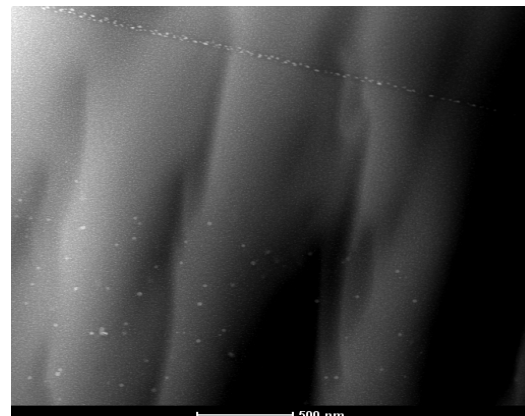
(w) Sample 9



(x) Sample 10



(y) Sample 11



(z) Sample 11

Figure A - 3 TEM/STEM images [7050]

Observations:

Sample 1:

In the as-cast structure we found a Mg-Cu, Mg-Cu-Zn and a Mg-Si phase. The matrix is filled with Mg-Cu and Mg-Cu-Zn particles some containing tiny amounts of Fe. Large eutectic phases appear along the GB, visible through their laminar structure.

Sample 2:

The Mg-Cu-Zn particles start to spheroidize and shrink. A few Al-Fe-Mn containing particles were found. The eutectic phase dissolves more and more (Figure 6.3.1-1 (c)). The total amount of particles within the matrix is decreasing. Some Al-Cu particles appeared.

Sample 3:

For the first time we find Zr (Figure 6.3.1-1 (g)). On the GB as well as within the grain, Zr-containing particles were found to nucleate on Fe containing particles. Along the GB coarse Mg-Cu phase can still be encountered. The Mg-Cu-Zn particles reduce again in size and amount.

Sample 4:

Zr-containing particles appear in greater number and size than before. We still run into some Mg-Cu-Zn particles but they are very rare and small (Figure 6.3.1-1 (h)). Apart from a few contamination particles and the Zr-containing ones the matrix within the grain is empty (Figure 6.3.1-1 (i)).

Sample 5:

Zr particles were found on Mg-Si and Fe-Cu particles as well as within the grain (Figure 6.3.1-1 (k)). For the first time we find some coarse (greater than 1 μm) particles consisting only of Fe-Cu (Figure 6.3.1-1 (l)).

Sample 6:

The matrix is now homogeneously filled with dispersoids in a high number density (Figure 6.3.1-1 (m)). A phase with a large amount of Si and Cu was detected next to a Mg-Cu-Zn phase (Figure 6.3.1-1 (n)).

Sample 7:

We find areas with a higher and lower dispersoid number density (Figure 6.3.1-1 (q) and (r)). Although in most of the grain it appears to be homogeneously distributed, some areas have very few Zr-containing particles. The Fe-Cu rich phase is still present within the grain and along the GB the Mg-Cu-Zn phase still exists.

Sample 8:

Very small Mg-Cu-Zn particles nucleate homogeneously within the matrix (Figure 6.3.1-1 (s)). The coarse Fe-Cu phase has still not dissolved (Figure 6.3.1-1 (t)).

Sample 9:

This state represents the end of the homogenization. The ND of the Zr-containing dispersoids varies strongly within the grain. While some regions show a high ND others seem to have only a few dispersoids (Figure 6.3.1-1 (u) and (w)). They appear to have decreased in ND but gained in size. Mg-Cu-Zn and Mg-Cu phase has precipitated again. The matrix is filled with a large variety of particles in all shapes and sizes (Figure 6.3.1-1 (v)).

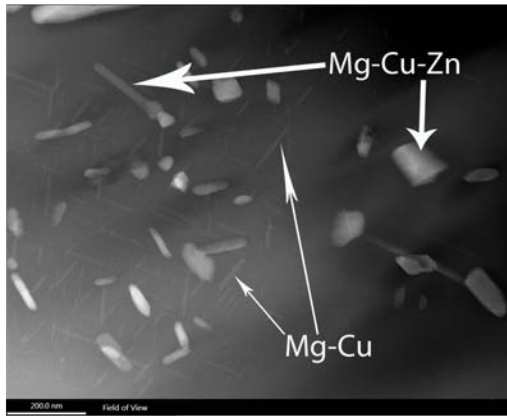
Sample 10:

Most of the phases have dissolved back into the matrix. A few very coarse Mg-Cu particles are left. The PFZ is clearly visible but strongly varies in distance (Figure 6.3.1-1 (x)).

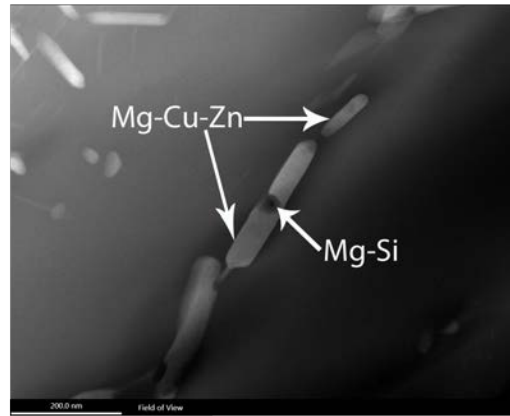
Sample 11:

For the first time we find a Ti-Cr containing dispersoid (Figure 6.3.1-1 (y)). Clear PFZ's can be seen, which vary strongly in size (Figure 6.3.1-1 (z)).

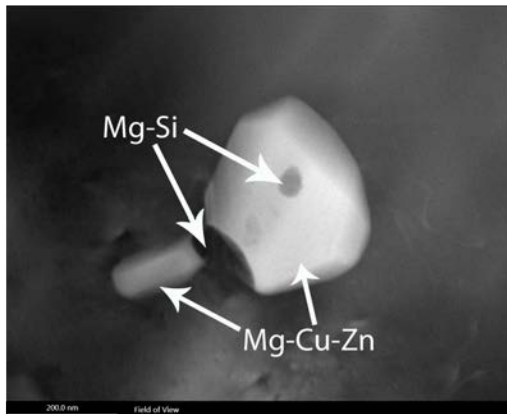
TITANAL – TEM/STEM images



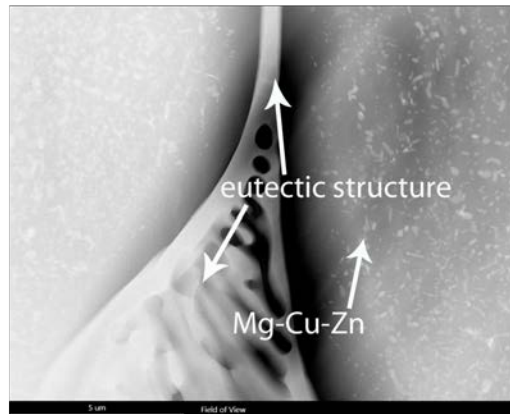
(a) Sample 1



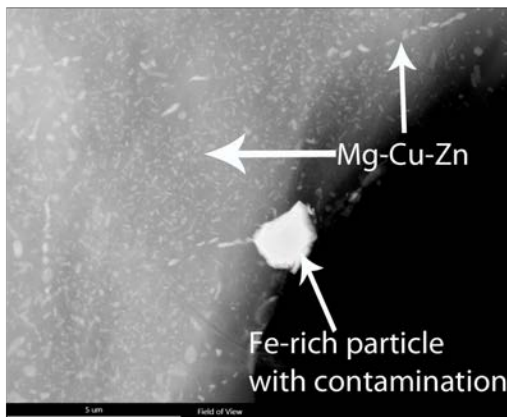
(b) Sample 1



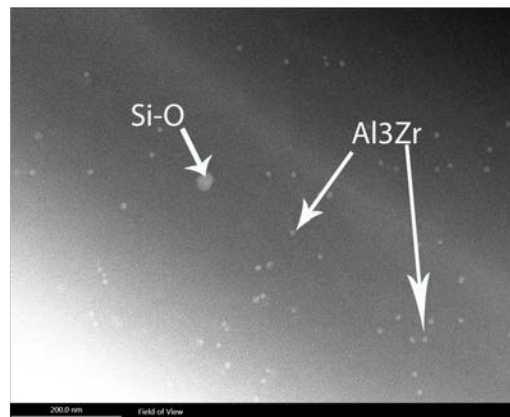
(c) Sample 2



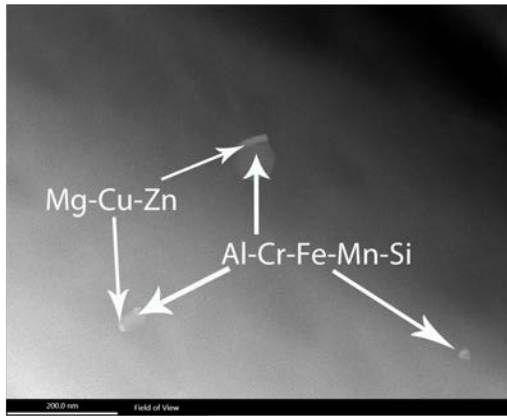
(d) Sample 2



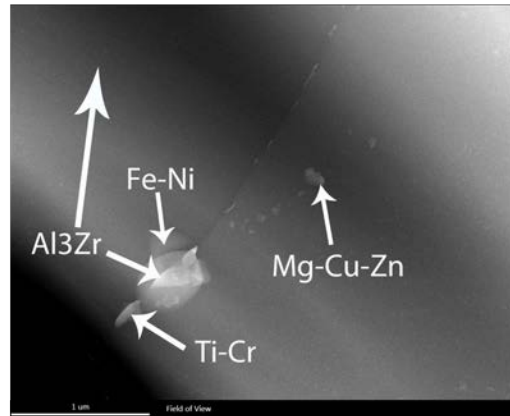
(e) Sample 2



(f) Sample 3



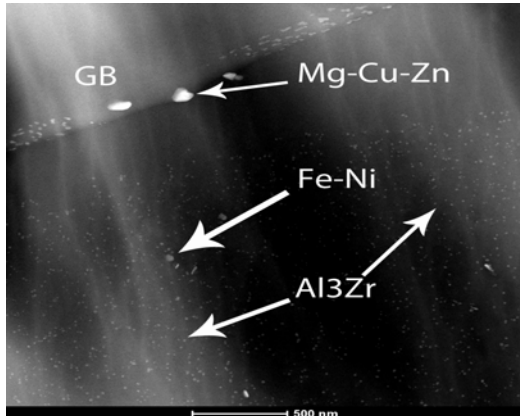
(g) Sample 3



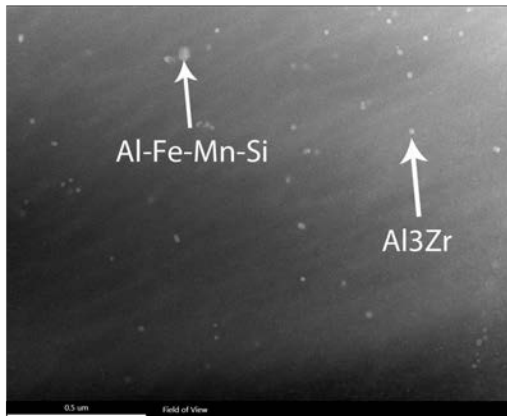
(h) Sample 4



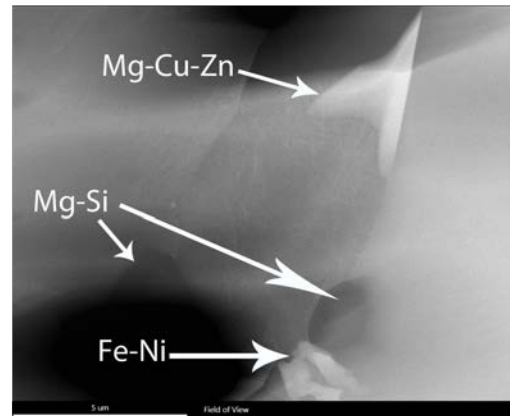
(i) Sample 4



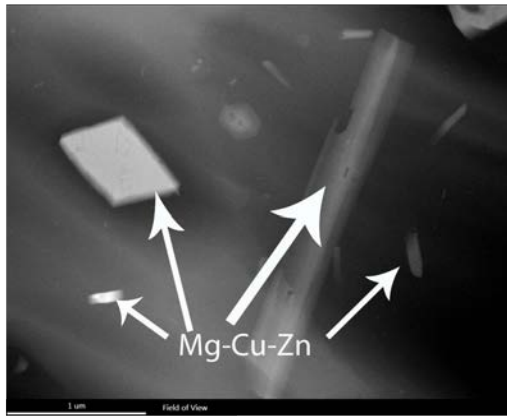
(j) Sample 5



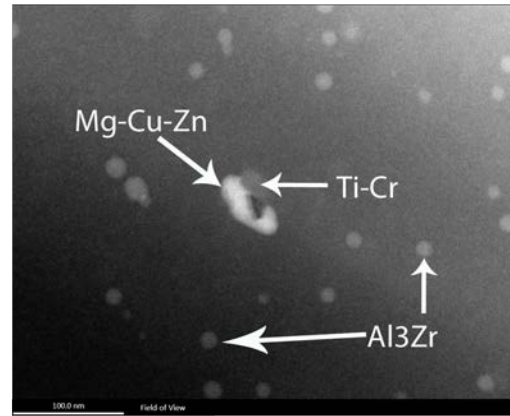
(k) Sample 6



(l) Sample 6



(m) Sample 7



(n) Sample 7

Figure A - 4 TEM/STEM images [TITANAL]

Observations:

Sample 1:

In the as-cast structure we found a homogeneously distributed Mg-Cu-Zn phase in different sizes and shapes (Figure 6.4.1-1 (a)). This is the main phase and the matrix is filled with Mg-Cu-Zn particles. Furthermore we see a very thin and needle shaped Mg-Cu phase and a small number of Mg-Si particles (Figure 6.4.1-1 (b)).

Sample 2:

We still see the same phases as in probe 1. Additionally we found a very Fe-rich particle with a small amount of Nd (contamination) (Figure 6.4.1-1 (e)).

Sample 3:

Most of the Mg-Cu-Zn phase has dissolved into the matrix. Zr-containing dispersoids have precipitated quite homogeneously throughout the matrix. The only coarse particles left are intermetallic and Si-O phases (Figure 6.4.1-1 (f)).

Sample 4:

A Ti-Cr dispersoid was found along a GB surrounded Fe-Ni, Zr and Mg-Cu-Zn particles (Figure 6.4.1-1 (h)). The amount of encountered Fe-Ni particles increases.

Sample 5:

On the GB's we still find some Mg-Cu-Zn phase but the matrix is now homogeneously filled with Zr-containing dispersoids in an ample amount. The only coarse phase left is Fe-Ni (Figure 6.4.1-1 (j)).

Sample 6:

Some coarse Mg-Cu-Zn particles are populating the matrix along with some Mg-Si particles. Additionally to Al-Fe-Mn and Al-Fe-Mn-Si particles we still find the Fe-Ni phase (Figure 6.4.1-1 (l)).

Sample 7:

The matrix is again filled with an ample amount of Mg-Cu-Zn phase in all shapes and sizes (Figure 6.4.1-1 (m)). The dispersoids can be found on a global scale and we also find some Ti-Cr dispersoids on Mg-Cu-Zn particles (Figure 6.4.1-1 (n)).

Zr-containing dispersoids [nm]